Universidade de São Paulo
Instituto de Astronomia, Geofísica e Ciências Atmosféricas
Departamento de Geofísica

Marta Henriques Jácomo

Nuclear magnetic resonance characterization of sandstones with anomalous porosity

São Paulo
2018

Marta Henriques Jácomo

Nuclear magnetic resonance characterization of sandstones with anomalous porosity

Tese apresentada ao Departamento de Geofísica do Instituto de Astronomia, Geofísica e Ciências Atmosféricas da Universidade de São Paulo, para obtenção do título de Doutor em Geofísica.

Área de Concentração: Geofísica Aplicada
Orientador: Prof. Dr. Ricardo Ivan Ferreira da Trindade

Versão Corrigida

(Versão original encontra-se disponível na Unidade que aloja o Programa)

São Paulo

2018

Tese de doutorado de autoria de Marta Henriques Jácomo, sob o título "**Nuclear magnetic resonance characterization of sandstones with anomalous porosity**", apresentada ao Instituto de Astronomia, Geofísica e Ciências Atmosféricas da Universidade de São Paulo, para obtenção do título de Doutora em Geofísica pelo Programa de Pós-graduação em Geofísica, na área de concentração Geofísica Aplicada, aprovada em 25 de outubro de 2018 pela comissão julgadora constituída pelos doutores:

MEMBROS DA COMISSÃO JULGADORA:

Prof. Dr. Ricardo Ivan Ferreira da Trindade - orientador

Instituição: IAG/USP

Presidente

Prof. Dr. Giovanni Chaves Stael

Instituição: ON/Rio de Janeiro-RJ

Prof. Dr. Antonio Abel González Carrasquilla

Instituição: LENEP-UENF/Macaé-RJ

Prof. Dr. Carlos Jorge de Abreu

Instituição: UnB-Brasília-DF

Dr. André Alves de Souza

Instituição: Schlumberger/Rio de Janeiro-RJ

With love,

to my husband and my parents

Acknowlegements

First, I would like to express my gratitude to my advisor, professor Ricardo Ivan Ferreira da Trindade, for his support over the last four years. Thank you for the excellent discussions and great teaching. Thank you most for your patience and for having trusted me when things seemed lost. I am grateful for the excellent partnership and beautiful friendship.

This research was only possible with all the support I had from Professor Tito José Bonagamba, who generously received me in his NMR team (LEAR/IFSC/USP) in São Carlos and helped me a lot in my research. I would like to mention my LEAR friends: Mari, Everton, Elton, Arthur, Alessandro, Renan, Rodrigo and Yuri, besides Edson Vidoto and Aparecido Amorim.

Profs. Luiz Fernando de Ros, Carlson de Matos Maia Leite and Marsha French were very important to this work. I thank them for their considerations, criticisms and productive discussions and by providing key samples and materials.

USPMag Team! Wil, Gra, Karine, Gigio, Aruã, Filipe, Raphael, Thiago, John, Kami, Gelvam, Elder and Oscar, thank you! Special thanks for Sônia, who gently helped me with the preparation of the samples; Plínio, who taught me patiently to do all the measurements in the laboratory and helped me in clarifying many doubts, and Janine and Dani for our lovely friendship, academic ideas and support.

I am in debt to IAG and all professors for the opportunity of doing my PhD in this institution, particularly Prof. Carlos Mendonça who followed my work and the IAG staff for all their support. The work was funded by a CNPq doctorate scholarship.

My beautiful friend Nagirley Kessin, thank you for made her home my home in São Carlos, for listening and advising me when it was necessary.

My deepest gratitude to my parents, brother and sisters, nephews, stepmother and stepdaughter for always being so loving and understandable. I have not yet met a more beautiful and close-knit family than ours! I will make a special acknowledgement here to my family from São Paulo: Eliane, Paulo, Isa and Pri. Thank you for welcoming me in São Paulo and making me feel at home all this time when I was not in São Carlos! My adventure would not be possible without your support. Love!

Last but not the least, I would like to thank my husband for being an incredible partner in this adventure and for transforming my dream into our dream. Thank you for all these 13 years together!

“É junto dos bão que a gente fica mió”

(João Guimarães Rosa- Grande Sertão Veredas)

Abstract

JÁCOMO, Marta Henriques. **Nuclear magnetic resonance characterization of sandstones with anomalous porosity**. 2018. 214 p. Doctorate Tesis – Instituto de Astronomia, Geofísica e Ciências Atmosféricas, Universidade de São Paulo, São Paulo, 2018.

In some geological circumstances, some sandstones are able to preserve high porosity after burial - this porosity is said to be "anomalous". The main mechanisms for the preservation of the primary porosity involves the presence of cuticles of clay or microquartz. Several studies have characterized the macroporosity in this context, but little is known about the micropore structure in these rocks, their surface properties and their relationship with the porosity preservation processes, in part due to the experimental challenge of performing sub-micrometric observations using the classical petrophysical and petrographic techniques. Nuclear Magnetic Resonance (NMR) is able to characterize the pore size distribution, being a fundamental technique to enable the investigation of the preservation of macroporosity and the associated micropore structure. The porosities of sandstones from Fontainebleau (Paris Basin), Água Grande (Recôncavo Basin) and Uerê (Solimões Basin) Formations were partially preserved in the presence of cuticle of microquartz, clay or both. The low magnetic field NMR distributions of these units are characterized by important displacements towards shorter T_2 times, which are related to differences in S/V ratio (Fontainebleau), diffusive coupling (Água Grande), relaxitivity and diffusion processes due to the presence of magnetic minerals (Uerê and Juruá). Relaxitivity from Fontainebleau varies from 1 to 8 μm/s. Água Grande relaxitivity is 32-43 μm/s for macropores, 100 μm/s for micropores in weak diffusive coupling and ~15 μm/s for micropores in intermediate diffusive coupling. In Uerê sandstones relaxitivity varies from 14 to 55 μm/s. If we assume the fast diffusion for high magnetic susceptibility samples from Uerê and Juruá sandstones, the relaxivity varies from 36 to 118 μm/s. Our results show that paramagnetic and ferromagnetic minerals, particularly when they occupy the pore surface, cause a strong displacement of T_2 values towards shorter times, resulting in an underestimation of pore size and porosity values. To reduce the ambiguity in interpretation, it is important to perform experiments increasing the inter-echoes times during the log NMR data acquisition and better characterize the magnetic mineralogy of the rocks.

Keywords: Anomalous porosity, NMR, grain coatings, diffusion coupling, T_2 distributions.

Resumo

Alguns arenitos podem preservar alta porosidade após o soterramento em certas condições geológicas – esta porosidade é dita “anômala”. Os principais mecanismos para a preservação da porosidade primária envolvem a presença de cutículas de argila e microquartzo. Vários estudos caracterizam a macroporosidade de rochas neste contexto, mas pouco se sabe sobre a estrutura dos microporos destas rochas, suas propriedades de superfície e sua relação com os mecanismos de preservação de porosidade, em parte devido às dificuldades em efetuar observações sub-micrométricas usando as técnicas clássicas de petrofísica e petrografia. A Ressonância Magnética Nuclear (RMN) permite a caracterização da distribuição de poros, sendo fundamental na investigação da macroporosidade e da microporosidade em sedimentos com porosidade anômala. As porosidades dos arenitos das Formações Fontainebleau (Paris Basin), Água Grande (Recôncavo Basin) e Uerê (Solimões Basin) foram parcialmente preservadas na presença de cutículas de microquartz, argila ou ambos. A distribuição de tempo de relaxação transversal (T_2 RMN) destas unidades é caracterizada por importantes deslocamentos para T_2 mais curtos, que estão relacionadas a diferenças em razão S/V (Fontainebleau), acoplamento difusivo (Água Grande), relaxatividade e processos de difusão devido à presença de minerais magnéticos (Uerê e Juruá). As relaxatividades calculadas para Fontainebleau variam de 1 a 8 μm/s. Em Água Grande ela é 32-43 μm/s para os macroporos, 100 μm/s para os microporos em acoplamento difusivo fraco e ~15 μm/s para os microporos em acoplamento difusivo intermediário. Em Uerê a relaxatividade varia de 14 a 55 μm/s. Assumindo difusão rápida para as amostras com altos valores de susceptibilidade magnética de Uerê e Juruá, a relaxatividade varia de 36 to 118 μm/s. Os resultados mostram que os minerais paramagéticos e ferromagnéticso, particularmente quando ocupam as paredes dos poros, causam um forte deslocamento nos valores de T_2 para tempos mais curtos resultando em tamanhos de poro e porosidade subestimados. Para reduzir a ambiguidade na interpretação dos dados de MRN, é importante efetuar experimentos de aumento do tempo inter-eco durante as rotinas de RMN de poço e também caracterizar de forma mais completa a mineralogia magnética das amostras.

List of figures

List of Tables

List of abbreviations and symbols

ø	Porosity
k	Permeability
ρ	Density
χ or Sus	Magnetic susceptibility
Sw	Water saturation
$\vec{\mu}$	Nucleus magnetic dipole moment
γ	Gyromagnetic ratio
$\vec{L}$	Angular momentum
$\hbar$	Planck´s constant
$\vec{I}$	Dimensionless spin operator
$\vec{M}$	Net magnetization
$\overrightarrow{M_\iota}$	Induced magnetization
$\overrightarrow{M_{x,y}}$	Transverse magnetization
$\overrightarrow{M_z}$	Longitudinal magnetization
$\vec{\tau}$	Torque
$\overrightarrow{B_0}$	Static magnetic field
$\overrightarrow{B_1}$	Oscillating magnetic field
$\overrightarrow{B_r}$	Reverse magnetic field
$\overrightarrow{B_{SAT}}$	Saturated magnetic field
ω_L	Larmour frequency
T_1	Longitudinal relaxation time
T_2	Transverse relaxation time
T_{2B}	Bulk transverse relaxation time
T_{2S}	Surface transverse relaxation time
T_{2D}	Diffusion transverse relaxation time
ρ_2	Transverse surface relaxivity
α	
D_0	Bulk diffusion coefficient
G	Magnetic field gradient
T_E	Echo-time or time between echoes

r	Distance that proton can travel
R	Radius of pore
S/V	Surface per volume ratio
T	Temperature
P	Pressure
SEM	Scanning Eletron Microscope
MICP	Mercury Injection Capillary Pressure
XRD	X-ray diffraction
μCT or Micro-CT	Micro Computed Tomography
NMR	Nuclear Magnetic Resonance
FID	Free Induction Decay
ILT	Inverse LaPlace Transform
IRM	Isothermal Remanent Magnetization
FORC	First-Order Reserval Curve
Ib	Chlorite polytipe which the angle between the structural axis is 90º
IIb	Chlorite polytipe which the angle between the structural axis is 97º
MD	Multiple Domain
SD	Single Domain
IGV	Intergranular Volume

Table of Contents

1 Introduction

Porosity and permeability are the most fundamental petrophysical properties and correspond to the two basic inputs for successful commercial oil/gas/water resource exploration analysis. In sandstones, both porosity and permeability are closely associated with the mechanical compaction and the amount of pore-filling cement; quartz cementation being the most meaningful mechanism of porosity loss in deeply buried sandstones (Worden and Morad 2003). There are several studies showing that porosity declines with depth (Bjørkum and Nadeau, 1998; Ehrenberg et al., 2008; Worden and Burley, 2003; Taylor et al., 2010). However, some mechanisms are able to preserve the porosity even at great depths producing "anomalous porosity" (Bloch et al., 2002). Two of these mechanisms are the presence of microquartz and chlorite/illite coatings, whose identification is not always simple and depend on empirical data sets.

Nuclear magnetic resonance (NMR) has been an important tool in providing information on rock reservoir characteristics, such as pore-sizes distributions, porosity, permeability and fluid saturation. In well logging, NMR is the only technique which provides pore size distributions (Vincent et al., 2011) and hence information about the microporosity which usually are obtained only through time-consuming laboratory analysis, such as Mercury Injection Capillary Pressure. The NMR technique is particularly suited for the study of microporosity, its surface properties and the relation between micro- and macroporosity.

In this thesis, we will apply NMR techniques, combined with classical petrophysics, microscopic observations and rock magnetic measurements, to study the pore strutucre of sandstones with "anomalous porosity". The main goals of this work are:

1. Investigate the mechanisms of porosity-preservation in sandstones with different coatings and their eventual NMR signature;
2. Investigate the microporosity structure, its connection to the macroporosity and diffusive processes in porosity-preserved sandstones;
3. Investigate the influence of magnetic components (detrital grains, cement and coating) on the NMR relaxation signal which may obliterate the magnetic resonance signal and consequently the analysis of pore size distribution and grain coatings in siliciclastic reservoirs;

The thesis is organized in 6 chapters, which include this Introduction (Chapter 1), Literature Review (Chapters 2 and 3), Methods (Chapter 4), Results (Chapter 5), Synthesis

and Conclusions (Chapter 6). Chapter 5 comprises three articles: **NMR characterization of porosity-preserving microcrystalline quartz coatings in Fontainebleau sandstones** which was accepted for publication in the AAPG Bulletin, **Nuclear magnetic resonance and pore coupling in clay-coated sandstones with anomalous porosity preservation, Água Grande Formation, Recôncavo Basin, Brazil** published in Petrophysics Journal (DOI: 10.30632/PJV59N2-2018a2) and **Magnetic matrix effects on NMR relaxation times in porosity-preserved sandstones: A case study in Solimões Basin** (draft to be submitted to the Journal of Applied Geophysics).

2 Anomalous porosity in sandstones

2.1 General considerations

The pore can be defined as the portion of the rock volume that is not solid and which can be filled by liquids, (dissolved) solids, gases and organisms — in the Earth´s crust, the pores are never empty (Milliken and Curtis, 2016).

Over burial history, changes in the pore volume occur permitting to classify them into primary and secondary pores. The primary porosity is formed at the time of deposition and preserved during the lithification of the rocks (although they can be mechanically or chemically modified), the secondary pores are generated by alteration of minerals after the deposition, during diagenesis (Fraser, 1935 *apud* Pettijohn, 1975; Worden and Burley, 2003). The *diagenesis* consists in "a broad spectrum of physical, chemical and biological post-depositional processes by which original sedimentary assemblages and their interstitial pore waters react in an attempt to reach textural and geochemical equilibrium with their environment" (Worden and Burley, 2003).

The primary and secondary pores can be intergranular, which are between detrital particles, or intragranular, which are within grains or particles (Choquette and Pray, 1970). In siliciclastic rocks, the primary intergranular pores are dominant. Generally, mudstones, carbonate grains and weathered rock fragments present primary intragranular pores when bioclastic fragments or vesicle-rich pumices are present in the rock (Worden and Burley, 2003; Milliken and Curtis, 2016). Figure 1 shows examples of primary porosities and some process of secondary porosity generation.

The classification of pore size is complex and is not a consensus among the authors. Pores that were once considered small (micropores) now assume great importance mainly due to advances of unconventional reservoirs or gas exploration (Milliken and Curtis, 2016).

Loucks et al (2012), for example, adapted the classification of Rouquerol et al (1994), and used the term micropores for those smaller than 2 nm in diameter, mesopores for those between 2 and 50 nm and macropores for those greater than 50 nm.

The maximum size-limit for micropores varies from less than 1 μm, according to the classification of Pittman (1971) to 62.5 μm for carbonate rocks, according to Choquette and Pray (1970). For Glover (2005), they are defined as being less than 2 μm and generally

associated with clays, while in Schön (2014), after compilation of Mann et al (1977), they are defined as the pores with diameter below 0.8 nm.

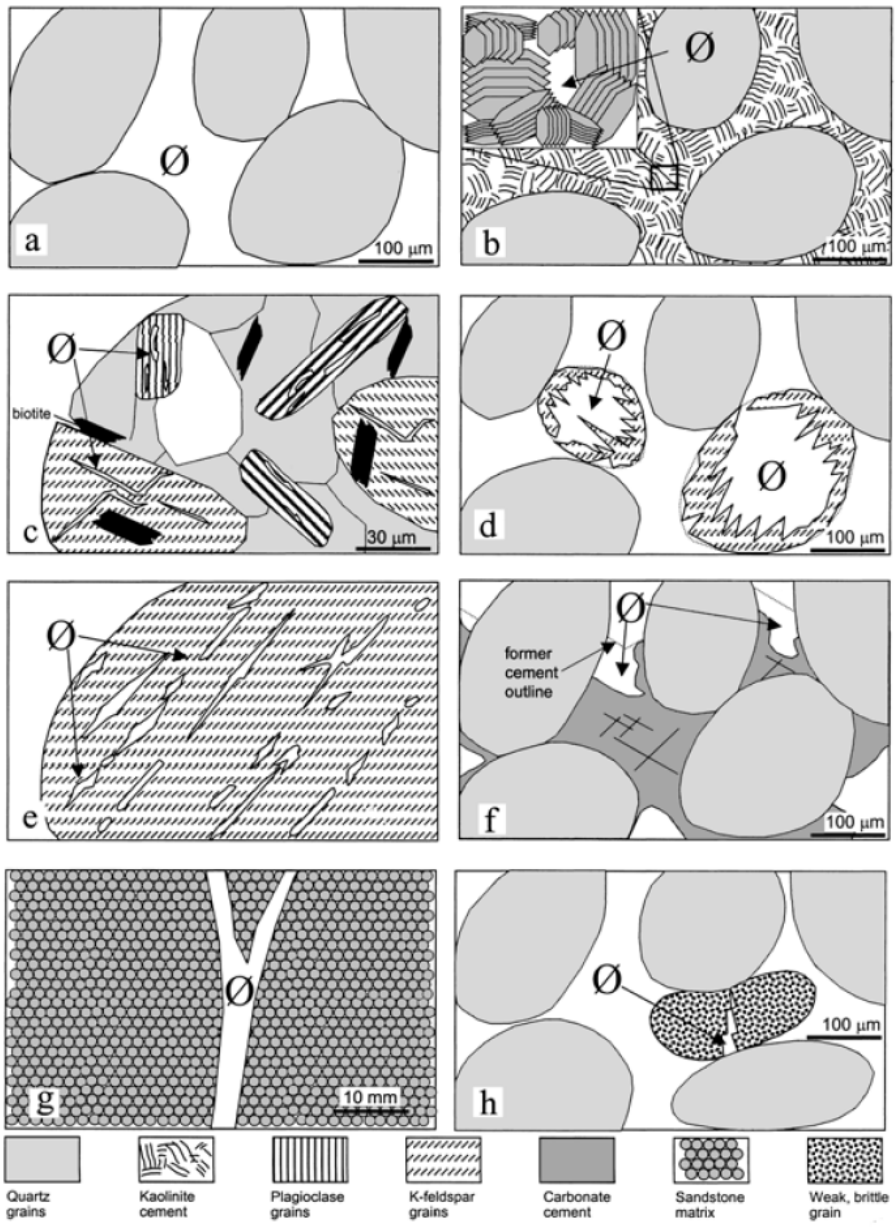

Figure 1 – (a) primary intergranular macropores, (b) primary intergranular micropores between authigenic clay crystals, (c) primary intragranular macropores in rock fragments generated by weathering, (d) secondary intragranular macropores generated by weathered feldspar grains, (e) secondary intragranular micropores (e.g. weathered out plagioclase zones in detrital perthitic feldspar), (f) secondary intergranular macropores generated by dissolved calcite cement, (g) macropore generated by fracture, (h) micropore generated by fracture (Worden and Burley, 2003).

Worden and Burley (2003) defined the microporosity as “the porosity that is only visible with a powerful (e.g. electron) microscope”, while macroporosity is “the porosity that

is visible within the naked eye". This definition is similar to the definition proposed by Cantrell et al (1999) for carbonates, who defines that micropores are about 10 μm since this is the resolution of optical microscopy commonly used for point count methods of porosity estimation.

In this thesis, I adopted a definition similar to that of Cantrell et al (1999). Therefore, here the term micropore was defined as being those that cannot be measured using the optical microscope (only using scanning electron microscopy – SEM), which are <10 μm. Consequently, the term macropore refers to those that are measured through optical microscopy.

2.2 Anomalous porosity

The depositional mineralogy, texture, grain sorting, shape of grains and mechanisms of compaction, cementation, dissolution and recrystallization are usually modified during/after burial, resulting in the loss of porosity with depth (e.g. Schmoker and Schenk, 1994; Ehrenberg and Nadeau, 2005; Ehrenberg et al., 2008). These effects vary from basin to basin, within the same basin, and also according to the lithology. Bjørkum and Nadeau (1998), studying Norwegian continental shelf sandstones and shales, showed a positive, normal porosity loss-depth trend for both lithologies due to mechanical compaction. However, the shales had their porosity much more reduced at depths greater than 1.5 km than the sandstones since the porosity of shales is almost completely lost in the earliest stages of diagenesis. Oelkers et al. 1996 (*apud* Bjørkum and Nadeau, 1998) reported a positive and exponential relationship between the cement volume increasing, which is caused by quartz precipitation and increase of temperature. Ehrenberg and Nadeau (2005) studied the siliciclastic rocks from Alberta, Canada, and stated that porosity loss with depth is a result of the combination of chemical compaction and cementation, both related to thermal burial effects. Taylor et al. (2010), by their turn, showed that rocks from the Gulf of Mexico present a straightforward relationship between porosity loss and depth until ~ 4500 m. From this depth the porosity is extremely variable.

Contrary to the general pattern observed in most basins, some sandstones show significant porosity and permeability even at great depths. This condition was defined by Bloch et al. (2002) as "anomalous porosity". According to these authors, the main factors that govern primary anomalous porosity are: (i) early entry of hydrocarbons into the porous space;

(ii) shallow development of fluid overpressure, and (iii) presence of clay or microcrystalline quartz coatings/rims on quartz and feldspar detrital host grains.

2.2.1 **Early entry of hydrocarbons into the system**

The first studies on the early entry of hydrocarbons as a cement-inhibiting factor date back to 1920 (Johnson, 1920 *apud* Walderhaug, 1994), but here is no consensus among researchers about this effect yet. While Saigal et al. (1992), Gluyas et al. (1993), Worden et al. (1998, 2018); Marchand et al. (2001), Haszeldine et al. (2003) and Bukar et al. (2013) affirm that oil emplacement can inhibit quartz cementation, Ramm and Bjorlykke (1994), Walderhaug (1994), Molenaar et al. (2008), Maast et al. (2011) affirm the opposite.

To understand the influence of oil input in preserving the porosity it is necessary to first discuss wettability – the property that defines what fluid is attracted preferentially to the grain surface if two or more fluid phases are present in the porous space (Worden et al., 1998; Barclay and Worden, 2000). According to thermodynamics any interaction between a surface and a fluid phase occurs with the lowest possible surface energy. Surface energy depends on the rock mineralogy, which is directly related to the specific surface charge and anisotropy, the presence or lack of ferrous minerals at the interface and the diffusion of organic molecules.

In petroleum reservoirs, pH conditions range from 4 to 7. In such conditions, the negative surface of quartz grains attracts positively the charged dipoles of water molecules (Barclay and Worden, 2000). Thus, in a mixed oil-water reservoir, quartz is typically wetting in water. Water-wetting minerals include quartz, illite, single crystals of kaolinite and unweathered feldspar, while oil-wetting minerals consist of carbonate, kaolinite booklets, Fe-rich smectites, chlorites, iron oxides and weathered feldspar (Barclay and Worden, 2000).

Petroleum is a mixture of natural compounds consisting essentially of hydrocarbons and organic derivatives (resins and asphaltenes). Among the various constituent groups of oil (alkanes, aromatic and polar), the polar compounds are those that influence the most the wettability of the reservoir since they are capable of transforming a wetting system in water to another wetting agent due to the electrostatic force and complex interactions with the mineral surface. Oxygen-rich organic matter (type III kerogen) or low thermal maturity favors the formation of polar compounds, while oxygen-poor and hydrogen-rich (type I kerogen) or yet more mature hydrocarbons are less likely to change rock wettability (Barclay and Worden,

2000). Therefore, the source, the temperature and the geochemistry of petroleum formation are the main factors determining the wettability (Barclay and Worden, 2000).

In oil-wet systems, silica-rich pore water is isolated from the quartz host grain by a layer of oil, therefore reducing the effectiveness of quartz cementation. In water-wet systems, the quartz cementation rate is dependent of the source, silica transportation and precipitation (Worden et al., 1998). For Worden et al (1998), quartz dissolution and precipitation are not strongly affected by the emplacement of oil in water-wet reservoir since they occur into the irreducicle water thin layer, but the transport of silica is affected. When silica transport occurs by advection from external sources, the transport is blocked due to the increase of relative permeability. At the same time, the transport of dissolved silica through diffusion is reduced due to the increase in tortuosity with increasing oil saturation, effectively stopping when oil saturation is at its maximum (Worden et al., 1998; Worden et al., 2018). Gluyas et al. (1993) and Marchand et al. (2002) showed a decrease of porosity from structural crests – where oil emplaces first – toward structural flanks. The authors modeled the quartz growth rate after the oil entered gradually the Miller oil field reservoir (North Sea) and confirmed that cement growth is higher in the water zone than in the oil zone, with decreasing mean porosity values in the later. The cementation in this oilfield is inhibited in regions presenting low water saturation (Sw = 20%) and submitted to T > 70 ºC during an effective period of time. Worden et al (2018) studied the effect of oil emplacement in the Ula field sandstones (Norwegian North Sea) and concluded that when it occurs before or during quartz cementation, it inhibits the growth of quartz cement. Conversely, Barclay and Worden (2000) and Molenaar et al (2008) show that no significant difference of porosity and volumes of quartz cementation on oil and water filled sandstones from Magnus field (North Sea) and the Baltic Basin, respectively. Maast et al (2011) showed that hydrocarbon on saturated sandstones occur independently of the porosity and saturation fluid in the south Viking Graben sandstones (North Sea).

There are two main reasons that may explain why oil emplacement may not affect the quartz cementation. The first one is the widespread presence of oil inclusions in cements. The second is the fact that quartz precipitation, which is not affected by oil emplacement on water-rich reservoirs, is the main controlling factor of cementation at temperatures below 130 ºC. Other factors that may be relevant to the interpretation of the factors controlling porosity preservation are: sedimentary facies, porosity types, presence of clay coats on grain surface and quartz cement abundance (Worden et al., 1998; Taylor et al., 2010).

2.2.2 **Fluid overpressure**

The column of overburden sediments exerts pressure on the pores of buried strata as follows:

$$P_{overburden} = \sum_i (\rho_{rock}\ g\ h) \quad (1)$$

where $P_{overburden}$ is the pressure resulting from the rock weight at depth h; ρ_{rock} is the density of the overlying rock and g is the gravity acceleration (Glover, 2005).

The fluid inside the pores also exerts a centrifugal pressure in all directions, called fluid pressure, which is defined by:

$$P_{fluid} = \rho_{fluid}\ g\ h \quad (2)$$

where P_{fluid} is the fluid pressure in the pore at depth h; ρ_{fluid} is fluid density, and g is the gravity acceleration (Glover, 2005).

The connected fluid pressure is called hydrostatic pressure, and it is less than the overburden pressure. The fluid pressure should be about 1/3 less than the overburden pressure since the fluid density is about 1/3 smaller than that of overburden rocks. However, since the connection among the pores within the reservoir is not always good, the fluid pressure can be higher than the hydrostatic pressure provided in equation 2, defining an overpressure condition (Glover, 2005).

Osborne and Swarbrick (1997) and Swarbrick et al (2002) defined three main causes of overpressure: disequilibrium compaction; fluid expansion and lateral transfer. Under normal compaction conditions, the beginning of deposition is characterized by low compaction and consolidation of rocks, generating rocks with high porosity and permeability. With burial, the overburden pressure causes the increase of compaction and the fluids are expelled from the porous medium. Then, contact between grains occurs and the equilibrium of pressure is reestablished. However, when rapid compaction occurs, the time required for the fluid pressure to dissipate is insufficient and the pore fluid is retained within the porous space. With increasing compaction, the fluid is pressurized and the contact between the grains is prevented. Consequently, the grains will support fluids with pressures above the hydrostatic. The disequilibrium compaction (or subcompaction) is the main mechanism forming overpressure zones, which occur mainly in low-permeability sediments such as siltstones, argillites and shales, because they prevent the fluid from being released (Swarbrick and

Osborne, 1998). Fluid expansion occurs during mineral transformations, such as clay dehydration, smectite-illite transformation and oil-to-gas cracking and aquatermal expansion (Osborne and Swarbrick, 1997). Lateral transfer, in turn, occurs when the high pore pressures produced by disequilibrium compaction are transmitted by water through permeable layers to other places in the reservoir (Yardley and Swarbrick, 2000). Tectonic events, capable of displacing normal pressure sealed regions towards shallower and more compressed regions (structural fault planes, for example), can generate overpressure zones since the original fluid pressure is maintained in the region where the hydrostatic pressure is lower (Swarbrick and Osborne, 1998).

2.2.3 **Clay coatings**

Regarding the capacity of preservation of the rock primary porosity, the main clay-forming coatings are smectite, illite/smectite, chlorite/smectite and chlorite (Pitmann et al., 1992). These coatings can have an authigenic or allogenic (detrital) origin. Authigenic clays are the product of chemical and biochemical reactions that take place at the site where they are found, while the allogenic clays are generated outside the deposition site (Wilson and Pittman, 1977), generally as precursor phases prior to burial. Although the vast majority of authors indicate an authigenic origin for clays that enable porosity-preservation (DeRos et al., 1994; Anjos et al., 2000), some authors claim that allogenic clays may also preserve porosity (e.g. Heald and Larese, 1974; Moraes and De Ros, 1990; Wilson, 1992; Dowey et al., 2012; Dowey et al., 2017).

The term “coats” was defined by Dowey et al (2017) as “any coat that covers, completely or partially, a sand grain in three dimensions (e.g. like a coat of fur on an animal) found in modern setting or ancient and deeply buried sandstone”. According to these authors, a coat has different mineralogy and/or no crystallographic orientation relationship to the host grain, however it is not true when we observe the Fontainebleau sandstones, which are formed by SiO_2 host grain and coating crystals. Among the coats formed by clays, the authigenic chlorite is the most effective mineral to inhibit quartz cementation in sandstones (Worden and Morad, 2003).

The chlorite is a phyllosilicate from the clay minerals group, which have the structure 2:1:1. The layers are arranged in sheets, where a negatively charged tetrahedral-octahedral-tetrahedral layer is interspersed with a positive octahedral layer formed by cations and hydroxyls. Its general formula is $(Mg, Al, Fe)_{12}$ $[(Si, Al)_8O_{20}]$ $(OH)_{16}$, although the solid

solutions may encompass a wide variation in composition (Worden & Morad, 2003). The quality of the reservoir will depend on the morphology, the form of distribution (pore filling or pore lining), the depositional environment and the composition of the coats (e.g. Billault et al., 2003; Taylor et al., 2010; Ajdukiewicz et al., 2010; Dowey et al., 2012; Cao et al., 2018). Due to the importance of chlorite in this work, this topic will be developed to cover all the main aspects of chlorite formation and its transformations.

2.2.3.1 Formation and depositional environments

The main formation processes of chlorite include the dissolution of detrital grains, transformation of precursor clay minerals and direct precipitation from the formation fluid (Anjos et al., 2003; Dowey et al., 2017).

2.2.3.1.1 Dissolution of detrital grains

Feldspars and ferromagnesian minerals such as biotite, amphiboles, garnet (almandine) and other heavy minerals in contact with formation waters favor the dissolution of the original grain and its substitution by chlorite (De Ros et al., 1994; Anjos et al., 2003). Chlorite can still be formed by volcanic glasses, fragments of basic rocks and mud intraclasts dissolution.

2.2.3.1.2 Transformation of precursor clay minerals

The major clay precursors for chlorite formation are: (i) berthierine and odinite (green clays), (ii) smectite (infiltrated or authigenic) and (iii) kaolinite (Grigsby, 2001, Anjos et al., 2003, Dowey et al. 2012).

Diagenetic berthierine and odinite are iron-rich clay minerals and occur as coatings or filling the pore spaces typically below the sediment-water interface of delta-estuarine environments (Gribsby, 2001). Ehrenberg (1993) and Gribsby and Langford (1996) have shown that Fe-rich particles are transported by high discharge rivers in rainy periods or by coastal currents that concentrate the sediments. These conditions favor the formation of iron-rich clay as chlorite-serpentine (berthierine and odinite) and Fe-rich matrix. The mixed-layer becomes more chloritic with increasing temperature and depth (Dowey et al., 2012) and the chlorite fills the pore space. In turn, during the dry period or when there is a wide distribution of these ferrous particles, there is a deficit of these particles and the Fe-rich marine clays are

less developed, generating discontinuous or very thin clay coatings. Meteoric water and changes in the oxidative and anoxic conditions of the sediment fluids may also favor the association of chlorite and siderite cement in shallow environments with low compaction.

The smectite diagenesis, in turn, requires processes of mineralogical dissolution and re-precipitation. They must involve an aluminum-rich source or aluminum preservation associated to important loss of silica and increase of Fe, Mg and H_2O to preserve its original structure (McKinley et al., 2003) as exemplified in the following reactions:

$$Ca_{0.1}Na_{0.2}Fe_{1.1}MgAlSi_{3.6}O_{10}(OH)_2 + 1.5Fe^{2+} + 1.2Mg^{2+} + 1.4Al^{3+} + 8.6H_2O \rightarrow \quad (3)$$

(smectite-saponite)

$$Fe_{2.6}Mg_{2.2}Al_{2.4}Si_{2.8}O_{10}(OH)_8 + 0.1Ca^{2+} + 0.2Na^{+} + 0.8SiO_2 + 9.2H^{+}$$

(chlorite) (quartz)

(Chang et al., 1986 *apud* McKinley et al., 2003)

or

$$2.4Ca_{0.1}Na_{0.2}Fe_{1.1}MgAlSi_{3.6}O_{10}(OH)_2 + 0.88H_2O + 1.44H^{+} \rightarrow \quad (4)$$

(smectite-saponite)

$$Fe_{2.6}Mg_{2.2}Al_{2.4}Si_{2.8}O_{10}(OH)_8 + 0.24Ca^{2+} + 0.48Na^{+} + 0.04Fe^{2+} + 0.20Mg^{2+} + 5.84SiO_2$$

(chlorite) (quartz)

(Chang et al., 1986 *apud* McKinley et al., 2003)

The increase in temperature with burial is an important factor for the transformation of trioctahedral (expansive) smectite into the more stable (non-expansive) chlorite. Conversely, dioctahedral smectite tends to develop illite- smectite mixed layers (Chang et al, 1986).

The interaction between saline formation waters and iron-oxide coatings favor the formation of smectite coats, which progressively transform into corrensite and Mg-rich chlorite (Anjos et al., 2003; Ajdukiewicz et al., 2010; Dowey et al., 2012). When smectite is mechanically infiltrated, it can be also transformed in dry conditions into more stable chlorite or illite (with or without intermediate mixed layer) (Moraes and DeRos (1990).

The chloritization of smectite coatings occurs in Mg- rich continental deltaic and fluvial environments associated with eolian arid deposits. In these environments, the clays can be mechanically infiltrated (e.g. Moraes and DeRos, 1990; Luo et al., 2009) or inherited (Wilson, 1992). Authigenic clays also occur in turbidite environments (eg Hillier, 1994; Anjos et al., 2003), estuarine (e.g. Al Ramadan et al, 2005 apud Morad et al., 2010) and evaporites (neoformation), by the alteration of volcanic fragments and by the alteration of kaolinite.

Finally, kaolinite transformation to chlorite occurs through the following reaction:

$$3Al_2Si_2O_5(OH)_4 + 3{,}5Fe_2 + 3{,}5Mg_2+ + 9H_2O \longrightarrow Fe_{3,5}Mg_{3,5}Al_{6,0}Si_{6,0}O_{20}(OH)_{16} + 14H^+$$

kaolinite ⟶ chlorite

(5)

(Boles and Franks, 1979 *apud* Worden and Morad, 2003)

According to Boles and Franks (1979) *apud* Dowey et al (2012), the kaolinite is formed by illitization of smectite, which supplies the necessary iron and magnesium for the transformation. It typically occurs in Fe and Mg rich environments with the increase of temperature (165º - 200ºC) and depth (3.5 Km - 4 Km) (Boles and Franks, 1979 *apud* Worden and Morad, 2003). Jiang et al. (2017), for example, show chloritization of kaolinite in the Huosholing Formation (China) reservoir whose formation water is rich in Mg^{2+} and Al^{3+}. Iijima and Matsumoto (1982), Curtis et al. (1985) and Surdam et al. (1989) suggested that destruction of eodiagenetic Fe-rich carbonates (siderite) and organic-metallic compounds, as well as the reduction of oxidized Fe minerals (hematite) are the sources of chloritization processes.

2.2.3.1.3 Precipitation from the formation fluid

Chlorite precipitation from the formation fluid (neoformation) occurs at great depths through mesodiagenesis of volcanoclastic sandstones, sandstones associated evaporites and carbonates. Chlorite in volcanoclastic lithic sandstones occurs filling the pores or as fringes covering substrates and grains. In mesodiagenetic siliciclastic sandstones, neoformed chlorite may be the result of late dissolution of ferromagnesian detrital grains, eodiagenetic hematite (red sandstones), clay transformation occurring in association with argillites or destabilization of organo-metallic complexes (Anjos et al., 2003). In evaporite/carbonate sequences, chlorite can be formed directly from the Mg-rich brine waters (Anjos et al., 2003).

However, Mg-rich chlorites are likely to be products of undetected precursor smectite transformations, forming mixed layers of chlorite-smectite (Hillier, 1994). Berger et al (2009) describe the presence of three localizations of chlorites in gas reservoirs in Pakistan: filling pores, coatings and chloritization of detrital components. In this case, chlorite coatings are characteristically formed after an initial compaction phase. They are not present in the contact

between grains, but appear before the growth of other diagenetic phases such as quartz overgrowth, therefore filling the pores with chlorite grains and carbonate cementation. The alteration and dissolution of ferromagnesian detrital grains (e.g. biotite) would be the main source of Fe, Mg, Si and Al for the authigenesis of chlorite.

2.2.3.2 Composition, morphology and distribution pattern

Authigenic chlorite may be Fe-rich (charmosite), Mg-rich (clinochlore) or present instead a wide variation in the concentration of these elements.

Fe-rich chlorites generally present polybodies Ib = 90º transforming in IIb = 97º and interlayer thicknesses of 7 Å below 200 ºC. They are generally associated with siderite, quartz, calcite, kaolinite and feldspar dissolution. The Mg-rich chlorites have a plaque shape, occasionally in hexagonal particles unique to the polytype IIb = 97°. These occur in association with FeO rims, anhydrite, K feldspar, calcite, quartz, dolomite and fibrous illite. Generally, they exhibit honeycomb morphology when the precursor is smectite (Hillier, 1994; Wilson et al., 2014).

Wilson and Pitmann (1997) showed that clay morphology is correlated with the concentration of Fe, where plaques and rosettes > honeycomb > cabbagehead, although the morphologies can be very confusing. For example, in the Central Graben, North Sea, UK, the chlorite coats present similar morphology and composition to the smectites (Humphreys et al., 1989).

The plaques develop more commonly as individual idiomorphic crystals attached to the detrital grains. Often, measuring the size becomes difficult depending on grain orientation and framework grain packing. The rosettes are formed by authigenic clays, which can form pore linings or fill the pores (Wilson and Pitmann, 1997; Wilson and Stanton, 1994). The crystals usually have lobed edges and often fill pore throats. This produces a drastic reduction of permeability, although the porosity is still preserved. Honeycomb morphologies also consist of plaques, but have a cellular pattern around the detrital grains. Generally, they are associated with the intermediate composition of Fe. Cabbagehead morphology is rare and occurs as small and equidimensional coats on host grains or fills the pores.

Clay flakes size and morphology define the quality of the reservoirs, being able to produce both positive and negative effects on porosity and permeability. When chlorite grows parallel or with low angle in relation to the detrital grains, the effect is positive for both

porosity and permeability. When flakes grow perpendicular or at high angles to the detrital grains as occurring on chlorite-smectite or smectite, they can preserve porosity but have a negative effect on permeability. Any clay that fills the pores has a negative effect on both porosity and permeability of reservoirs (Billault et al., 2003; Dowey et al., 2012, Smith et al., 2013, Cao et al., 2018).

2.2.3.3 Impact of chlorite on reservoir quality

The grain-coating chlorite provides generally a positive or mixed effect on reservoir quality, generating a great preservation of porosity and/or permeability in deep reservoirs. Negative or null effects are present in only 13% of chlorite-coated reservoirs (Dowey et al., 2012). However, the way in which it contributes to preservation is no consensus in literature (e.g. Pittman and Lumdsen, 1968, Heald and Larese, 1974, Ehrenberg, 1993, Hiller 1994, Billault et al., 2003, Ajdukiewicz and Larese, 2012). Billault et al (2003) showed some of the mechanisms for inhibition of quartz overgrowth by chlorite coatings: (i) quartz overgrowth does not occur because pressure dissolution reduces the Si available in the system (Pittman and Lumsden, 1968; Thomson and Stancliffe, 1990, *apud* Pittman et al., 2002); (ii) chlorite grains can retard the secondary quartz growth even the conditions are favorable for crystallization (Heald and Larese, 1974); (iii) chlorite grains inhibit the growth of quartz due to separate the detrital grains surface to pore water, preventing the dissolution of the grains and avoiding nucleation (Ehrenberg, 1993); (iv) inhibition of quartz overgrowth occurs due to the limited epitaxial growth of inter-particle space by chlorite; and chlorite coatings do not prevent the nucleation of the quartz cement (Billault et al., 2003; Ajdukiewicz and Larese, 2012).

Chlorite particles which are parallel or slightly oblique on the detrital surface tend to orient themselves progressively perpendicular with the increase of the distance of the grain due to geometric selection. During particle growth, the particles compete for available space such that some oriented crystals gain favorably more growth space than others. In this process, only high tilting or perpendicular crystals continue to grow, as nothing can inhibit crystal growth since there is no competition among them. The number of crystals fast decrease with an increase of crystal size as they move away from the surface until their stabilization. Thus, syntax or low angle quartz growth occur forming crystals under the chlorite coatings (Billaut et al., 2003; Ajdukiewicz and Larese 2012).

The efficiency of the inhibitory mechanisms also depends on the amount of coatings or rims and their discontinuity (Taylor et al., 2010; Morad et al., 2000). When the layers are thin, they tend to be discontinuous, favoring quartz cementation. Other factors that determine this efficiency are burial history, sandstone composition and grain size (Bloch et al., 2002).

The control of grain size in primary porosity and permeability is a function of the relationship among grain size, surface area and pore throat size. In a given volume of sandstone, the larger the grain size, the smaller the surface area. Therefore, it takes a smaller volumetric fraction of chlorite to coat a coarse grain than a fine grain. The effect of the larger surface area on fine-grained sandstones is enhanced because the coatings thickness has a significantly higher deleterious impact on permeability when compared to coarse-grained sandstone due to throat pore sizes (Ehrlich et al., 1991). The pores and throat of pores are wider on coarse sandstones than finer grained sandstones when they are well selected and with a limited amount of cement. Chlorite coatings of a given thickness (the thickness of the coating does not depend on grain size) are much more restricted in a narrow than in a broader throat (Bloch et al., 2002). The contribution of the composition of chlorite in the preservation mechanisms is still doubtful (Pittman et al., 1992; Anjos et al., 2003). While Heald and Larese (1974) argue that the efficiency of inhibitory mechanisms varies with coating composition, Lander and Walderhaug (1999) affirm that composition does not affect the preservation mechanisms.

Sandstone reservoirs with high anomalous porosities are those containing eodiagenetic pre-compaction clays that are chloritized. They show continuity necessary to inhibit quartz cementation and pressure dissolution (Morad et al., 2000; Anjos et al., 2003). Those with late and neoformed mesogenetic chlorite coatings do not present such porosity preservation, since the sediments would have been submitted to the conditions necessary for cementation. An exception to this rule would be the formation of chlorite by the direct precipitation of interstitial fluids (Berger et al., 2009).

It is important to note that chlorite acts only in the preservation of primary porosity by inhibiting quartz overgrowth, and does not act in other cementation processes (e.g. carbonates) (Berger et al., 2009).

Quartz cementation is one of the most important process leading to the lithification of siliciclastic sediments and destroying the porosity. However, small amounts of randomly oriented microcrystalline quartz coats are known to preserve the primary porosity (e.g. McBride, 1989).

2.2.4 **Microcrystalline quartz coatings**

The presence of microcrystalline quartz coats require a source of elevated amounts of dissolved silica, which are mainly formed by dissolution of organic opaline such as sponge spicules (e.g. Vagle et al., 1994; Aase et al., 1996, Hendry and Trewin, 1995; Jahren and Ramm, 2000; Lima and De Ros, 2002; Worden et al, 2012; French and Worden, 2013) and fragments of volcanic rocks (e.g. Hattori et al., 1996; Weibel et al., 2010). The amorphous silica isolates the detrital quartz grain from cement, allowing the sequential quartz microcrystals to grow randomly and inhibiting the pore-filling quartz overgrowth (French and Worden 2013).

This topic will support the main aspects of microcrystalline quartz formation and its effects on reservoir quality.

2.2.4.1 Formation and depositional environments

The siliceous cement covering the detrital grains results from fast dissolution and precipitation processes of biogenic opal-A (amorphous silica), opal-CT (cristobalite-tridymite), chalcedony or cryptocrystalline quartz and microcrystalline quartz. This sequence clearly shows the change from high-entropy to low-entropy phase through *Ostwald ripening* process, which control the recrystallization of silica minerals (Williams and Crerar, 1985; Morse and Casey, 1988; Lima and DeRos, 2002). The *Ostwald ripening* process defines that the inibition of quartz cementation is driven by crystal size, whose growth depends on differences in free energy of crystal faces. In this context, crystals smaller than a specific size dissolve while crystals larger than the specific size grow.

Opal-A → opal-CT → quartz sequence occurs due to differences in specific surface area, allowing a dissolution-reprecipitation pathway in early diageneses, which is given by :

$SiO_2 + nH_2O$ (amourphous silica) $+ 2H_2O \leftrightarrow H_4SiO_4 + (n + 2)\ H_2O \rightarrow SiO_2$ (crystalline silica) $+ (n+2)\ H_2O$ (6)

(Chang and Yortos, 1994)

Some silicious microorganisms, such as sponge spicules, precipitate opal-A to form tests, which are accumulated on the sea flor after their death. With increasing burial and diagenesis, these tests can be fragmented, dissolved and precipitate as opal-A within the pore space of rocks. Therefore, the water pore is initially supersaturated in silica (point 1 in Figure

2) when it be compared with lower surface area opal-A or other silica phases. The water is yet saturated, so the nucleation and growth of CT-opal and quartz is happening from supersaturated solution. If the dissolution of opal-A is faster than nucleation and growth of CT-opal, which are faster than quartz growth, the dissolved silica opal-A specific area will little decrease forward the point which surface area changes do not affect the opal-A solubility (point 2 in Figure 2). As the dissolved silica concentration continues to decrease due to fast nucleation with respect to growth, the superficial area of opal-A and CT increases. This process occurs until the opal-CT growth exceeds the remaining opal-A. When it occurs, both silica concentration and superficial area decrease. Now, opal-A solid is absent and opal-CT solid is predominant. The pore water is still saturated and quartz crystals can be formed (Williams et al., 1985; Lima & DeRos, 2002; Figure 2). The large number of micro quartz crystals indicate that the dissolution rate of the micro quartz precursors are fast enough to maintain silica saturation at the micro quartz nucleation level, resulting in several crystals rather than just a few large crystals (Jahrem & Ramm, 2000; Lima and Deros, 2002).

Ostwald-Freunlich equation for SiO_2 determines how supersaturation is the water pore allows small crystalls growth (Aase et al., 1996):

$$\log\left(\frac{K_r}{K_\infty}\right) = \frac{\upsilon\sigma}{\text{r}1.152RT} \tag{7}$$

where K_r is the solubility of crystal radius; K_∞ is solubility (or equilibrium constant) of an infinitely large crystal; υ is mole volume of quartz (22.688 cm^3/mol), σ is quartz free energy in water (3.6 X 10^{-5} J/cm^2), R is 8.3143J/K mol; T is temperature (373K or 100ºC).

The amorphous silica has solubility of 60-130 ppm, which are 10-20 times higher than quartz solubility (6-10 ppm) at 25° C (Williams et al., 1985). In the temperature range from 0° C to 100° C, chalcedony is approximately twice as soluble as quartz (Gislasson et al., 1993). Aase et al (1996) obtained values of solubility of 60.6 and 61.2 ppm for crystals with 0.5 μm and 0.25 μm radius, respectively. These values are tipical of supersaturated waters, implying that microquartz crystals will grow only while amorphous silica is present. When this amouphous fase is not presente, the micro quartz stops growing and porosity is preserved.

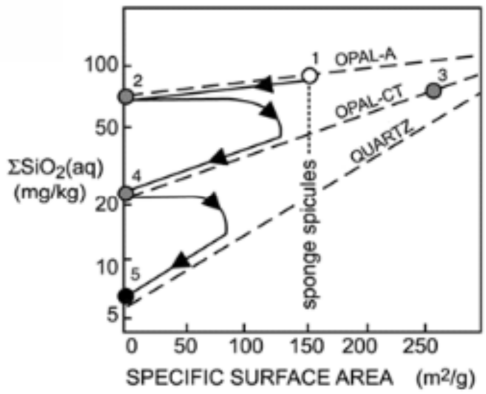

Figure 2 – Diagram showing the relationship between the classic evolution of silica polymorphs within the pore space and the specific surface (Lima and De Ros, 2002). See details in the text.

Quartz cements and macrocrystalline quartz despite being of similar composition, present structural disparities. Quartz overgrowths have syntaxial orientation with the detrital grain, that is, crystals grow faster along the crystallographic *c-axis* and towards the pores. On the other hand, the crystallized chalcedony grows along the *a*-axis, or the [1120] direction, which is perpendicular to *c*-axis. Worden et al. (2012) and French et al (2013) showed the syntactic cross-fertilization of quartz cement with the detrital grain may be followed by the precipitation of a very thin layer of amorphous/chalcedony silica. The micro quartz grains formed subsequently would have inherited the crystallographic orientation of the chalcedony *c*-axis, being parallel to the surface of the detrital grains. The result is that the microcrystalline quartz cement does not grow towards the pores to clog them, but rather parallel to the walls, preserving them (Figure 3).

Microcrystalline quartz is present on shallow marine (Lima and DeRos, 2002; Worden et al., 2012; French et al., 2013), fluvio-marine deltaic (Catagay et al., 1996), lakes (Hattori et al., 1996) and fluvio-eolian environments (Leite et al., 2014).

In fluvio-marine deltaic environment, the microcrystalline quartz could be precipitated when fluvial waters with high silica contents mix with marine pore waters (Catagay et al., 1996). In turn, the presence of microcrystalline quartz on fluvial environment was identified by Hattori et al. (1996). The authors described only two thin chert layers (<10cm) present in the Kunimi Formation (Niu Mountains, central Japan). The chertification derived from devitrification and weathering of volcanic ash and consisted in transformation of A-opal to CT-opal and quartz. Chert would have accumulated rapidly in the shallow lake near the source during eodiagenesis while the lithification process was finalized before the deposition

of the overlying rocks. According to these authors, the rotation and packing of “silica balls” (cherts), destroyed old structures and formed crystals, suggesting not only a solubility process but also a mechanical process of formation. The authors did not analyze the effect of microcrystalline quartz on porosity preservation. An example of microcrystalline quartz in aeolian sandstones is provided by Leite et al. (2014) for the Recôncavo Basin, after identification of microquartz rims, which inhibited quartz overgrowth. According to these authors, the precipitation of microquartz would have happened early in the diagenetic history, during percolation of alkaline solutions in semi-arid climate.

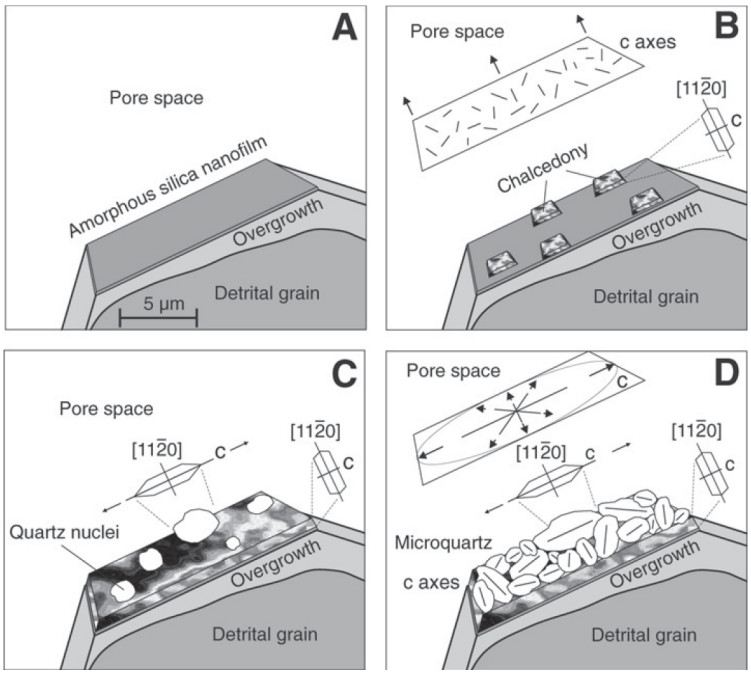

Figure 3 – Sketch showing the sequencial growing of polymorphs of silica. A) The quartz overgrowth which as the same grown orientation of detrital grains can be formed during the early diagenesis; B) Then, chalcedony crystals grow into pore space perpendicularly the host grain or along [1120] directions. C axes are randomly oriented in nanofilm plane; C) Microcrystaline quartz crystals inherit the calchedony´s structure which c axis are parallel to grain surface; D) the microquartz crystals are mesorientated and grow subparallel to nanofilme until the colision among. So, the growth into the pore is inhibited, preserving the primary porosity. The arrows indicate the direction of growth (Worden et al, 2012).

2.2.4.2 Impact of microquartz coatings on reservoir quality

Microcrystalline quartz coats are known to preserve the porosity even at high depths, however their identification in this case is difficult. That is because microcrystalline quartz coats can occur together with other processes, such as hydrocarbon emplacement, and the

microcrystalline crystals almost always can be identified only through SEM images (Bloch et al, 2002; Taylor et al., 2010). An example is provided by the Miller Field, North Sea (Marchand et al., 2002, Aase and Walderhaug, 2005; Maast et al., 2011).

The amounts of microquartz, the continuity around the host quartz grains and the geometry of microquartz define the quality of reservoir (Aase et al.,1996; French and Worden, 2013). According to these authors, if the volume of microquartz coatings is from 2-5 vol. %, and all the grains are coated by microquartz, the reservoir is good. In its turn, more than 10 vol. %, there is an excessive microquartz cementation and the silica can also precipitates as chalcedony and aggregates of microcrystalline quartz in open pore, affecting mainly the permeability of reservoir. These characteristics only occur if the microquartz growth is parallel to the grain surface and along the fast c-axis. Hence, the crystals cannot coalesce crystallographically, limiting their growth length and size (French and Worden, 2013).

3 Nuclear Magnetic Resonance

NMR has been applied as a petrophysical tool in the oil and gas industry, and provides unique information about the geometric and structural features of the porous medium (Kleinberg and Jackson, 2001), including the pore size distribution, porosity, permeability, saturation and capillary adsorption (Coates, 1999, Vincent et al., 2011; Mitchell et al., 2013; Song, 2013).

The following topics address the basic theory of NMR applied to porous media. The concepts described here are based on Brownstein and Tarr (1979), Mitra et al. (1993), Hürlimann et al. (1994), Kleinberg et al. (1994,1996), Kleinberg and Vinegar (1996), Kenyon et al. (1995), Kenyon (1997), Freitas and Bonagamba (1999), Coates et al. (1999), Dunn et al. (2002), Song (2003), Appel (2004), Sen (2004), Anand and Hirasaki (2005), Souza (2012), Mitchell et al. (2013), Salimifard et al. (2014) and Behroozmand et al. (2015).

3.1 Basic principles of NMR

A resonance is defined as the physical interaction between two systems, each having specific frequencies and amplitudes (e.g. an elastic wave vibrates according the sound). For NMR, the resonant systems are the atomic nuclei, which are into an external static magnetic field, and an oscillating magnetic field applied perpendicular to this external field. The frequency of the electromagnetic waves coming from oscillating magnetic fields must be equal to the frequency of the atoms that compose the matter into a static magnetic field.

According to the semi-classical theory, electrons, protons and neutrons have an intrinsic magnetic moment $\vec{\mu}$, which is proportional to their angular momentum ($\vec{L}$):

$$\vec{\mu} = \gamma \vec{L} = \gamma \hbar \vec{I} \tag{8}$$

where γ is the atom gyromagnetic constant, $\hbar$ is the reduced Planck constant ($6.63 \times 10^{-27}/2\pi$ erg.seg) and $\vec{I}$ is the angular momentum of spin that is called spin-spin. The $\vec{I}$ value depends on the number of protons and neutrons of the atoms and the interactions between them (Table 1). When all the atoms with an odd number of protons or neutrons possess a spin angular momentum, the nuclei are unpaired, having $\vec{I} \neq 0$ and hence, will lead to NMR signals. Hydrogen (^{1}H), carbon (^{13}C) and sodium (^{23}Na) are examples of nuclei which have good NMR responses, depending on the abundance of these elements in sample (Figure 4 and Table 1).

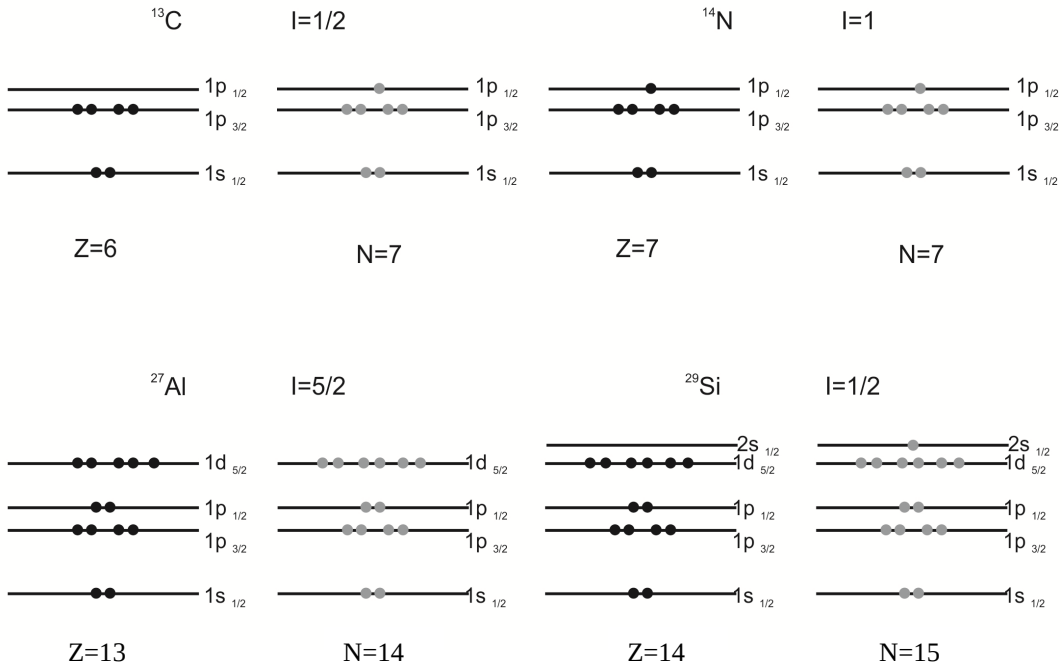

Figure 4 – Proton and neutron distribution according to the values of spin number I for the elements ^{13}C, ^{14}N, ^{27}Al and ^{29}Si. When the spin is unpaired, it produces the NMR response (Azevedo, 2017).

Table 1 – Values of spins I integral, semi-integral and null.

N. protons (Z)	N. neutrons	Mass	I (spin nuclear)		Examples
Even	Even	Even	0		$^{12}C_{6l,}$ $^{16}C_8$
Even	Odd	Odd	Semi-integral	$^1/_2$ $^3/_2$	^1H, $^{13}C_6$ $^{33}S_6$
Odd	Even	Odd	Semi-integral	$^1/_2$ $^3/_2$	$^{19}F_9$ $^{11}B_5$, $^{23}Na_{11}$
Odd	Odd	Even	Integral		$^2H_1$, $^{14}N_7$

In the petroleum industry, the ^1H atom is of interest since it is present in the formation fluid of rocks — water and hydrocarbon. Figure 5 shows the associated intrinsic magnetic moment of H^+ protons, which is compared to a small magnet.

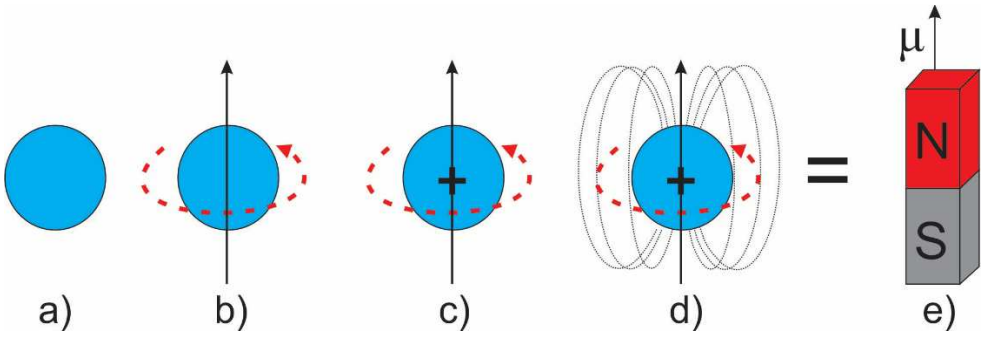

Figure 5 – The hydrogen proton is characterized by a small sphere (a), which has an angular momentum of spin due to the rotational movement about its own axis (b); it generates its own magnetic field around itself (c and d), behaving as a small magnetic dipole (e), with an associated intrinsic magnetic momentum (μ).

Under the action of the weak magnetic field of the Earth (~$5x10^{-5}$ T, on average), the magnetic moment of H^+ protons are randomly distributed, so that the resulting magnetization is equal to zero. When the protons are subjected to the external magnetic field $\vec{B}_0$, a torque is generated to align the spins with the field (Figure 6 and Figure 7). This torque produces a temporal variation in the nuclei angular momentum until the alignment is reached:

$$\vec{\tau} = \Delta\vec{L}/\Delta t = d\vec{L}/dt \tag{9}$$

$\vec{\tau}$ can also be calculated as a function of the intrinsic magnetic moment:

$$\vec{\tau} = \vec{\mu} \times \vec{B} \tag{10}$$

Therefore:

$$d\vec{L}/dt = \vec{\mu} \times \vec{B} \tag{11}$$

From Equation 8:

$$\frac{d}{dt}\left(\frac{\vec{\mu}}{\gamma}\right) = \vec{\mu} \times \vec{B} \rightarrow \frac{d\,\vec{\mu}}{d\,t} = \left[\vec{\mu} \times \gamma \vec{B}\right] \tag{12}$$

Equation 11 defines the precession movement of an isolated magnetic momentum around the field $\vec{B}_0$ (Figure 6). The frequency associated with this movement is known as Larmor Frequency:

$$\omega_L = -\gamma \left| B_0 \right| /2\pi \tag{13}$$

where ω_L is Larmor angular frequency; γ is the gyromagnetic constant, which is intrinsic to each core and whose signal dictates the rotation direction of the precession movement and is defined as the magnetic and angular momentum ratio (the H^+ proton has a high gyromagnetic constant of 0.2675 X 10^9 s^{-1} T^{-1}).

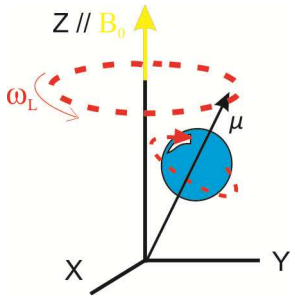

Figure 6 – Vector representation of the precession movement of a core with magnetic momentum μ in response to the applied magnetic field B_0 parallel to z-axis, or longitudinal axis. The XY plane is called the transverse plane (adapted from Coates, 1999).

The frequency at which the protons precess is changed by any modification in B_0. The field intensity used in laboratory studies varies greatly. For petrophysical studies, magnetic fields below 50 mT (or Larmor frequency equal to 2 MHz) are recommended, but high magnetic fields (2 T or 85 MHz) are used for specific experiments.

Based on the semi-classical theory, during precession all the individual magnetic momentums of H^+ protons are aligned with the B_0 field direction, and the nuclei precess at the same Larmor frequency, absorbing or emitting energy. The quantization of the spin angular momentum of the isotope ^1H (I = 1/2) has two directions associated with the energy levels that the proton can occupy – N^- or N^+ populations. Under the magnetic field B_0, the nuclei move from the higher to the lower energy level (N^-) emitting energy to the neighborhood, such that over time, the N^- population gradually increases as N^+ decreases. This behavior is described by the Boltzmann distribution:

$$\frac{N^+}{N^-} = e^{-\gamma B_0 \hbar \ /\mathrm{kT}} \tag{14}$$

where N^+ and N^- are populations with nuclei in the high and low energy states, respectively; $\gamma B_0 \hbar$ is the magnetic energy, and kT is the thermal energy.

The population difference between the energy levels generates a net magnetization M_0 which is aligned with the longitudinal M_z axis (Figure 7 and Figure 8) and proportional to the number of ^1H in the sample. It is the so-called thermal equilibrium magnetization and it will

produce the detectable signal on the coil. The net magnetization vector in thermal equilibrium is given by the Curie law:

$$M_0 = B_0 (n \gamma^2 h^2/4K_BT) \quad (15)$$

where n is the number of protons per volume; γ is the gyromagnetic constant; *h* is the reduced Plank constant; *T* is the temperature, and K_B is the Boltzmann constant.

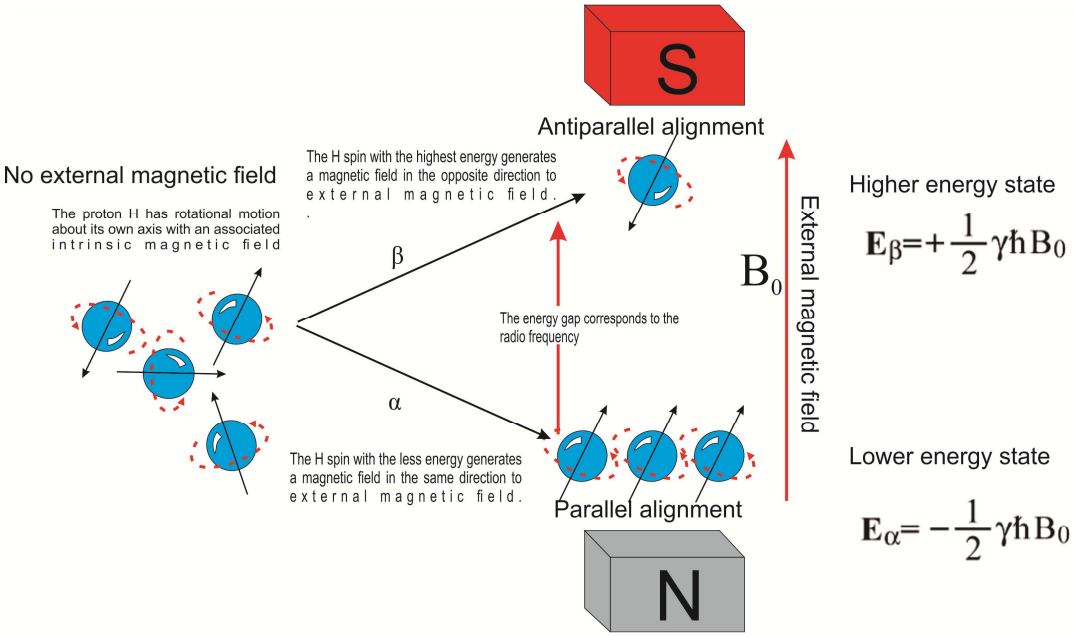

Figure 7 – The spins of hydrogen protons are randomly orientated in the absence of an external magnetic field (generated by logging or laboratory tool), where $N^+ = N^-$. Under the action of the applied external magnetic field, the ^1H protons are distributed in two energy levels while a larger number of low energy protons are aligned parallel with the applied field.

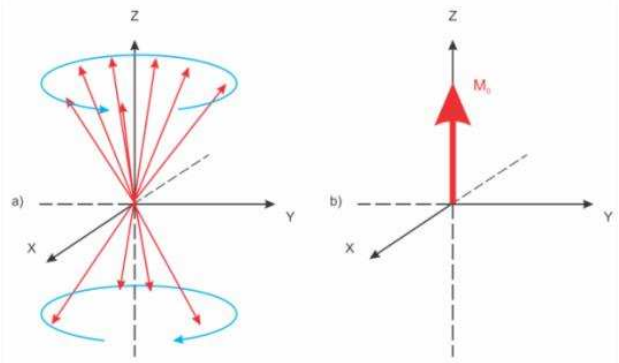

Figure 8 – a) Spins aligned parallel and antiparallel with the applied external magnetic field (z-axis) forming a precession cone; b) resulting in a magnetizing vector (M_0) (adapted from Coates, 1999).

Electrons also have a magnetic moment and angular momentum. If electrons around the nucleus (or a charge in movement) precess around the static magnetic field, they produce a magnetic moment opposite to the applied magnetic field (Lenz low). We define these atoms

as being diamagnetic. In paramagnetic atoms the spins of electrons are unpaired, and the magnetic moment tends to align with the external magnetic field, the net magnetization therefore compensating the diamagnetic effect. Due to their small mass and larger interaction energy, the magnetic moment of electrons is stronger and more dependent on the surroundings than that of the ^{1}H nuclei.

Although the net magnetization is different from zero in the axis parallel to the external magnetic field B_0, a coil perpendicular to the transverse plane would not detect any NMR signal since M_z is a stationary component, that is, it does not vary with time (Figure 8 and Figure 9a). Similarly, no signal would be detected if the coil were positioned in the transverse plane, because although the magnetic components vary with time, they are randomly distributed on xy-plane and it resultant is zero ($M_{x,y}$=0) (Figure 9a).

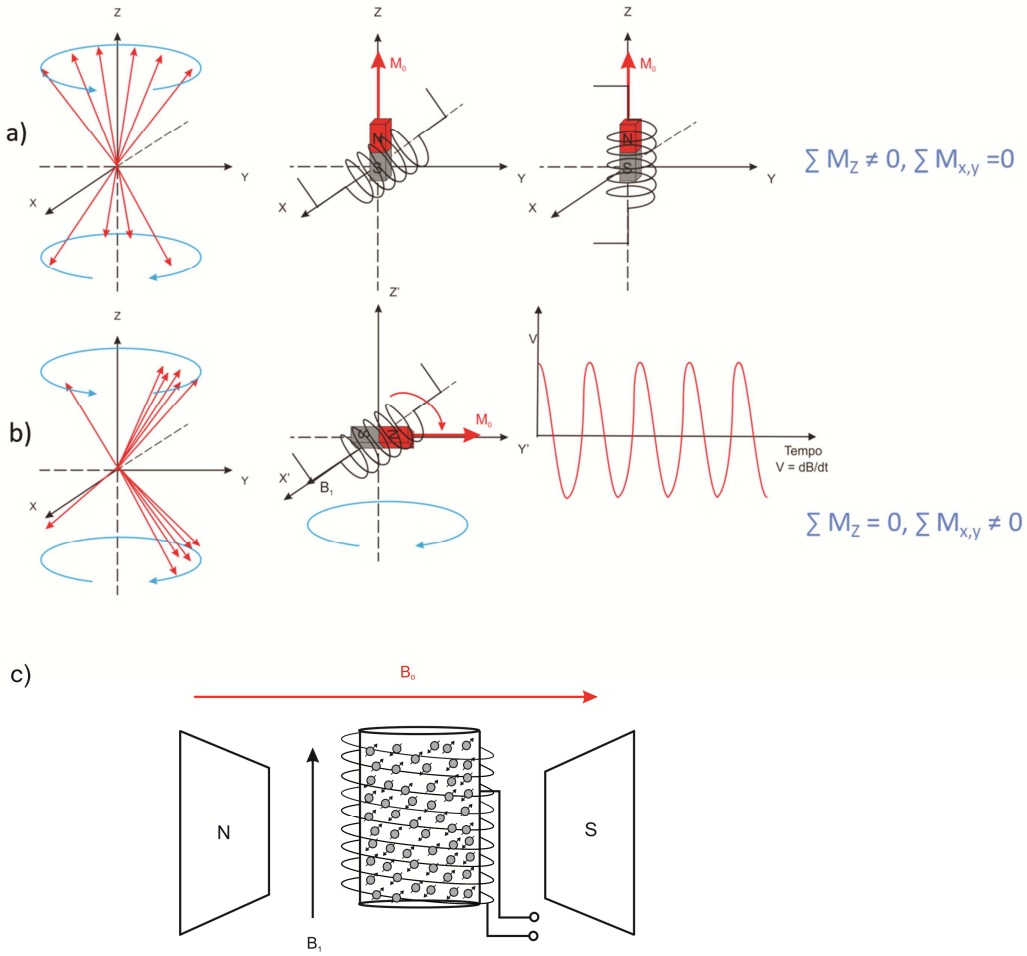

Figure 9 – a) The coil perpendicular to the z-axis cannot detect any signal because the magnetization in the transverse plane is equal to 0; parallel to the z-axis, no signal is also obtained, since it is stationary; b) to have signal, it is necessary to shift the magnetization to the transverse plane, where magnetization can vary with time.; c) B_0 and B_1 applied field into sample.

The magnetization vector needs to be shifted from the longitudinal z-axis to the transverse xy-plane to induce an electric current in the coil positioned in the transverse plane. When an oscillatory magnetic field is applied for a short time perpendicular to B_0 (B_1) with a frequency equal to the Larmor frequency, the protons in the low energy state will absorb energy from the neighborhood molecules and change to a high energy state equating the N^+ and N^- populations. Thus, mathematically, the magnetization in the z-axis cancels out (M_z = 0), and the nuclear spins move away from z-axis and begin to precess around in the xy-plane ($M_{x,y} \neq 0$). This precession motion induces an electromotive force on the coil as a function of the magnetic flux variation (Figure 9b).

Figure 10 shows the effect of applying an RF pulse on the precession movement over time. When the pulse lasts long enough to shift the magnetization M_0 to 90° ($\theta = \pi / 2$ radians), the magnetization is then maximized. When the RF pulse ceases, the nuclear spins return to their equilibrium thermal state, where $M_{x,y} = 0$ and $M_z = M_0$. The oscillatory signal induced in the coil gradually decays due to several factors such as the spin-spin interactions and their environment (e.g., uniformity of the magnetic field and presence of paramagnetic nuclei in the sample). The time domain measured signal is called *free induction decay* (FID) which is proportional to the magnetization and occurs until the magnetic momentums of the nuclei align with B_0 (see more details in section 3.1.2).

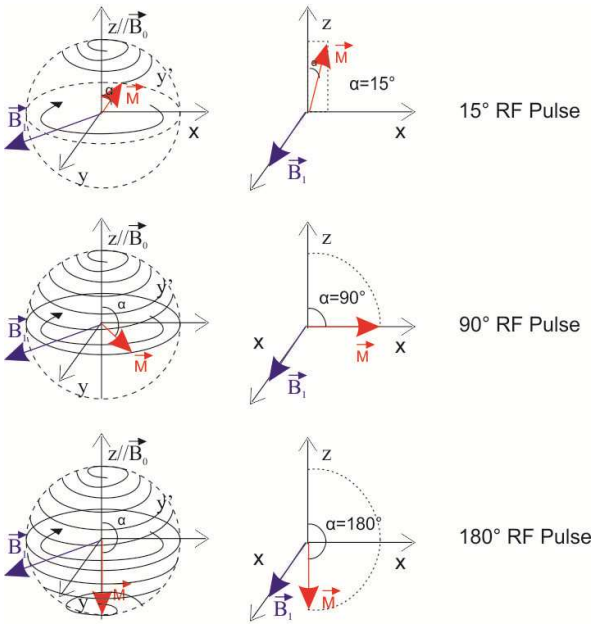

Figure 10 – RF pulse applied at 15º, 90º and 180º in a rotating reference frame (adapted from Bonagamba, 2005). The time used for RF pulse defines the necessary angle to shift the magnetization to transverse plane.

The longitudinal relaxation (T_1) is related to the magnetization return time to the longitudinal axis and is influenced by the energy exchange between the excited spin proton and its molecular neighborhood (network) until reaching thermal equilibrium. The transverse relaxation (T_2) is related to the interaction between spins (spin-spin), that is, the reduction of magnetization in the transverse plane.

3.1.1 Longitudinal relaxation time T_1

The longitudinal relaxation is related to the magnetization return time to the longitudinal axis, or the state of thermal equilibrium, which is described by:

$$\frac{Mz(t)}{M_0(\infty)} = (1\text{-}ce^{-t/T_1}) \quad (16)$$

where M_z is the magnetization on the z-axis; M_0 is the initial maximum magnetization in a given magnetic field; *t* is the time when the protons were exposed to the field B_0; c is a scalar constant determined from the set of spins, and T_1 is the longitudinal relaxation time.

T_1 is the time required for magnetization to reach 63% of its equilibrium value and reflects how effectively the spins magnetic energy is transferred to its neighborhood. The spin-environment (or spin-lattice) interactions occur through the fluctuating magnetic field in the sample, which is caused by nuclei-nuclei interactions due to thermal agitation and/or proximity to pore surface. So, when the nuclei "feel" distinct magnetic fields, they dissipate energy until the thermal equilibrium state is reached and there is no more magnetization in the transverse plane (Figure 11).

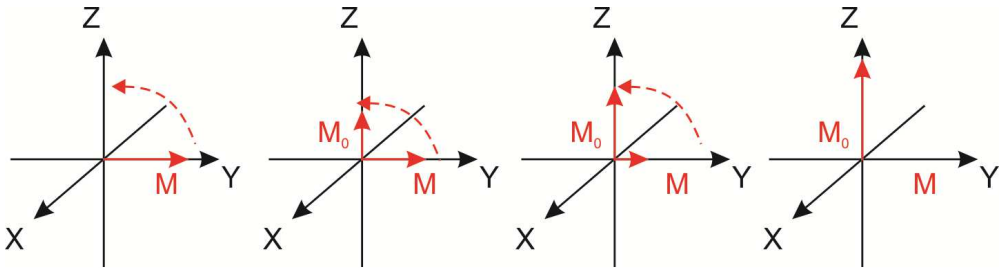

Figure 11 – The recovery of the thermal equilibrium state of the magnetization (M_0) or return of the magnetization is followed by a magnetization (M) decrease in the transverse plane.

For high T_1 values, the interaction is low and the system reaches equilibrium slowly. For low T_1 values, interaction is strong and equilibrium is reached quickly. A $5T_1$ is required for magnetization return to 99% of its equilibrium (Figure 12).

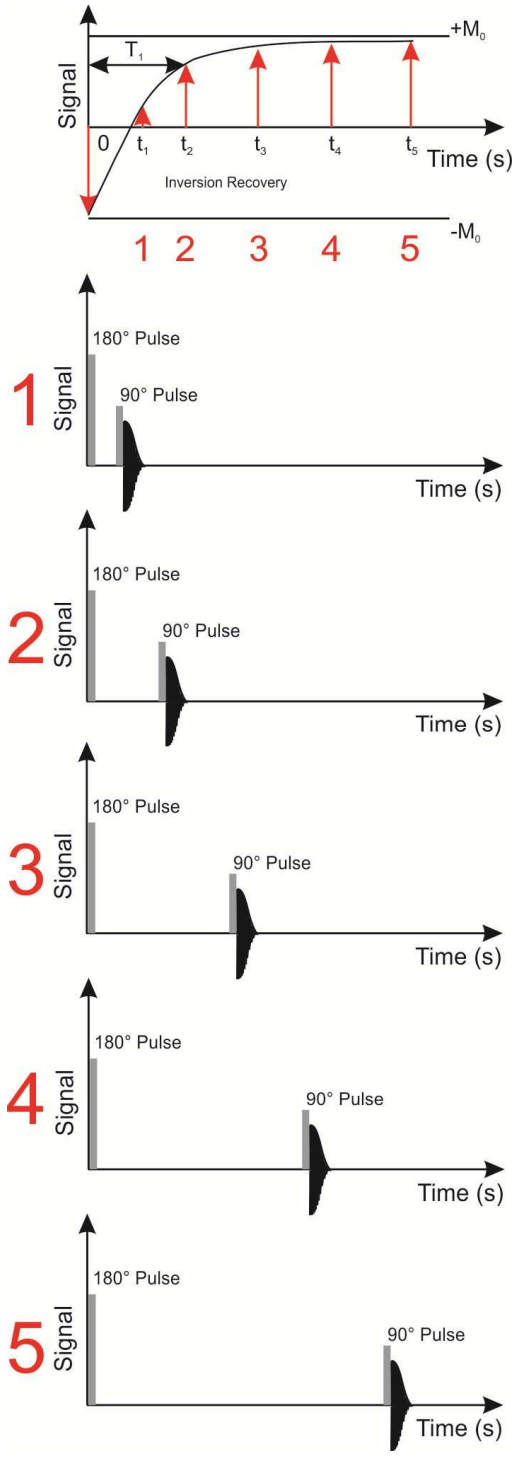

Figure 12 – Behavior of longitudinal magnetization; a) When there is no magnetic field, proton spins are randomly oriented, resulting in a zero magnetization; b) when the field B_o is applied in the z-direction at t = 0, the system magnetization increases until it reaches the equilibrium point M_0.

3.1.1.1 Measuring T_1

Inversion-Recovery (IR) is the most used technique for measuring the longitudinal relaxation time, T_1. It consists of applying a 180º pulse to invert the magnetization vector M_0

from the +z to the -z-axis. The nuclei are then aligned forming a net magnetization (vector sum of the individual magnetic moments). As the magnetization vector continues in the longitudinal position, there is no transverse component and hence no measurable signal. Then, after a time interval t_i long enough to align the longitudinal magnetization, an RF 90° pulse is applied to invert the magnetization to the transverse xy-plane, where the signal is read. The RF pulse is proportional to the magnetization magnitude along the +z-axis. Several measurements with different t_i are performed until the magnetization relaxes and reaches equilibrium completely. For a relatively small t_i, the magnetization value measured is $-M_0$. The signal-to-noise ratio of the NMR signal is improved by calculating the signal mean after repeating the procedure several times (Figure 12).

3.1.2 **Transverse relaxation time T_2**

The previous section showed that to perform an NMR measurement, it is necessary to apply an RF pulse 90º from the magnetic field B_0, generating transverse magnetic components. These components reach their maximum value at $\theta = 90º$ and cancel at $\theta = 180º$. By suspending the 90° RF pulse, the magnetization of bulk fluids will disappear on the xy-plane, relaxing to equilibrium over time according to the equation:

$$M_{xy}(t) = M_0 \, e^{-t/T_2} \tag{17}$$

where $M_{xy}(t)$ is the magnetization component in the xy-plane at time t, M_0 is equilibrium magnetization and T_2 is the bulk fluid relaxation time, or the time required for the transverse plane magnetization to reach the initial value (Figure 13).

The amplitude of the NMR signal decays over time by loss of phase coherence among spins (spin-spin relaxation). During the interactions, the precession frequency of some nuclei becomes delayed while others accelerate, increasing the disorder. There is no energy transfer to medium in this process, only interactions with other particles.

When $t = 0$, the initial amplitude M_0 is sensitive to water content and hence T_2 can be interpreted through the pore space properties. However, the NMR signal obtained due to the magnetization decay after the applied 90º RF pulse is also affected by the magnetic susceptibility difference at the fluid-grain interface and inhomogeneities inherent to the external magnetic field B_0:

$$\frac{1}{T_2^*} = \frac{1}{T_{2B}} + \gamma \Delta \chi B_0 + \gamma \Delta B_0 \quad (18)$$

where γ is the gyromagnetic constant, B_0 is the external magnetic field, $\Delta\chi$ is the difference in magnetic susceptibility at the pore-grain interface.

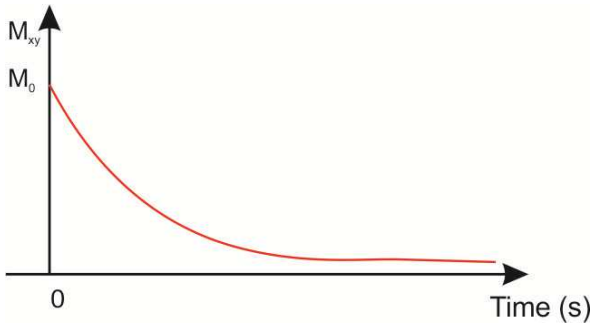

Figure 13 – NMR transverse relaxation decay from the water in the porous rock due to return of magnetization to its equilibrium condition after suspending the 90º RF pulse.

T_{2B} is the natural transversal relaxation time of the sample without any interference. Any process that causes loss of transverse magnetization, including the magnetization return to the z direction, contributes to T_2^*.

The spectrum in the frequency domain can be obtained through the Fourier transform. In general, long and short FIDs generate, respectively, narrow and broad peaks in the Fourier transform curves, indicating a heterogeneous field distribution. Magnetic susceptibility interferes with field homogeneity. Therefore, when a rock has high magnetic susceptibility, the FID signal is short, and the Fourier Transform peak is broad (Figure 14).

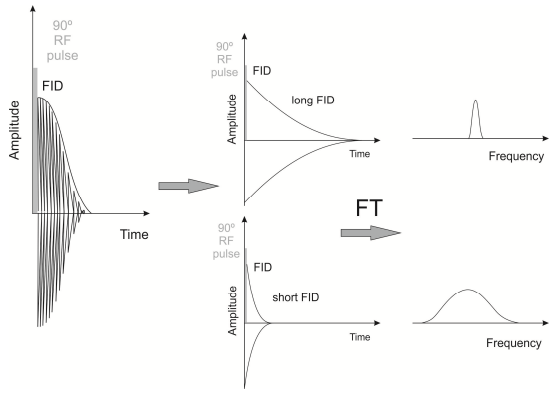

Figure 14 – After the 90º pulse, the FID is generated and the Fourier transform shows how efficient the spins are precessing at a given frequency. For a long FID, the spins precess longer at the same frequency, taking time to relax so that the Fourier transform peak is narrow. For a short FID, the spins lose their phase coherence faster due to the field inhomogeneity and, therefore, the Fourier transform peak is broad (adapted from Dunn, 2002).

The interpretation of the FID is very complex. Therefore, multi-pulse sequences are used to separate these effects.

3.1.2.1 Measuring T_2

The most widely used technique for measuring the transverse relaxation time T_2 was developed by Carr-Purcell-Meiboom-Gill in the 1950´s years and has been known as CPMG. The experiment consists of applying a 90º RF pulse followed by several 180º pulse applications. The 90° pulse inverts the magnetization to the xy plane, and when it is switched off, the magnetization components begin to lag in the xy-plane due to interactions between the spins and diffusion in an inhomogeneous field. After a certain time *t*, a second 180° RF pulse is applied to reverse the precession movement. By reversing the movement, the effect of the heterogeneities on the individual protons is expected to be compensated after one cycle. In addition to the signal emitted as a function of the 90° pulse (FID), a second signal also appears at 2*t*, which is the echo of the first and called the spin echo or "spin signal," resulting from this new phase. The echo shape is determined by the FID shape, such that the spin echo, which comprises 2 FIDs ("back-to-back") is centered in the TE time (inter-echo time: time between π pulses and identical to time between two echoes) = $(2T_E)/2$, after the excitation pulse.

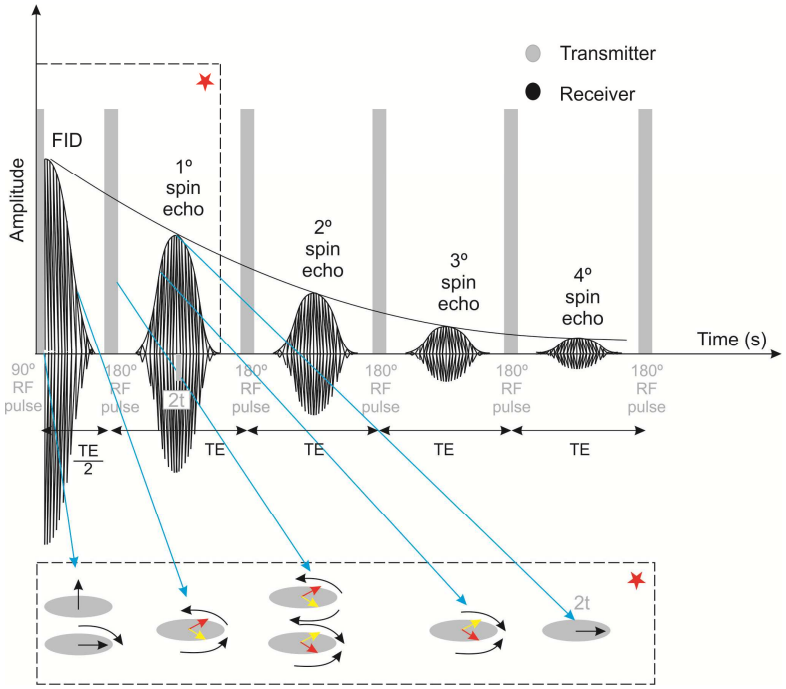

Figure 15 – First, a 90º radiofrequency pulse is applied. As the pulse is turned off, the protons begin to precess and magnetization decay occurs in the xy plane. An induced current is picked up by the coil that measures transverse magnetization, which picks up the decreasing

exponential signal, the free induction decay (FID). At time t, a 180° pulse is applied to revert the phase angles. By repeatedly applying 180º RF pulses, separated in time by TE, an echo train is formed. The decay of the amplitude of the echo signals is called relaxation time T_2.

By repeatedly applying 180º RF pulses, separated in time by TE, an echo train is formed. The echo signal in 2t has maximum refocalization. Since the reversal is not perfect, the echo signal is less than the initial value until the refocalization becomes inefficient. The amplitude decay of the echo signals is called relaxation time T_2 and can be measured even in an inhomogeneous magnetic field (Figure 15).

With refocalization, only the interactions between the magnetizations of the spins are represented in the decay. The inhomogeneity of magnetic field and/or $\Delta\chi$ are repaired and the effects of diffusion can be minimized by choosing a short echo time.

3.1.3 **Translational diffusion D**

Molecular diffusion is defined as the random translational motion of the fluid molecules due to the thermal agitation of the constituents of the medium. It may be interdiffusive, when migration occurs between areas of different concentrations, or self-diffusive, when migration occurs in the same volume with the same molecular concentration. The diffusion coefficient is defined by:

$$\vec{J} = -D \ \overrightarrow{\nabla} \xi \tag{19}$$

where $\vec{J}$ is the particle flow, D is the diffusion coefficient, and ξ is the particle concentration.

The translational diffusion coefficient (D) is a measurement of how easy it is for a molecule to move in a given medium. Due to collisions caused by pore walls, the movements of these molecules are restricted, causing a variation in D. This coefficient, therefore, depends on the medium viscosity, temperature, molecule size, and the diffusion time before relaxing. The relationship between the diffusion coefficient and the distance traveled by the molecule during the process is given by:

$$<r^2> = 2d\ D(t)t \tag{20}$$

where r^2 is the mean square distance a molecule diffuses over time t, d is the dimensionality of the system (commonly 3), D is the molecular diffusion coefficient.

$D(t) = D_0$ for unrestricted medium and time is an independent bulk constant, which will depend only on the type of the fluid and the diffusing molecule (e.g. $D_{0water} = 2300\mu^2/s$). In a confined geometry, D(t) is time dependent, so it carries information of pore walls according the time of molecules are diffusing. At short time, small fraction of the molecules contacts the pore wall, so it carries informations about the S/V of pore, while the long time limit of D(t), the molecules move among pores and throat pores, carrying informations about geometry and tortuosity. When the pore is closed, the diffusion coefficient is zero, while in connected systems the finite value is reduce from its free value by the tortuosity (α), according the equation (Hurlimann et al, 1994; Sen, 2004):

$$\frac{D(t)}{D_0} = 1 - (1 - \frac{1}{\alpha}) \quad (21)$$

The more restricted open geometry has large tortuosity and wide pore in open geometry has tortuosity near 1.

3.1.3.1 Measuring D

For measuring D, it is necessary to apply a magnetic field gradient that results on different values of magnetic field according to the position on the sample (Figure 16) (see more details on section 3.1.4.3.

The sequence to measure D is called *Pulsed Field Gradient Stimulated Echo – PFG-STE* (Tanner, 1970). The PFG-STE consists of two combined RF-gradient pulses sequence, which are separated by one pulse of RF. In the first sequence, the gradient pulse (with intensity g and duration δ), spatially encode the initial phase (or equilibrium phase) on the static magnetic field. After applying this second RF pulse, diffusion may occur without transverse relaxation, since the magnetization is now in the longitudinal axis. In the second RF-gradient pulses sequence, the magnetization is shifted to the transverse plane and the gradient pulse spatially encode the final (or post-diffusion molecular phase) initial phase. In the presence of diffusion, the measured echo intensity decreases due to loss of coherence. On the contrary, if there is no diffusion, the signal strength is the same as that after the first pulse, since there is no loss of phase coherence (Figure 17).

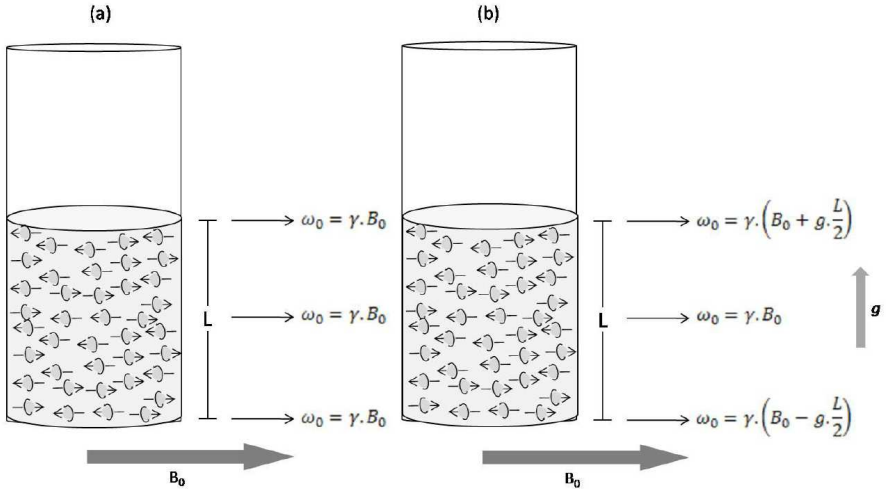

Figure 16 – Sample within (A) no magnetic field gradient and (B) magnetic field gradient. Observe that in A the Larmour frequency is the same for the whole sample, whereas it changes with the sample position in B (Carneiro, 2012).

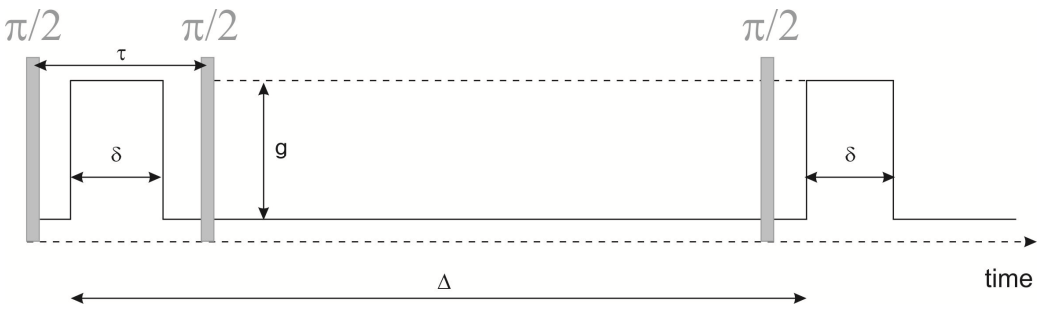

Figure 17 – PFG-STE sequence for D-T_2 experiment which two combined RF (π/2) - gradient pulses (with duration δ and intensity g) sequence, which are separated by one pulse of RF applied τ time after the first RF pulse. Δ is the diffusion time (adapted from Mitra et al., 1993).

3.1.4 **Nuclear magnetic resonance applied to petrophysical studies**

As described before, the magnetization which is proportional to bulk volume of water in the sample decays through two relaxation times constants: T_1 and T_2. In this work, we used only the T_2 relaxation times because this parameter is the one commonly used in NMR borehole tools during oil and gas exploration.

In geological materials which have a range of pore sizes, the total relaxation is the sum of the decay signals of each pore size, the individual relaxation occurring independently for each pore (Figure 18):

$$M(t) = \sum_{i=1}^{n} Mi \exp(-t/Ti_2) \quad (22)$$

where M_i is initial magnetization of the relaxation component, T_2 is the decay time constant and $M_z(t)$ is total relaxation (Gauss) at time *t*.

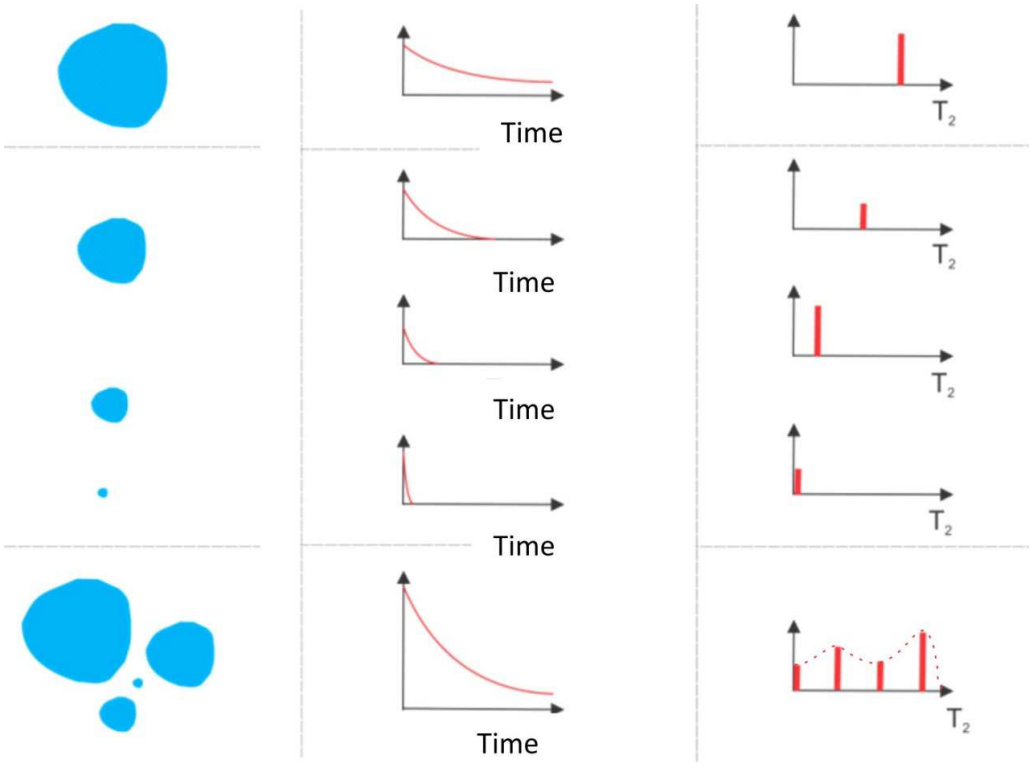

Figure 18 – The relationship between pore size and the NMR response. A water-saturated pore (upper left) has a single T_2 value (upper center) whose spin-echo train exhibits a simple exponential decay (upper right). As the pore size decreases (left center), the T_2 value also decreases (central center) and the exponential decay of the spin-echo train becomes faster (center right). Several pores (lower left) have several T_2 values (bottom center), depending on pore size and therefore the composite spin-echo train exhibits multiexponential decay (lower right), which also depend on pore sizes (adapted from Coates et al., 1999).

In studies of NMR, the magnetization decay can be inverted to T_2 relaxation time distribution through the Inverse LaPlace Transform (ILT) (Figure 18). Depending on the input data, this technique can generate different results, especially in data from NMR logging surveys. In order to stabilize the signal, a regularization algorithm was introduced by the NMR industry and it is possible to obtain a good relationship between T_i distribution and pore size distribution.

By conducting a CPMG sequence, the T_2 relaxation process can be affected through three mechanisms: bulk relaxation (T_{2B}), surface relaxation (T_{2S}) and molecular diffusion relaxation (T_{2D}) and the equation 18 becomes:

$$\frac{1}{T_2} = \frac{1}{T_{2B}} + \frac{1}{T_{2S}} + \frac{1}{T_{2D}} \quad (23)$$

3.1.4.1 Bulk relaxation

Intrinsic relaxation, or bulk fluid relaxation, occurs when the hydrogen protons relax before coming into contact with the pore wall, as a function of local magnetic field fluctuations caused by motion of neighboring nuclei. This relaxation is controlled by the fluid intrinsic properties, such as viscosity, chemical composition (mainly the concentration of dissolved paramagnetic ions such as Mn^{+2} or Fe^{+3}), temperature, pressure and pH. When more than one immiscible fluid is present in the porous medium, spins of the non-wetting fluid tend to relax by bulk relaxation, since they are not in contact with the grains. In turn, when only one saturated fluid is present, the bulk relaxation commonly can be neglected since it is dwarfed by the other relaxation mechanisms. In viscous fluids, the low diffusion mechanisms associated with short surface time allows the bulk relaxation to predominate. When this occurs, for low magnetic field, $T_1 = T_2$ (for water at room temperature, it is 3s).

3.1.4.2 Surface relaxation

Surface relaxation occurs when the spin-spin interactions between water protons find the paramagnetic sites on the solid surface. The diffusion of protons has no significant effect on the nuclear precession movement when the spins are subjected to a homogeneous magnetic field. Therefore, independent of the Brownian motion, the spins continue to precess around B_0 with Larmor frequency ω_0. When the molecules of the wetting fluid collide with the pore/grain wall, the spins relax by transferring energy to the surface and, consequently, may realign their magnetization with B_0 faster. The efficiency of these mechanisms depends on some factors such as mineralogy (ions present at the rock-fluid interface), pore size (S/V ratio), distribution and relaxation capacity of wetting fluid molecules, independent of temperature and pressure.

Relaxation does not occur in every collision, but a greater number of collisions increases the likelihood of proton relaxation. When the molecules travel large distances within the porous space during a time *t* before relaxing it is said that they are in a fast diffusion system. This condition was established by Brownstein and Tarr (1979) through the following equation:

$$\kappa = \frac{\rho_2 \alpha}{D} \quad (24)$$

where ρ_2 is the transversal surface relaxivity which is defined by "ability of the surface to cause relaxation of proton magnetization (Kenyon (1997)", α is the distance which the proton can diffuse towards the grain surface; generally we assume it is equal the ratio divided by three for spherical pores since it equivalent to V(volume)/S(surface area) of pores; and D is the coefficient diffusion of proton in the water. If κ is >>10, the system is in slow-diffusion regime which the proton does not travel the entire pore space before relaxing at pore surface; if κ is <<1, the system is in fast-diffusion regime which the proton can travel to relax at grain surface during the time of NMR experiment; if 1< κ < 10, the system is in intermediate diffusion regime. Ryu and Johnson (2009) suggest that << 1 is equivalent to < 0.1. If the water relax in the fast diffusion regime, a direct relation can be stablished between T_2 time and S/V or pore size (Kenyon, 1997):

$$\frac{1}{T_2} = \rho_2 \, (S/V) \tag{25}$$

The Figure 19 shows this relationship. If the pore size is small (higher S/V ratio), the probability of H^+ collides with the pore surface is high, increasing the likelihood of rapid relaxation and shortening the relaxation time.

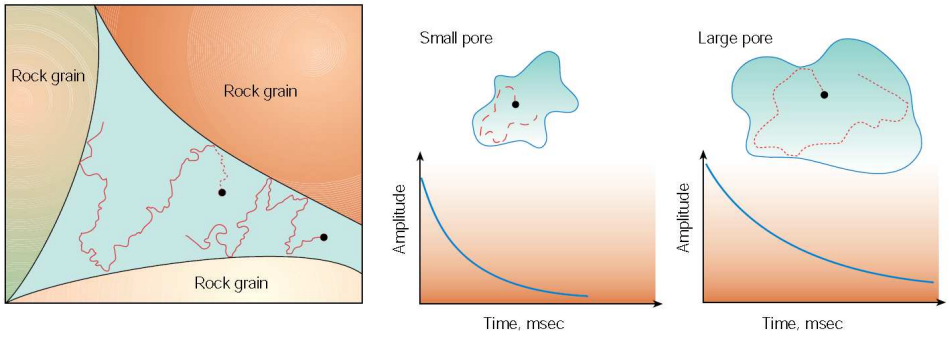

Figure 19 – The spins of H proton in the water-filled pore are diffusing (left). If the pore is small, the spins easily "feel" the magnetic properties of surface grain and, hence, increasing the probability that magnetization relax more quickly (centre). If the pore is big, the probability of spins "feel" the grain surface is less and the magnetization decays slowly (right) (Schön, 2014).

The presence of paramagnetic or ferromagnetic particles on the grain's surface contributes to fast relaxation, since they have a larger magnetic moment than the proton. In this case, the nuclei relax even before interacting with the surface, so they lack the same freedom to move to other regions. When the magnetic susceptibility of the surface is very high, the magnetization becomes higher in the pore center than on its surface (Figure 20).

When this occurs, surface relaxation dominates over diffusion and hence the system is on the slow diffusion limit.

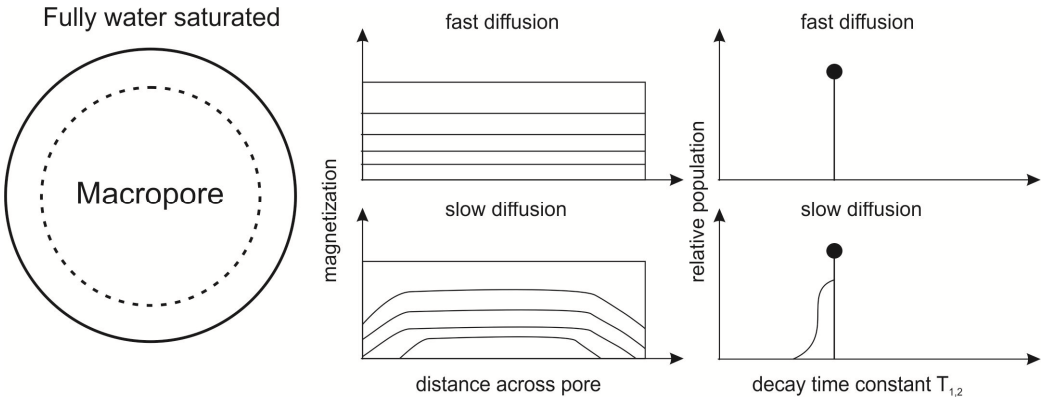

Figure 20 – Scheme showing the magnetization across the macropore. The centered-upper part shows the uniform magnetization in whole pore, while the underside shows the magnetization variation in pore surface and center of pore (adapted from Straley, 1995).

Resuming, three assumptions are required to obtain a relationship between T_2 times and S/V ratio: (a) the pores have to be effectively isolated, causing each pore relax independently of the others; (b) the system has to be in fast-diffusion regime; (c) the surface relaxivity has to be uniform across the entire surface of pore space.

3.1.4.3 Molecular diffusion relaxation

In a non-homogeneous magnetic field, the molecules diffuse to areas of different magnetic field intensities, making the nuclei precess at different frequencies, hence losing the phase coherence and relaxing. The molecular diffusion rate is described by:

$$\frac{1}{T_{2D}} = \frac{D(\gamma G T_E)^2}{12} \tag{26}$$

where: $\frac{1}{T_{2D}}$ is the molecular diffusion rate, D is the molecular diffusion coefficient, γ is the gyromagnetic constant, G is the magnetic field gradient (G/cm), and TE is the inter-echo time used in the CPMG sequence.

Qualitatively, we can analyze the T_{2D} contribution measuring the dependence of T_2 with different values of T_E (equation 26). Kleinberg and Vinegar (1996) illustrated this behavior very well. In a CPMG sequence, when the ^1H core is subjected to a RF pulse, the

magnetization is inclined to the transverse plane. The nucleus is in position A with defined magnetic field strength B_0 when the pulse ceases. As it diffuses, the nucleus moves from A to B, and the small variation of the magnetic field causes the Larmor frequency to change slowly as well. The 180º pulse is performed when the nucleus reaches B to reestablish phase coherence. The nucleus continues to diffuse until it reaches C in time T_E. If the precession movement is faster between A and B than between B and C, phase recovery in T_E was not efficient, making the dephasing irreversible (Figure 21). In a diffusion experiment, the spin amplitudes of the echoes can be monitored by selecting the appropriate inter-echo spacing for the magnetic field gradient so that the diffusion effects can be increased or minimized. When the inter-echo spacing decreases, the diffusion contribution to T_2 relaxation is minimized.

Not all minerals contribute to the magnetic field gradient. It arises only when a high magnetic susceptibility contrast occur in the grain-fluid interface:

$$G= \Delta B_0/r \tag{27}$$

$$\Delta B_0=\Delta\chi B_0 \tag{28}$$

where r is the distance traveled by the proton which is dependent from pore geometry, ΔB_0 is the varying external magnetic field and $\Delta\chi$ is the varying magnetic susceptibility.

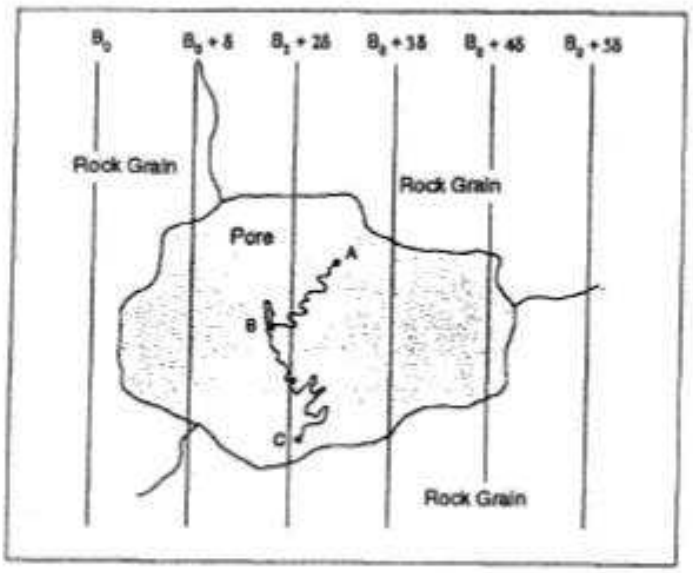

Figure 21– Diffusion of molecules submitted to a heterogeneous field during the NMR experiment. See details in the text (Kleinberg and Vinegar, 1996).

4 Methods

Laboratory techniques as Helium and fluid saturation porosimetry (section 4.1.1 and 4.1.2), Helium permeability (section 4.2), transmitted-light optics (section 4.3), micro-CT (X-ray micro computed tomography) (section 4.4), mercury injection (section 4.5), XRD (x-ray diffraction) (section 4.6), magnetic susceptibility and hysteresis analysis (section 4.7), besides NMR (nuclear magnetic resonance) (section72 4.8) are used here to characterize the samples.

4.1 Porosity (ϕ)

4.1.1 **Helium porosimeter**

The method is based on the law of Boyle-Mariotte or the "principle of expansion of gases". It is defined for closed systems (or T constant), the product between the gas volume and its pressure remains constant before and after an interconnection of two systems:

$$P_1V_1 = P_2V_2 \tag{29}$$

where P_1 is the initial pressure, V_1 is the initial volume, P_2 is the final pressure, and V_2 is the final volume of a gas for constant temperature.

There are two chambers in the porosimeter: the first one is known as the reference cell volume (V_b) and the second one (V_a) is where the sample (V_{bulk}) is inserted and is known as the sample cell, which is limited at its top and base by two movable pistons adaptable to sample length. The two chambers are connected to each other by a connection valve, which initially is closed. The first step consists in injecting the gas into the reference cell (V_1 or V_b) with pressure P_1 of about 200 (or 100) PSI using the valve located between the helium tank and reference cell. Then, the sample is inserted into sample cell and the valve between sample cell and atmosphere is closed — a confining pressure of 400 PSI is required in the sample cell in order to eliminate any void space between the sample and the wall of the cylinder. The third step of measurements is to open the connection valve, which is located between the reference and the sample cell. The gas will slowly equilibrate through the entirety of both cells. The gas will penetrate into the pores of sample and the pressure will decrease to a new equilibrium value (P_2). Due to gas expansion, P_2 will always be less than P_1 and the volume of voids is provided by (Anovitz and Cole, 2015):

$$V_v = V_{bulk} - V_a - V_b \frac{P_2}{P_2 - P_1} \quad (30)$$

where V_v is voids volume, V_{bulk} is sample volume, V_a is volume of second camera, V_b is reference cell volume, P_1 is initial pressure and P_2 is equilibrium pressure.

In this thesis, the porosity data were provided from Petrobras S/A which used the Wheaterford Laboratories DV-4000 porosimeter using 100 PSI.

4.1.2 **Fluid saturation**

The effective porosity was obtained by saturation (or imbibition) of the rock with a wetting fluid. In general, brine or fresh water is used for these experiments, but other types of liquids as toluene or dichloromethane can also be used (Glover, 2005; Anovitz and Cole, 2015). The experiment consisted of a sample being placed in an oven at 50 °C for minimum 24 hours and weighed. This procedure was repeated several times for some hours until the mass obtained was constant. Then, after the sample was completely dried, it was saturated by immersion in water and subjected to vacuum in a desiccator where it remained for about one hour. During this time, the water was displaced by capillarity in the sample and every half hour the sample was weighed until the (saturated) equilibrium mass was reached. At this point a saturation of 100% is assumed. It is important to remove carefully the excess of water from the surface of the samples and determine the volume with a micrometer or digital caliper (5 measurements are recommended, Andersen et al., 2013).

The porosity can be calculated as follows:

$$\Phi effective = \frac{Vv}{Vt} / = \frac{Vw}{Vt} = \frac{\frac{(Msat - Msec)}{\rho w}}{Vt} \quad (31)$$

where Vv is the void volume; Vt is total volume; Vw is water volume that fills the pores; Msat is the mass of water saturated sample and Msec is dry mass of sample.

This method is not suitable for rocks with expansive clays and poorly cemented (friable) sandstones because there is a risk of breaking the sample during the procedure or causing a mistaken estimate of porosity.

4.2 Permeability (k)

4.2.1 **Helium permeameter**

The permeability measurements using a Helium permeameter are performed through a Hassler chamber which contains a rubber sleever that surrounds the porous medium in an applied confining pressure. The methodology consists in putting the sample in a high gas pressure core holder and then open the valve. The gas will pass through the sample and the pressure decreases. Therefore, the variation of pressure and flow rate can be calculated by Darcy equation that relates to a macroscopic cross-section, to viscosity and fluid pressure gradient (Schön, 2014):

$$K = Q \mu L / A (P_1 - P_2) \quad (32)$$

where K is the permeability of rock (Darcy); Q is the flow rate (cm/s); L is sample length (cm); μ is the viscosity of the fluid (cP); A is cross-sectional area (cm^2), and P_1P_2 is the pressure difference in the flow direction.

A Core lab helium permeameter (model n. 3020-124 and serie A7520) from Petrobras/SA was used for measurements in this work.

4.3 Transmitted light optics and scanning electron microscopy (SEM)

Basic petrographic analysis is usually performed in transmitted-light optical microscope, but also it often requires SEM analysis.

Optical microscopy observations of thin-sections were performed to identify the constituent minerals, describe the depositional and diagenetic processes, estimate qualitatively and quantitatively the composition and the textural framework, besides analyzing the porosity system. The quantitative analysis was done by modal analysis (point counting) with at least 300 points.

SEM images were used to identify and characterize the coatings on detrital host grains and measure the size of the micropores. In this work, a INSPECT F50 FEI scanning electron microscope from Instituto de Física de São Carlos, Universidade de São Paulo, was used.

Energy Dispersive Spectroscopy (EDS) was used for semi-quantitative chemical mapping of O, Al, Fe, Mg and Si in the Água Grande Formation sandstones (Topic Section 5.2).

4.4 X-ray micro computed tomography (Micro-CT)

The micro-CT basic system consists of a standard X-ray source, a rotating sample apparatus and a fix X-ray detector. Two configurations are possible: the first is a cone-beam micro-CT, in which the sample can be positioned anywhere between the x-ray source and the detector. So, the resolution will be limited by the focal spot size. In the second, the synchrotron sources are used, so the parallel x-ray beam is detected by scintillator screen, which convert the X-ray beam to light (Cnudde and Boonde, 2013). The digital images were reconstructed using an algorithm (e.g. least squares; see more in Duliu, 1999; Pierret et al., 2002), segmented and 3D matrix of voxels, which is correspondent to the attenuation coefficient, is obtained.

Here, the measurements were performed with a SkyScan 1272 scanner by Bruker (USA) from Instituto de Física de São Carlos, Universidade de São Paulo, and were analyzed using the Bruker μCT software (CTAn). Samples correspond to fragments of about 0.005 cm^3 in volume collected directly from the original samples.

4.5 Mercury intrusion capillary pressure (MICP)

Mercury porosimetry is a widely used technique to characterize the pore space. It provides important information, such as pore throats distribution, median pore throat diameter volume, porosity and specific surface area of rocks. Mercury is a non-wetting fluid for most materials, so to penetrate into the pore space it is necessary to apply a pressure, which is greater than the surface tension of the mercury — equivalent to 484.6 mN / m² (Giesche, 2006; Anovitz & Cole, 2015).

The capillary force through which a grain surface avoids the mercury to penetrate into the pores is:

$$F_E = 2\pi\, r\ \gamma\ \cos\theta \tag{33}$$

where F_E is capillary force; r is pore radius; γ is the surface tension and $\cos\theta$ is the contact angle, which can be calculated by:

$$\cos\theta = \frac{(\gamma_{sv} - \gamma_{sl})}{\gamma_{lv}} \tag{34}$$

where $\cos\theta$ is contact angle, γ_{sv} is surface-vapor tension vector, γ_{sl} is surface-liquid tension vector and γ_{lv} is liquid-vapor tension vector. The pressure required for the mercury to enter through the pores (P) can be obtained by dividing equation 33 by $2\pi r^2$:

$$\frac{F_E}{A} = P = \frac{2\pi r\ \gamma\ \cos\theta}{r^2} = -\frac{2\gamma\ \cos\theta}{r} \tag{35}$$

$$r = -\frac{2\gamma\ \cos\theta}{P} \text{ or } D = -\frac{4\gamma\ \cos\theta}{P} \tag{36}$$

where F_E is capillary force, A is pore area, r is pore radius, assuming circular geometry, γ is the surface tension, $\cos\theta$ is the contact angle and D is pore diameter. Since the pressure is incrementally increased, the mercury volume will be injected into the sample and measured. Assuming $4\gamma\ \cos\theta$ is constant, as the pressure goes up, the mercury infiltrates smaller and smaller throat pores (equation 36 (Webb, 2001).

The porosity can be obtained by the accumulated mercury volume, while the pore throat distribution can be obtained by the logarithmic derivative of pore sizes (Nimmo, 2004):

$$f(r) = \frac{dV}{\log r} \tag{37}$$

where f (r) is pore size distribution, V is volume and r is pore size.

The relation between the throat size, which governs mercury injection technique, and the pore size, which governs the NMR, is widely used in NMR studies (Marschall et al., 1995; Straley et al., 1995; Kleinberg, 1996; Agut et al., 2000, Saidian and Prasad, 2015; Rosenbrand et al., 2014; Li et al., 2018). However, it is valid only when the pore and pore throats are similar or there is a fixed multiplicative ratio between them, which usually is the case in sandstones unless they present significant diagenesis (Kenyon, 1997).

In this work, a Mercury Injection Capillary Pressure curves were obtained using a poreSizer 9320 Micromeritics Instruments Co. from Universidade de São Paulo, Instituto de Física de São Carlos to obtain pore throat size distributions.

4.6 X-ray diffraction (XRD)

Clays are very common components of sedimentary rocks, but identify them is not always simple due to the variable range of physicochemical properties of clay minerals, including their composition, morphology, grain size, swelling and cation exchange (Wilson et al, 2014). Thus, X-ray diffraction is a useful technique to distinguish clays, mainly smectite and its mixed-layer, based on their expansion with ethylene glycol (Beaufort et al., 1997; Wilson et al, 2014).

The method is based on incident monochromatic X-ray in the samples, which are diffracted and detected following Bragg´s Law (Moore and Reynolds, 1989):

$$n\lambda = 2d \operatorname{sen} \theta \tag{38}$$

where n is integer number, λ is the wavelength of electromagnetic radiation, d is the lattice spacing, θ is the diffraction angle. The angle between the incident and diffracted rays will determine the type of mineral since each mineral has it set of d lattice spacing (Moore and Reynolds, 1989).

Here, a Bruker D8 Advance Da Vinci Diffractometer from Instituto de Geociências, Universidade de São Paulo (IGc/USP) was used to identify the types of clays present in the samples.

4.7 Magnetic properties

4.7.1 **Magnetic susceptibility (Sus) and hysteresis analysis**

Magnetic susceptibility can be defined as a measure how much a material is likely to become magnetized (Butler, 2004). When a material is subjected to a H field, it acquires an intensity of magnetization M (or induced magnetization), which is proportional to the applied field, given by:

$$M_i = \chi H \tag{39}$$

where M_i is induced magnetization (A/m), χ is magnetic susceptibility (dimensionless in *Système International* or SI) and H is induced magnetic field (H) (A/m).

According to Equation 39, M_i is directly proportional to the applied field, acquiring positive or negative signal due to direction of magnetization intensity relative to the field. Therefore, all the minerals present in the sample contribute to bulk χ, including ferromagnetic (e.g. magnetite, maghemite), antiferromagnetic (e.g. hematite, goethite), paramagnetic (e.g. Fe-bearing clays), diamagnetic (e.g. quartz, carbonates) (Liu et al., 2012) minerals. Among them, the ferromagnetic and antiferromagnetic minerals acquire a remanent magnetization in addition to the induced magnetization.

Hysteresis loop allows one to analyze the induced magnetization behavior M with applied magnetic field of minerals H. Applying an increasing magnetic field from a initial stage where H = 0 and M = 0, the magnetization will increase until it reaches its maximum point, which is called saturation magnetization (Ms). At this point, all the moments are parallel and aligned with the applied field and even if the applied magnetic field. Decreasing the applied field until zero, the magnetization could return to zero or not. When the magnetization does not return to zero, the material has acquired a saturation remanent magnetization (Mrs). Then, an opposite magnetic field is applied until the magnetization reaches zero; this point is known coercivity force (Hc). The field that brings the saturation remanent magnetization to zero is known as the remanent coercivity (Hcr) (Figure 22) (Butler, 2004).

Minerals can be classified according to their behavior under an applied field (Figure 23). Therefore, (Tauxe et al., 1996; Dunlop and Ozdemir, 1997; Butler, 2004; Liu et al., 2012):

a) Diamagnetic behavior: have negative magnetic susceptibility and do not present hysteresis. The diamagnetic substances acquire magnetization of weak intensity and opposite to the direction to the field, allowing a negative signal to be attributed to their magnetic susceptibility. Every material presents diamagnetism. Graphite, quartz, feldspars and anhydrite are examples of minerals that present exclusively this behavior (Figure 23A).

b) Paramagnetic minerals: when an external magnetic field is applied, a small induced field is acquired parallel to that field and when the magnetic field is zero, the magnetization is reduced to zero. The curve is actually a positive inclined line (Figure 23B). The paramagnetic present low induced magnetization is still weak, with a sense equal to that of the applied field, producing a positive magnetic susceptibility. The most common paramagnetic minerals are the Fe-bearing minerals, including olivine, pyroxene, biotite, pyrite, clays and, usually, metallic conductors.

Some elements such as iron, cobalt and nickel have a strong magnetic interaction between the constituent atoms and may present spontaneous magnetization (i.e. ferromagnetic behavior). After a certain grain-size ferromagnetic materials can be subdivided into magnetic domains whose distinct regions are randomly orientated due to energy minimization. The magnetic susceptibility of ferromagnetic minerals is 10^6 times stronger than that of diamagnetic and paramagnetic minerals. The temperature at which a material loses its ferrimagnetic characteristic and begins to behave as a paramagnet is called the Curie temperature. There are four classes of ferromagnetic behavior:

- Ferromagnetism (*strictu sensu*): atoms have strong parallel interactions among adjacent magnetic moments, contributing for the net magnetization. Ferromagnetic minerals are not found in nature (Figure 23G).

- Ferrimagnetism: the interaction among adjacent magnetic moments is antiparallel, but the magnetic moments of the different sublattices are unequal, resulting in a non-null spontaneous magnetization (Figure 23H). Examples of ferrimagnetic minerals are: magnetite and pyrrhotite.

- Antiferromagnetism: the interaction among ions is antiparallel and neighboring magnetic moments are equal and opposite, resulting in a zero total magnetization. Like the ferromagnetic minerals, the antiferromagnetic ones lose their antiferromagnetic properties to a certain temperature, called temperature of Néel (Figure 23I). An example of this behavior is ilmenite.

- Parasitic ferromagnetism: when magnetic mineral contains imperfections or slight distortions (less than 1°) in their crystalline lattice, the magnetic moment of sublattices are not exactly antiparallel. A perpendicular weak magnetization to the orientation of the spins is then generated. Parasitic ferromagnetic materials have typical characteristics of ferromagnetic materials, such as hysteresis, spontaneous magnetization and Curie/Neel temperature (Figure 23J). A very common example is hematite.

It is worth mentioning that an interpretation of a hysteresis curve is not always easy since diverse magnetic minerals assemblages are present in the sample. Therefore, diverse magnetic minerals, which present different physical properties, are reflected in hysteresis loops, resulting in a distorted hysteresis curves (Tauxe et al., 1996).

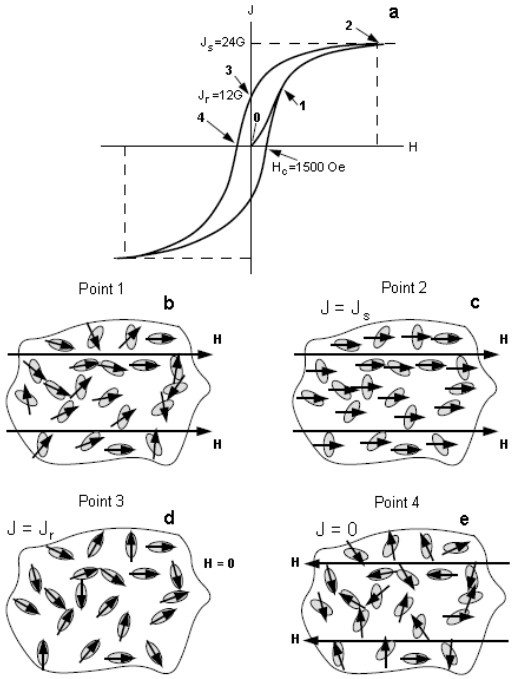

Figure 22 – A) The hysteresis loop shows the field dependence with the induced magnetization. B) In the Point 1, the magnetic moments begin to align to magnetic field; C) In the point 2, all the magnetic moments are align to magnetic field, D) When no magnetic field is applied, the magnetic moments are randomly oriented, but the sample acquire an important magnetization; E) When the opposite magnetic field is applies for more time, the magnetization goes to zero (Butler, 2004).

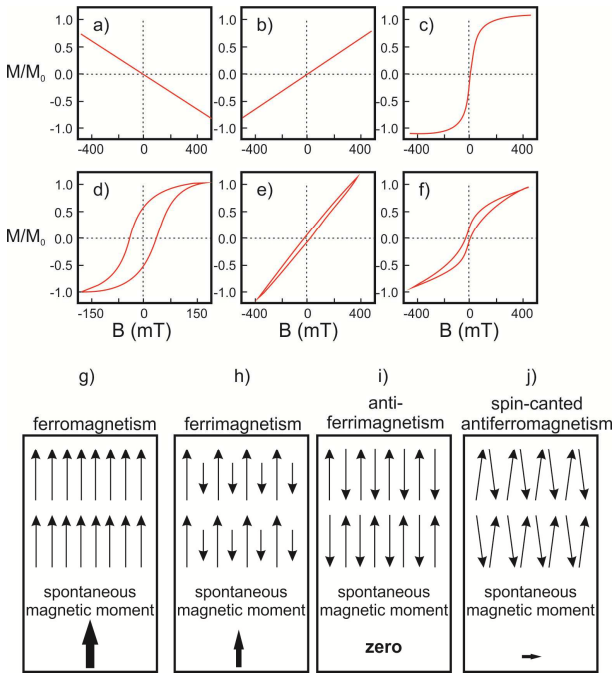

Figure 23 – Magnetic hysteresis cycles with different behaviors: (a) diamagnetic, (b) paramagnetic, (c) superparamagnetic (eg, basaltic submarine glass), (d) uniaxial, monodomain, (e) magnetocrystalline, single domain, simple domain. Adapted from Tauxe et al., 1996; Dunlop, 1997; Tauxe 2005)

In this thesis, I used the Susceptmeter KLY-4S-Kappabridge by AGICO operating at 976 Hz at the Laboratório de Paleomagnetismo da Universidade de São Paulo (USPmag) for magnetic susceptility measurements. The hysteresis loops measurements were performed in a Princeton Measurements Corp. vibrating sample magnetometer with a peak field of 1T also from USPmag.

4.7.2 **Isothermal Remanent Magnetization (IRM)**

The IRM is the remanent magnetization (or permanent magnetization) obtained when we apply an instantaneously large magnetic field in a room temperature. As we increase the field, the sample is remagnetized along the applied field direction until the saturation. The saturation isothermal remanent magnetization (SIRM) and the field at which the magnetization attains half of saturation $B_{1/2}$ are not equal for all minerals, varying according to their remanent coercivity (or the resistance of the magnetic mineral to being permanently magnetized), the composition, the grain size and the interactions between the magnetic grains (Lowrie, 2007). Generally, the SIRM of ferrimagnetic minerals (magnetite) is reached with smaller fields ($\leq$ 0.3T), while the antiferromagnetic (hematite and goethite) minerals need larger fields (>1T) (Lowrie, 2007; Liu et al., 2012), allowing the identification of the predominant magnetic minerals.

By fitting cumulative log-gaussian functions (CLG) to IRM curves, we can determine the contribution of each magnetic phase (Robertson and France, 1994). The CLG consists method of simultaneously fitting different CLG curves (one for each magnetic phase) to the IRM acquisition curve of the sample. The quality of the fitting is analyzed qualitatively by comparing the sum of individual CLG curves to the linear acquisition plot (LAP), the gradient of acquisition plot (GAP) which is the derivative of CLG curves, and the standardized acquisition plot (SAP), which is a probability scaled IRM curve (Kruiver et al., 2001).

In this work, a pulse magnetizor MMPM10 from Magnetic Measurements Ltd. was used, reaching maximum field of 1 T in the 1.25 cm diameter coil in which the samples were submitted to inductor fields ranging from 0.01 T to 1 T through 30 magnetization steps. The IRM was acquired at each step was measured on a 755-1.65 DC SQUID magnetometer (2G Enterprises). Data analysis was done from cumulative-Gaussian curves (Robertson and France, 1994) using the spreadsheet compiled by Kruiver et. al. (2001).

4.7.3 **First-Order Reversal Curve (FORC)**

The FORC diagrams consist of a set of partial hysteresis loops which are used to define qualitatively the presence of magnetic phases with varying domain states, besides the possible presence of magnetostatic interactions (Zhao et al., 2017). The sample is firstly magnetized until it reaches the saturation through the high positive applied field (B_{sat}). This field is then decreased to a reverse field (B_r). As we apply a series of evenly spaced applied fields (δB) from B_r to B_{sat}, the first-order-reversal curves are formed. The two consecutive magnetization measurements within a FORC series are used to obtain gridded magnetization measurements, creating a FORC diagram or a mixed second derivative diagram (Roberts et al., 2014) (Figure 24).

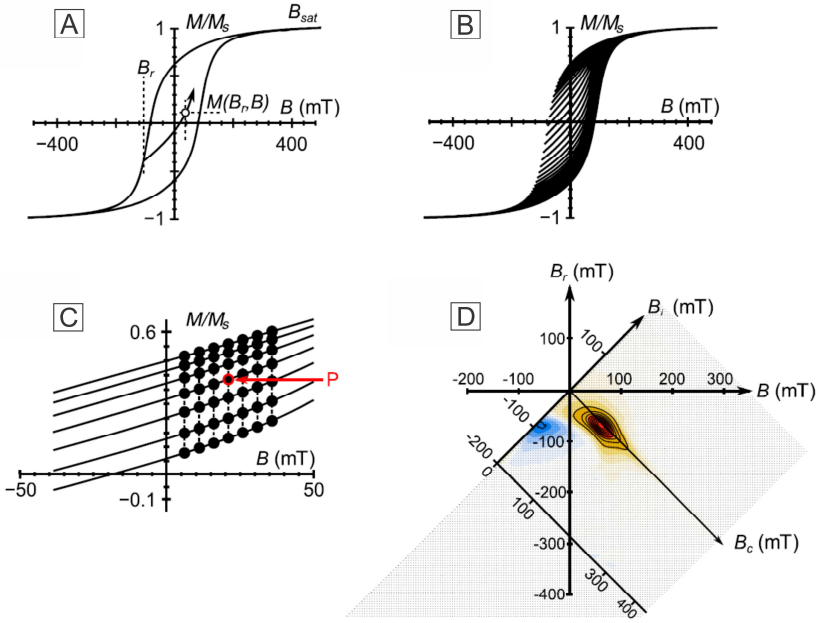

Figure 24 – The FORC measurement begin at B_r point. When the magnetic field is applied, the induced magnetization is measured along the M(Br, B) line; B) Set of FORC; C) The grid used for calculate the FORC distribution ρ(Br, B) which is used a smoothing for consecutives FORCs; D) the FORC diagram showing the magnetic response of all particles with irreversible magnetization where the relationship between {Br,Bc} are transformed to terms of coercivity and magnetic interaction field distribution {Bi,Bc} (Roberts et al., 2014).

The Figure 25 shows some examples of FORC diagrams for different types of magnetic behavior.

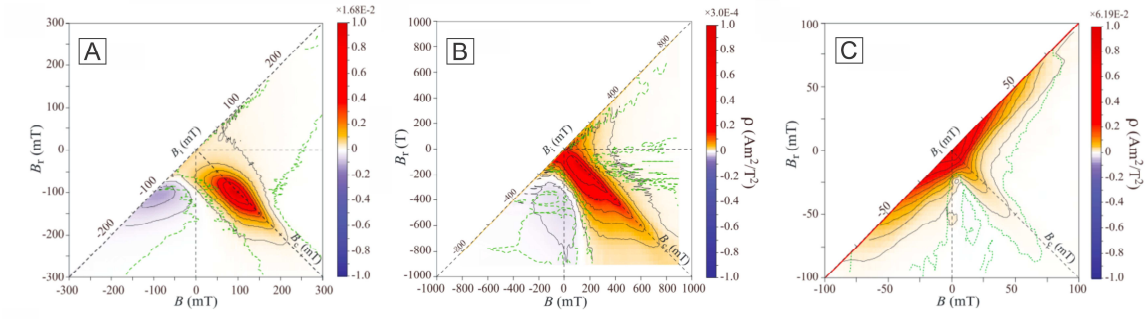

Figure 25 – Examples of FORC diagrams: A) single-domain magnetite sample; B) single-domain hematite sample; C) multi-domain magnetite sample (~120 μm) (Zhao et al., 2017).

4.8 Nuclear magnetic resonance (NMR)

The theorical fundaments of NMR were described in chapter 3. Therefore, this topic consists of specifications of experiments.

1H NMR measurements were performed using two Redstone Tecmag spectrometers, one operating at 2 MHz and another at 85 MHz, using a permanent magnetic (0.047T) and an Oxford Instruments superconductor magnet (2 T), respectively, both from Instituto de Física de São Carlos, Universidade de São Paulo. A LapNMR^{TM} Tecmag spectrometer operating at 20 MHz were performed for only two samples from Fontainebleau sandstones due to equipment and sample size limit.

The T_2, T_2-T_2 and D-T_2 measurements were done on samples saturated with fresh water since all the samples do not present expansive clays. Tests with brine water also were done for Recôncavo Basin samples. Inversion-recovery (IR), Carr-Purcell-Meiboom-Gill (CPMG), T_2-Filtered T_2-T_2 Exchange (T_2F-TREx) and *Pulsed Field Gradient Stimulated Echo (*PFG-STE) + CPMG sequences were used for for T_2, T_2-T_2 and D-T_2 analysis, respectively (Tanner, 1970, Song et al., 2002; Mitchell et al., 2013; D'Eurydice et al., 2016; Montrazi etal., 2018).

The CPMG measurements were performed with echo times of 200 μs with 32 averages for each experiment for all samples. Tests with diverse echo times also were done using 200, 250, 300, 400, 500 and 750 μs.

The T_2-T_2 experiments were performed in Fontainebleau sandstones at 85 MHz with three and four filter times (D'Eurydice et al., 2016), defined by multiples of echo times for

FB83 (3, 16, 200, 2500) and for 155 (3, 16, 300) samples. The number of scans and echo time used were 8 and 250 μs, respectively. The storage time t_s was swept in 16 logarithmic steps. The measured exchange curves were analyzed using the method described by Montrazi et al. (2018). The results of T_2-T_2 exchange experiments from Recôncavo Basin sandstones were unsatisfactory due to the effect of magnetic susceptibility.

The 2D D-T_2 experiment was performed on the 2-MHz equipment, with time to the fixed stimulated echo of 6 ms, diffusion time of 40 ms, and time to the Hahn echo of 200 μs.

To convert the decay functions into a T_2 distributions we used the inverse Laplace transform (ILT) implemented in an in-house program developed in the NMR Group. The Two-dimensional maps were constructed with a patented MATLAB routine developed by Schlumberger Ltd.

5 Results

Accepted for publication in the AAPG Bulletin (07/31/2018).

5.1 NMR characterization of porosity-preserving microcrystalline quartz coatings in Fontainebleau sandstones

Marta Henriques Jácomo[a]; Ricardo Ivan Ferreira Trindade[a]; Marsha French[b]; Everton Lucas-Oliveira[c]; Elton Tadeu Montrazi[c]; Tito José Bonagamba[c].

[a]Instituto de Astronomia, Geofísica e Ciências Atmosféricas, Universidade de São Paulo, São Paulo, Brasil;

[b]Department of Geology and Geological Engineering, Colorado School of Mines, Golden, United States;

[c]Instituto de Física de São Carlos, Universidade de São Paulo, São Carlos, Brasil;

Acknowledgments

The authors acknowledge CNPq for Marta Jácomo and Everton Lucas-Oliveira scholarships, FAPESP 2016/06114-6, Colorado School of Mines for providing part of Fontainebleau samples collection, and Schlumberger for the LaPlace Inversion routines.

Abstract

The almost pure quartz-cemented Fontainebleau Formation (Paris Basin, France) sandstones are known to preserve their porosity due to microcrystalline quartz coatings. Here we use Nuclear Magnetic Resonance (NMR) techniques, petrography, scanning electron microscopy (SEM), porosity and permeability measurements, hysteresis and mercury injection capillary pressure (MICP) curves, to identify and analyze their porosity structure. NMR experiments include T_2 relaxation times distributions and T_2-Filtered T_2-T_2 Exchange, a technique that provides estimates on the diffusion coupling by comparing the evolution of families of pores in T_2 distributions at different exchange times. Samples were divided according to their texture, composition and abundance of microcrystalline quartz crystals, comprising Group 1 samples with very low amounts of coatings and Group 2 samples with entire grains coated by microquartz. Both groups show three (or four) peaks in NMR 2MHz T_2 distribution at ~1s (peak A), 10^{-1}s (peak B), and 10^{-2}s (peak C); Group 2 samples present a

slight shift to shorter T_2 times in comparison with other samples. The longest T_2 peak A is due to intergranular macropores while the shortest peak C is due to the microporosity associated with the microcrystalline quartz coating at the surface of the pores. Peak B is also due to microporosity associated with microcrystalline quartz, but with a different S/V (surface/volume) ratio, being likely related to flat shaped pores within the microcrystalline coating. T_2F-TREx indicates the proton exchange is higher between macropores and the pore-surface micropores (peak C) than between macropores and the internal flat-shaped micropores; no exchange between the two sets of micropores can be observed. Our results show the potential of NMR techniques in characterizing the microporosity in Fontainebleau sandstones, which is key for the mechanism of porosity preservation in these rocks.

5.1.1 **Introduction**

Porosity is an important physical property defining the quality of reservoirs since it affects fluid migration and storage. Porosity tends to be lost with increasing depth usually following a power law specific for each basin (e.g., Bloch, 1991; Ehrenberg et al., 2008). Nevertheless, some deeply buried sandstones partially preserve their porosities due to processes that limit compaction and cementation or promote the dissolution of minerals. The main mechanism of porosity preservation is related to detrital grains coating by either clay (e.g. Heald and Larese, 1974; Moraes and De Ros, 1990; Ajdukiewicz et al., 2010; Dowey et al., 2012) or microquartz (e.g. Vagle et al., 1994; Lima and De Ros, 2002; Worden et al., 2012; French and Worden, 2013), which inhibit the quartz cement overgrowths that syntaxially propagate from host grains and fills the pores (Cooper et al., 2000; McBride, 1989; Haddad et al., 2006).

Previous studies showed the importance of microcrystalline quartz coating on porosity preservation in Fontainebleau sandstones (Haddad et al., 2006; French and Worden, 2013). Detailed petrographic studies on samples from this unit demonstrate that siliceous cement covering the detrital grains results from rapid dissolution and precipitation processes of opal-A (amorphous silica), opal-CT (cristobalite-tridymite), chalcedony or cryptocrystalline and microcrystalline quartz. The microcrystalline quartz crystals inherit the crystallographic orientation of the length-fast chalcedony and grow parallel the surface of the detrital grains, therefore preventing growth into the pore and preserving the porosity (French and Worden, 2013). It is worth noting, however, the lack of studies about the micropore families, including those generated by microquartz crystals (Cooper et al., 2000; Al Saadi, 2017). In this context,

Nuclear Magnetic Resonance (NMR) is a suitable tool to identify and analyze the microporosity associated with the anomalous porosity preservation processes (Gallegos et al., 1988; Kenyon, 1989; Vincent et al., 2011; Mitchell et al., 2013). Yet, in spite of several studies on the Fontainebleau geology (e.g. Thiry et al., 1988, Thiry, 2005; Thiry and Maréchal, 2001), including NMR and petrophysical measurements (e.g., Fredrich et al., 1993; Hürlimann et al., 1994; Kieffer et al., 1999; Arns, 2004; Øren and Bakke, 2002; Wang et al., 2005; Fleury et al., 2001; Fleury, 2007; Talabi et al., 2009; Souza, 2012; Bernabé and Maineult, 2015; Livo, 2016; Al Saadi et al., 2017; Garing et al., 2017), a correlation between NMR and petrophysical data, with emphasis on the mechanisms of porosity preservation, is still lacking.

Here, we use the NMR Carr-Purcell-Meiboom-Gill (Meiboom and Gill, 1958) (CPMG) technique to measure the transversal relaxation time (T_2) and characterize the porous space of a set of Fontainebleau samples that contain microcrystalline quartz coatings. Other methods such as petrography (optical and electronic microscopy), porosity and permeability analysis, mercury injection capillary pressure curves and magnetic susceptibility data are used to improve the interpretation of the NMR results.

An important detail in the interpretation of the NMR CPMG data is related to the diffusion coupling discussed by Straley et al. (1995), Kenyon (1997), Grunewald and Knight (2011) and Keating and Knight (2012). In order to study this effect, we used the T_2-T_2 Exchange technique which allows observing fluid molecules migration among different pores (Washburn and Callaghan, 2006). Since T_2-T_2 Exchange experiments are very time consuming, a faster version of this experiment was used (T_2F-TREx) following the procedure of D'Eurydice et al. (2016). The T_2F-TREx is alternative T_2-T_2 Exchange NMR technique that compares the evolution of families of pores in T_2 distributions at different exchange times using a fix number of π pulses in the first CPMG. Hence, it acts as a short T2-filter allowing to estimate the diffusion coupling between the peaks or families of pores (D'Eurydice et al., 2016).

5.1.2 **Fontainebleau Formation, Paris Basin**

Early Oligocene Fontainebleau sandstones (24-34 Ma) are located in the central Paris Basin, south of Paris, France. They form a 50 to 80 m (or 160 to 260 in) thick unit composed of homogeneous, well sorted and almost pure quartz sandstones deposited in a shallow marine environment during a marine transgression period.

Three main facies are distinguished in this unit: (1) bottom greyish sandstones containing quartz, feldspar, glauconite, carbonates, pyrite and organic matter (Thiry et al., 2015, 2017); (2) bottom 'ochre or greenish sandstones' composed of quartz, smectite or illite, feldspar and glauconite, and (3) top 'white sandstones' composed exclusively of quartz, with no clay minerals present. The clay content decreases upwards. The formation of white and ochre (or greenish) sandstones is the product of alteration of greyish sandstones (Thiry and Maréchal, 2001).

The white sandstones are the best known facies in petrophysical studies due to its homogeneity in composition, grain size and good porosity-permeability correlation (Al Saadi et al., 2017). This unit was formed during glacial periods by contrasted shallow loose permeable sands and tightly silicified quartz lenses at the edges plateaus and valleys. Silica precipitated as its solubility decreased by cooling when the nourishing groundwaters came in contact with the cold and even frozen grounds near their outlet (Thiry et al., 2015; Thiry et al., 2017).

Two types of 'white sandstones' were described by Haddad et al (2006). *Sample 1* consists of homogeneous quartz sandstones, formed by subangular overgrowth cements, which have the same orientation of the host grain and commonly form angular facets. All silica cement present in this type is quartz. *Sample 2* consists of cemented quartz sandstones, formed by quartz host grains, which are coated by quartz overgrowth cement and microcrystalline quartz. The quartz overgrowth cement forms a concentric zonation layer, which contains fine bright and dark luminescent bands, while the microcrystalline quartz crystals have orientations varying from 6^0 to 28^0 relative to host quartz grains and overgrowth cement.

Quartz cementation in Fontainebleau occurred during maximum ground-water flow and can be classified into four main types: (1) homogeneous syntaxial overgrowth; (2) heterogeneous syntaxial overgrowth with isopachous bright and dark luminescent parallel bands; (3) amorphous or cryptocrystalline silica; (4) randomly oriented microcrystalline quartz (Thiry and Maréchal, 2001; Haddad et al., 2006; French and Worden, 2013). The various silica phases probably precipitated along the nourishing solution flow path in relation with variable silica saturation states and precipitation kinetics (Thiry et al., 2015a & b). Among them, amorphous silica and microcrystalline quartz preserve the porosity at deeper reservoirs, while quartz overgrowths are one of the main porosity-loss causes because they can completely occlude the pore space (Worden et al., 2012, French and Worden, 2013).

The microquartz coatings are formed subsequently to chalcedony and inherit the crystallographic *c*-axis orientation growing parallel to the surface of the detrital grains. The result is that microcrystalline quartz cement does not grow towards the pores to clog them, but rather grow parallel to the walls, preserving the porosity (Worden et al., 2012; French and Worden, 2013). Additionally, the microquartz crystals grow much smaller crystals than the quartz overgrowths would. Here, we consider microcrystalline quartz as being partially oriented 0.5-10 μm quartz crystals formed on the quartz host grain surface (e.g., Vagle et al. 1994).

5.1.3 NMR and previous result on Fontainebleau sandstones

NMR is a noninvasive technique applied in the characterization of porous materials. The amplitude of the NMR signal is proportional to the number of molecules bearing ^{1}H nuclei in the fluid and its time decay is characterized by the longitudinal and transverse relaxation times T_1 and T_2, respectively (Kenyon et al., 1995; Kenyon, 1997).

The three main mechanisms that govern the ^{1}H NMR relaxation in a fluid within a porous medium are: bulk relaxation **($T_{1,2B}$)**, which is related to magnetic dipolar couplings among proton nuclei, being mostly controlled by viscosity, fluid composition, temperature and pressure (Coates et al., 1999); diffusion relaxation **(T_{2D})**, which is controlled by the dynamic behavior of the fluid molecules bearing ^{1}H nuclei under a magnetic field gradient (Mitchell et al.,2010; Kenyon et al., 1995; Kenyon, 1997); and surface relaxation **($T_{1,2S}$),** which is connected with the grain mineralogy and surface-to-volume ratio (SVR) (Davies and Packer, 1990; Davies et al., 1990; Song, 2003).

The NMR relaxation times T_1 and T_2 can be expressed according to these different relaxation mechanisms as:

$$\frac{1}{T_1} = \frac{1}{T_{1B}} + \frac{1}{T_1 S} \text{ and } \frac{1}{T_2} = \frac{1}{T_{2B}} + \frac{1}{T_{2D}} + \frac{1}{T_{2s}} \quad (40)$$

Depending on the pore sizes and the magnetic properties of minerals, the bulk relaxation rate ($1/T_{1,2B}$) of water can be neglected, since it is dwarfed by the other relaxation mechanisms.

The observed T_2 can also be affected by diffusion relaxation due to internal magnetic field gradients (G). Considering the classic Carr-Purcell-Meiboom-Gill (CPMG) experiment

to obtain T_2 relaxation time distributions, T_{2D} will depend on the gradient field (G) and inter-echoes times as follows:

$$\frac{1}{T_{2D}} = \frac{D(\gamma G T_E)^2}{12} \tag{41}$$

where $1/T_{2D}$ is the relaxation rate due to molecular diffusion, D (cm^2/s or 0.39 in^2/s) is the molecular diffusion coefficient, γ (Hz/gauss) is the gyromagnetic ratio, G (gauss/cm or gauss/0.39in) is the magnetic field gradient, and T_E (s) is the inter-echo time used in the CPMG sequence measurements. Using short T_E values the diffusion contributions are reduced to very small levels and can be neglected (Kleinberg and Horsfield, 1990). Hence, in low field NMR experiments, where these conditions can be satisfied, the magnetization decay is predominantly due to the surface mechanism.

In a specific regime, defined as fast diffusion limit by Brownstein and Tarr (1979), all the magnetization in the entire pore decays at the same rate due to the surface mechanism, and the surface relaxation time is proportional to the surface to volume ratio (S/V):

$$\frac{1}{T_{1,2s}} = \rho_{1,2}\frac{S}{V} \tag{42}$$

where ρ_1 and ρ_2 are the pore surface magnetic relaxivities for T_{1s} and T_{2s}, respectively. The surface relaxivity (ρ) is a measure of the surface relaxation efficiency. It is related to the concentration of paramagnetic or magnetic impurities at the surface, as well as with the grain surface wettability.

Previous NMR relaxation studies in Fontainebleau sandstones (e.g. Fleury et al., 2007; Souza, 2012, Livo, 2016) showed T_2 distributions varying from 10^{-4} to 2 s, forming three to four log-normal peaks. Arns (2004) and Souza (2012) obtained pore size distributions ranging between 10 to 300 μm and 0.02 to 400 μm, respectively. The longest T_2 peak was associated to the larger and preserved intergranular pores (Fleury et al., 2007, Souza, 2012 and Livo, 2016), but the sources of smaller peaks found at shorter T_2 times was not discussed by these authors. Although the Fontainebleau sandstones have an almost pure composition, the variable cement amount (and thus S/V) have been interpreted by Fleury et al (2007) as the main cause of the variable values of surface relaxivity observed in different studies: 4.1 to 16.0 μm/s (Hürlimann et al., 1994); 11.7 to 24.7 μm/s (Øren and Bakke, 2002); 3.5 to 11.7 μm/s (Fleury et al., 2007); 6.0 to 12.8 μm/s (Souza, 2012). These variations have been also interpreted as a reason for the weak correlation between NMR pore sizes and the estimated permeability of Fontainebleau samples (Fleury et al., 2007; Livo, 2016).

In this study, the diffusion coupling was investigated using the T_2-T_2 Exchange technique. In this experiment, one can measure the T_2 distributions using CPMG pulse sequences during two different periods of time, separated by a storage time t_s. In this way, this experiment allows measuring the correlated T_2 distributions before and after t_s. This means that, if there is no migration of molecules (or if they migrate to similar pores) their respective T_2 values are the same before and after t_s. In its turn, if the molecules that have relaxed with the T_{2i} during the first CPMG migrate from the pore *i* to another pore *j* during the time t_s, these molecules should relax with a different T_{2j} during the second CPMG. This allows the estimation of the exchange, from an evaluation of the T_2 distributions of the second CPMG as a function of t_s.

5.1.4 **Samples and methods**

5.1.4.1 Samples

Eight samples of Fontainebleau Formation sandstones were studied. Two samples were collected in a previous study (French and Worden, 2013) at the Bonnevault quarry (Saint Pierre les Nemours, France), while the remaining six samples were purchased from Cydarex that provides outcrop samples from quarries from the same region. Samples acquired from Cydarex were bored as cylindrical samples 3.8 cm (or 1.5 in) in diameter and a length of 7 cm (or 2.75 in). These samples were split into two parts: the first one with length of 0.5 cm (or 0.20 in), was used for destructive analysis (Transmitted-light and scanning electron microscopy (SEM), Mercury Injection Capillary Pressure (MICP) and blue-epoxy resin impregnated thin polished sections), and the second, 3.8 cm (or 1.5 in) in length, was used for 2 and 85 MHz NMR analysis. Samples from the Bonnevault quarry were bored as cylindrical samples 1 cm (or 0.40 in) in diameter and length of 3.8 cm (or 1.5 in) and used only for the 20 MHz NMR analysis. These samples were previously studied for their petrography and porosity structure by French and Worden (2013).

5.1.4.2 Nuclear Magnetic Resonance

NMR measurements were performed using one LapNMR^{TM} Tecmag spectrometer operating at 20 and two Redstone^{TM} Tecmag spectrometers operating at 2 and 85 MHz. CPMG routines were performed with inter-echo spacing times of 200 μs, detecting 40,000 echoes. The number of scans for each experiment at 2, 20 and 85 MHz were 32, 16 and 8,

respectively. To convert the decay functions into a T_2 distribution was used the inverse Laplace transform (ILT) implemented in our NMR Group, using the curvature-smoothing regularization method (Borgia et al., 1998; Kenyon, 1997).

The T_2-Filtered T_2-T_2 Exchange (T_2F-TREx) experiment consists of measuring the T_2 distributions using CPMG pulse sequences during two different periods of time, separated by a storage time t_s. The first CPMG is used to filter the shorter relaxation times which are associated with the smaller pores. After this step, during the storage time, the molecules within the macro pores (longer T_2 relaxation times) can migrate to the others pores whose relaxation times were filtered. The second CPMG is used to measure the magnetization intensities of each pore after the time t_s. These intensities are associated with the storage time t_s and exchange rate k_{ij} between the pores. Therefore, the exchange is observed by the reappearance of the filtered times after the evolution of the time t_s (d'Eurydice, 2016).

The T_2F-TREx measurements were performed at 85 MHz with three and four filter times (D'Eurydice et al., 2016), defined by multiples of echo times for FB83 (3, 16, 200, 2500) and for 155 (3, 16, 300). The number of scans and echo time used were 8 and 250 μs, respectively. The storage time t_s was swept in 16 logarithmic steps.

To identify the intensity of each pore, we have fit each peak of the relaxation time by a log-normal function. In order to estimate the exchange rate, exchange curves were constructed for each pore which means that the magnetization intensities of each peak were analyzed according to time t_s. Afterwards, a numerical fitting was done for all the exchange curves simultaneously to obtain the exchange rates and the real relaxations times, according to the equation (Dortch et al., 2009):

$$M_{T_2-T_2}(t_1,t_s,t_2) = 2e^{L_2 t_2}\, e^{L_1 t_s}\, e^{L_2 t_1}\, M_0 \tag{43}$$

where: L_1 and L_2 are the -($R_{1,2}$ - K), and R_1 and R_2 are the diagonal matrices of the longitudinal and transverse relaxation rates, respectively. According to this equation, the evolution of the longitudinal and transversal magnetizations are not only due to relaxation rate, but also due to the exchange rate (*K)* between the pores. The times t_1, t_s and t_2 are the first CPMG evolution (filter time), the storage time (molecules migration) and the second CPMG (acquisition), respectively.

5.1.4.3 X-ray micro computed tomography (Micro-CT)

Three-dimensional images and estimation of pore-size distribution were provided through the micro-CT analysis. Measurements were performed using a Bruker SkyScan 1272 scanner (Belgium). The images were processed and analyzed using the Bruker micro-CT software (CTAn). The obtained images resolution was 2μm. The sample FB was obtained a 1.5 μm of resolution. The samples correspond to fragments from 0.5 to 1 cm^3 (or 0.03 to 0.06 in^3) in volume collected directly from the original samples.

5.1.4.4 Transmitted-light and scanning electron microscopy (SEM)

Optical microscopy observations of thin-sections were realized to identify the constituent minerals, describe the depositional and diagenetic processes, estimate qualitatively and quantitatively the composition and the textural framework, besides analyzing the porosity system. The quantitative analysis was done by modal analysis (point counting) with at least 300 points. SEM images were used to identify and characterize the coatings on detrital host grains and measure the size of the pores. Blue epoxy-impregnated thin-sections were examined with transmitted-light optical microscope. Scanning electron microscopy (SEM) observations were performed on rock chips cut from the same sample fragments used for thin-sections. We used the Zeiss Sigma Vacuum Field Emission SEM coupled to an Oxford Instruments EDX Penta Precision detector from IFSC (Instituto de Física de São Carlos, Brazil) to identify the composition of minerals and measure the size of micropores.

5.1.4.5 Porosity (ϕ) and permeability (k) measurements

We used thin-section point counting (300 points), Helium expansion 2500 PSI, water saturation, mercury injection capillary pressure and micro-CT methods to estimate rock porosity (Table 1). The permeability was determined using a Hassler cell (Table 1). A Core lab Helium Permeameter (model n. 3020-124 and series A7520) was used for measurements.

5.1.4.6 Mercury Injection Capillary Pressure

Mercury porosimetry is a widely used technique to characterize the pore space in diverse studies, including NMR. The advantage of this method is that mercury is a non-wetting fluid for most materials, so to penetrate into pores space it is necessary to apply a pressure, which is greater than the surface tension of the mercury — equivalent to 484.6

mN/m². As the pressure is incrementally increased, the mercury volume is injected into the sample and its volume can be measured (Anovitz & Cole, 2015). Mercury porosimetry was measured with a poreSizer 9320 Micromeritics Instruments Co. to obtain pore throat size distributions.

5.1.4.7 Magnetic susceptibility and hysteresis

Magnetic susceptibility is an important physical property in NMR studies since paramagnetic minerals can induce field inhomogeneity in the pore space, contributing to the faster $1/T_{1,2}$ relaxation rates (Kenyon, 1997). Magnetic susceptibility can be defined as a measure how much a material is likely to become magnetized. This property depends on the type and the concentration of magnetic minerals in the samples (Butler, 2004). In order to characterize the magnetic mineral in the sample and their type (paramagnetic or ferromagnetic), the hysteresis loops can be used through analyzing the induced magnetization behavior with increase applied magnetic field until 1T (Tesla) (Butler, 2004). H A MFK1-FA AGICO susceptometer operating at 976 Hz was used in this work. Magnetic hysteresis loops were obtained using a Princeton Measurements Corp. vibrating sample magnetometer, with a peak field of 1 T (Tesla) to define if the magnetic susceptibility was mainly carried by ferromagnetic or paramagnetic minerals.

5.1.5 **Results**

5.1.5.1 Petrography, electron microscopy and petrophysical data

Petrographic descriptions follow the classification of Haddad et al. (2006) for Fontainebleau white sandstones, which were divided into Groups 1 and 2 (equivalent to their Samples 1 and 2, respectively).

FB, FB10, FB25, FB83, FB217, FBL2B01 and FBL3B01 form Group 1 samples. They consist of fine and coarse sandstones composed of monocrystalline quartz grains (55 to 73%) and rocks fragments (1 to 4%). Authigenic silica phases include fibrous crystals of microcrystalline radial chalcedony (0 to 2%) grains, sub-angular and uniform syntaxial quartz overgrowth (10 to 21%) (Figure 26A-Figure 26B), acicular silica (0 to 7%) and chert (1 to 6%) (Figure 26A-Figure 26D). The microcrystalline quartz coatings, which are partially

oriented, can occur sporadically with incipient oriented overgrowth cements and do not cover the entire pore (Figure 26D).

The FB155 sample represents Group 2 (Figure 26E-Figure 26H). It is a fine grained quartz sandstone also composed of monocrystalline quartz grains (64%), rock fragments (3%), microcrystalline radial chalcedony fibers (1%), subangular and syntaxial quartz overgrowths (8%), acicular silica (6%) and chert (3%). The pore space of Group 2 samples (unlike Group 1) presents a set of alternating light and dark radial layers, which are deposited onto the host quartz grain and before the microcrystalline quartz coating (Figure 26E-Figure 26F). This structure appears also as bright and dark luminescence in the Fontainebleau samples studied by Haddad et al. (2006) and was initially interpreted as due to Fe^{+3} enrichment in the pore water. French and Worden (2013) showed through TEM (transmission electron microscopy), SEM, and optical thin section analysis that this zone comprises a light layer of amorphous silica (silanol Si-OH group or opaline silica) and the dark zone is formed by Si-OH opal, water and hydrocarbon compounds in fluid inclusions. SEM Sample 2 images show quartz host grains covered by amorphous silica (~1.5 μm) → chalcedony (~3.5 μm) → randomly oriented microquartz crystals (~5.0 μm) in sequence layers (Figure 26I and Figure 26J). Chalcedony forms ~100 nm particles and microcrystalline quartz crystals range from ~3 to ~10 μm (Figure 26G-Figure 26H).

The studied Fontainebleau sandstones are well sorted with unimodal grain and macropore size distributions in the range of 140 to 330 μm and from 12 to 75 μm, respectively. The FB25 sample has the smallest pore sizes, which vary from 7 to 30 μm. The pore throat size distributions obtained by MICP measurements show one dominant peak and other smaller peaks (Figure 27). FB10 and FB25 samples present the smallest throat pore sizes. In comparison to the other samples, among the small throat pore sizes the FB25 has the largest pore throat. Conversely, FBL2B01 and FBL3B01 samples have pore throat sizes slightly larger than the others (Figure 27). The MICP and Micro-CT distributions were used to estimate the surface magnetic relaxivity using the highest peak of MICP or micro-CT and the longest T_2 values observed at 2 and 20 MHz, which is expected to be correlated with the largest pore size, Equation 41. The distributions of T_2 relaxation times are shown overlapped in the Figure 27 (MICP) and 28 (micro-CT).

In both sets of samples, porosity is dominantly related to the intergranular pore space, which is sometimes filled with small amounts of acicular silica, varying in length from 10 to 50 μm (FB25, FBL2B01, FBL3B01 and FB155) and partially oriented microquartz crystals,

which vary from 600 nm to 3.0 μm in diameter. Mercury and micro-CT porosities vary from 5.6 to 17.9% and 5.5 to 20%, respectively. The permeability varies from 10 to 1,050 mD (Table 1). The samples showed a significant difference among the porosity data, mainly due to size and heterogeneity of the samples, besides the resolution of each method. While we used a ~1cm^3 (or 0.06 in^3) of samples in Micro-CT and MICP analysis, ~ 40cm^3 (or 2.4 in^3) were used for water saturated porosity and NMR measurements. Comparing the average of standard deviation between water method and the others for all samples, the Micro-CT method showed the minor value of 1.02%, while petroprahy and MICP showed 2.1 and 1.6%, respectively. These results showed that samples which are used in Micro-CT analysis are more similar than the others which are used in NMR and water porosity analysis. The similarities between NMR and Micro-CT distributions corroborate with this analysis. Among Group 1 samples, FBL2B01 and FBL3B01 are the most porous samples probably as a result of their depositional settings since samples with similar porosities contain different amounts of microcrystalline quartz and cements. The late formation of the amorphous silica layer or microcrystalline quartz during eodiagenesis favoring the development of quartz overgrowth cement, preserved only 5 to 15% of the porosity.

From the magnetic point of view, hysteresis analysis show that Group 1 is purely diamagnetic, while Group 2 has a small ferromagnetic contribution due to the presence of trace amounts of magnetite (Table 2), probably inherited magnetite grains included in the detrital quartz grains.

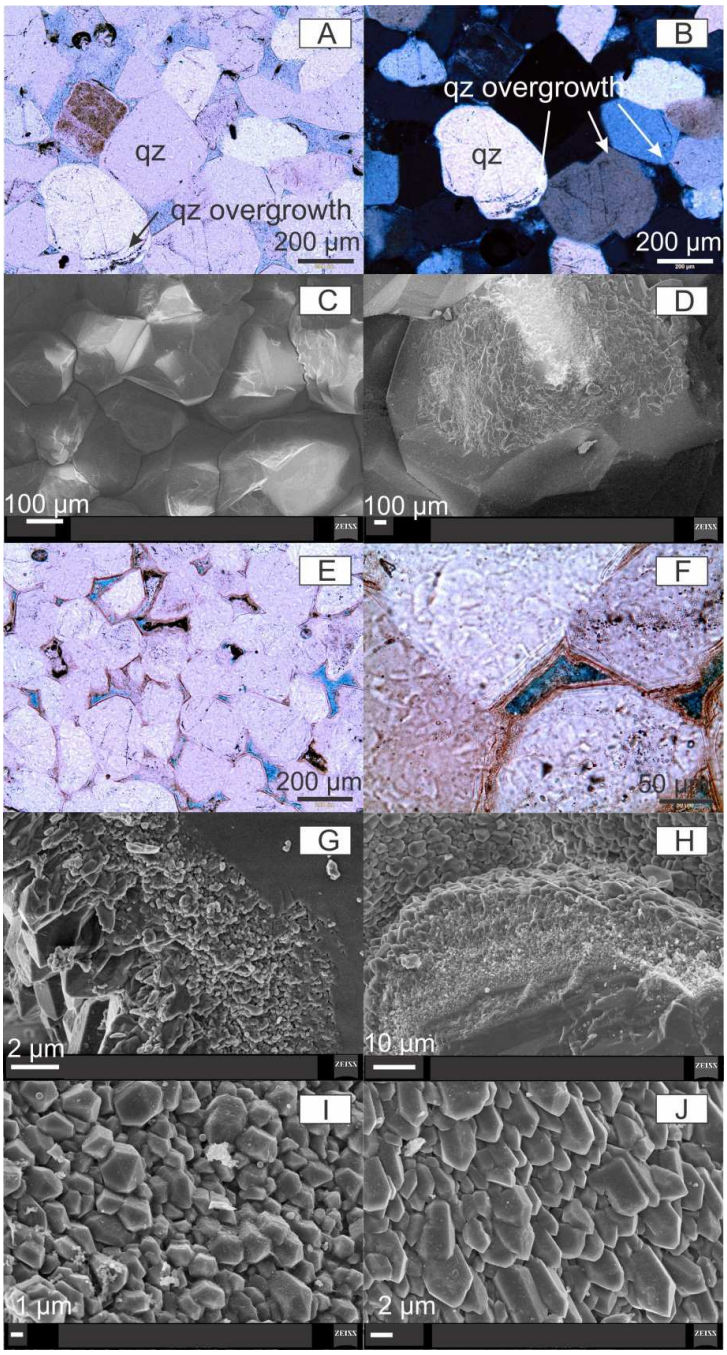

Figure 26 –A-D) Group 1 samples showing homogeneous well developed quartz (Qz) overgrowth cements. The partially oriented microcrystalline quartz coatings do not coat the entire pore. E-F) Group 2 microscopy optical images showing light and dark alternating zones; G-H) SEM images showing clearly the microquartz coatings covering the entire pore. It is observed the quartz host grains are coated by amorphous silica → chalcedony → randomly oriented microquartz crystals in sequence layers; I-J) SEM images showing the microporosity associated with microquartz crystals.

Table 2 – Table 1: Porosity data (ϕ), which were measured trough petrography, water, mercury and X-ray micro computed tomography (micro-CT) techniques, permeability (*k*), which was measured using helium gas, magnetic susceptibility (*Sus*) and magnetism of Fontainebleau samples. Dia is diamagnetic mineral and ferro is ferromagnetic mineral.

Sample	Group	ϕ (%) petrography	ϕ (%) water	ϕ (%) mercury	ϕ (%) micro-CT	k(mD) helium	Sus (10^{-6} SI)	Magnetism
FB	1	9.3	12.6	17.9	11.8	491	-6.93	-
FB10	1	6.0	4.5	5.6	4.9	10	-11.07	Dia.
FB25	1	2.7	5.0	5.8	7.5	25	-10.83	Dia.
FB83	1	4.3	8.0	5.9	5.2	60	-9.82	Dia.
FB217	1	9.3	8.6	8.4	8.6	217	-10.24	Dia.
FB L2B01	1	15.3	-	15.9	19.3	-	6.92	Dia. + Ferro
FB L3B01	1	12.3	19.0	12.9	20	-	17.60	Dia. + Ferro
FB155	2	5.6	8.2	8.9	5.6	155	-9.26	Dia. + Ferro

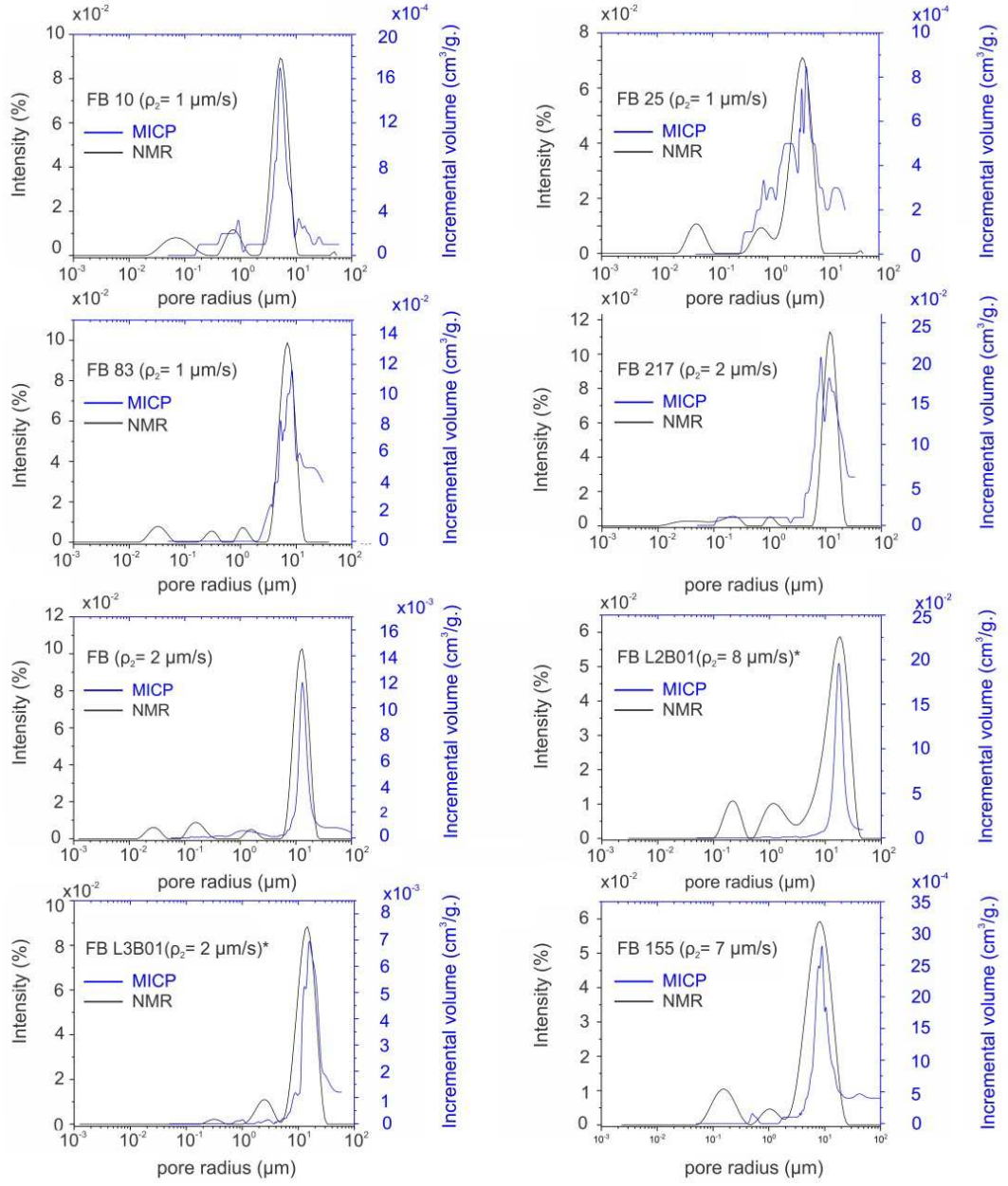

Figure 27 – Mercury Injection Capillary Pressure (MICP) and 2MHz Transverse relaxation times (T_2) or Nuclear Magnetic Resonance (NMR) distributions for Group 1 and 2 (FB155). For MICP, pore size is throat pore sizes. ρ_2 is the surface relaxivity *. The surface relaxivity t was calculated using the 20 MHz data.

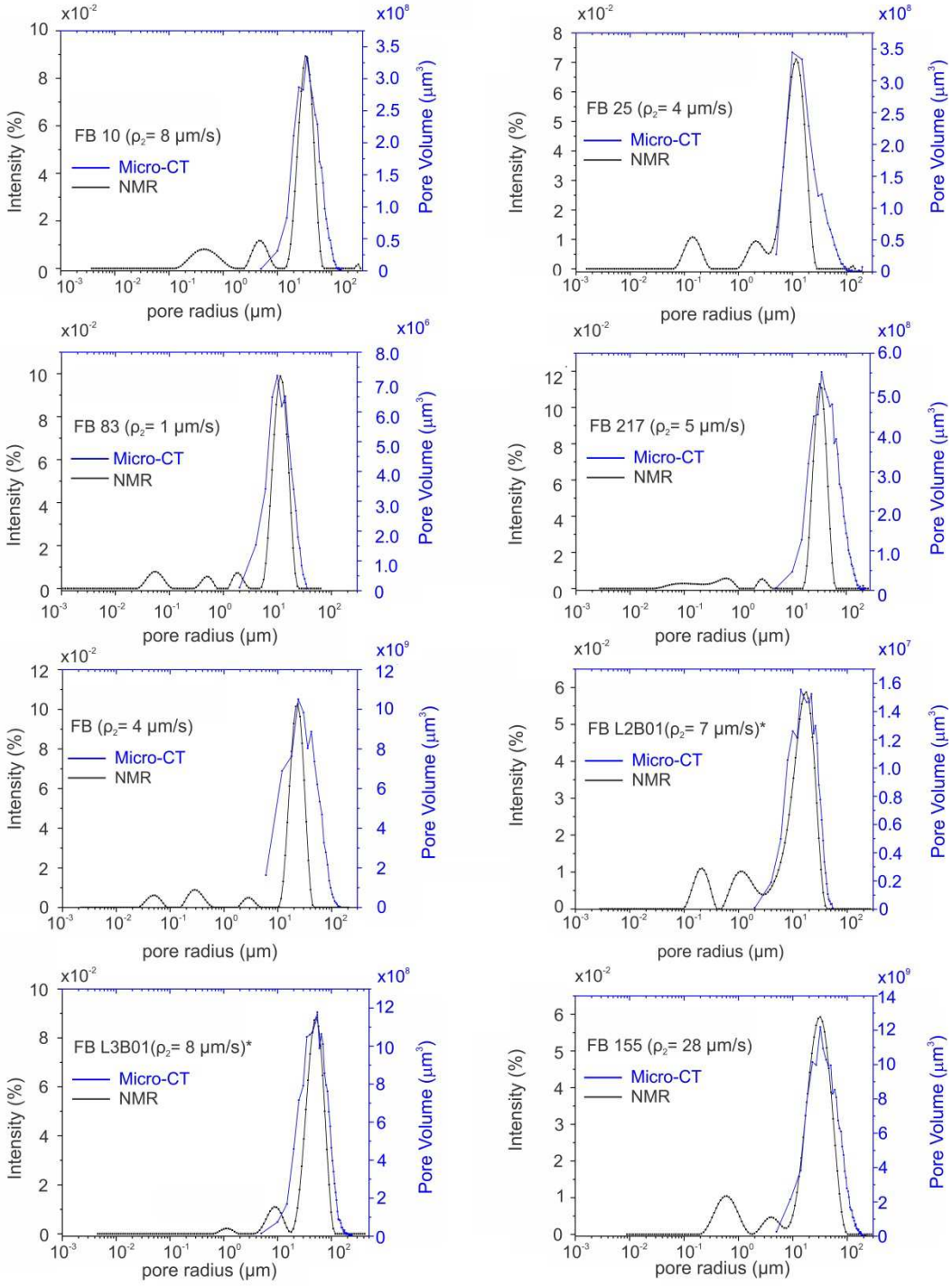

Figure 28 – X-ray micro computed tomography (Micro-CT) and 2MHz transverse relaxation times (T_2) or Nuclear Magnetic Resonance (NMR) distributions for Group 1 and 2 (FB155). ρ_2 is the surface relaxivity *. Surface relaxivity was calculated using the 20 MHz data.

The use of Fontainebleau sandstone for NMR studies and other petrophysical methods have many advantages, mainly due to its almost pure quartz composition (>99% quartz), relatively constant grain size and different levels of cementation (Fredrich et al., 1993; Al Saadi et al., 2017). Although with small non-homogeneous levels of cementation, the petrography of samples which contain microquartz coatings of Fontainebleau Formation is very similar of previously works (Haddad et al., 2006 and French and Worde, 2013). Due to this homogeneity, the studied samples are very well representative of microquartz coated sandstones.

5.1.5.2 Nuclear Magnetic Resonance

5.1.5.2.1 T_2 distributions

The T_2 distributions show three or four well-defined peaks in 2 and 20 MHz (Figure 29 and Table 3). The best log-normal fittings of 2 MHz T_2 distributions show that Group 1 shows the longest relaxation times, which vary from ~0.76 to ~1.7 s, and are significantly longer than that shown by Group 2 sample, which are about ~0.2 s. Among the samples from Group 1, FB25 presents the shortest T_2 values.

In general, 2 MHz T_2 distributions can be associated to pore size distributions, since the magnetic susceptibility effects are minor. Therefore, they can be correlated with MICP distributions, which correspond to the pore throat size distributions (Marschall et al., 1995; Straley et al., 1995; Kleinberg, 1996; Agut et al., 2000, Saidian and Prasad, 2015; Li et al., 2017). The Figure 29 shows a strong correlation between macro pores or pore throat sizes and a weak correlation for micro pores or pore throat sizes for almost all samples. FB10 and FB25 show better correlation for the entire distribution of pore and pore throat sizes, while FB25 and FB83 have the smallest pore and pore throat sizes. FBL2B01 and FBL3B01 have the highest porosities and pore throat sizes. Since they are measured at 20 MHz spectrometry, the real T_2 time in 2 MHz NMR distributions could be slightly longer than that shown in Figure 29.

In order to ensure that smaller T_2 peaks are not a result from noise or normal modes (Browstein and Tarr, 1979) and, therefore, have a geological meaning, an NMR analysis of a drying procedure was performed. First, the NMR signal of a totally saturated sample was obtained. Afterwards, the sample was continuously dried using a vacuum pressure of 700 mm

Hg in a laboratory stove at 30 ^{0}C for 0, 30 and 90 minutes steps. For each step, T_2 distributions were measured. Therefore, as the rock is continuously dry, it is expected that the water will go away first from the larger pores, highlighting the presence of the smaller ones and discarding the possibility of the smaller peaks in T_2 distributions being classified as normal modes which occurs when a pore presents more than one T_2 time, arising a new false peak in distributions. The Figure 30 shows the example of FB 155 drying procedure.

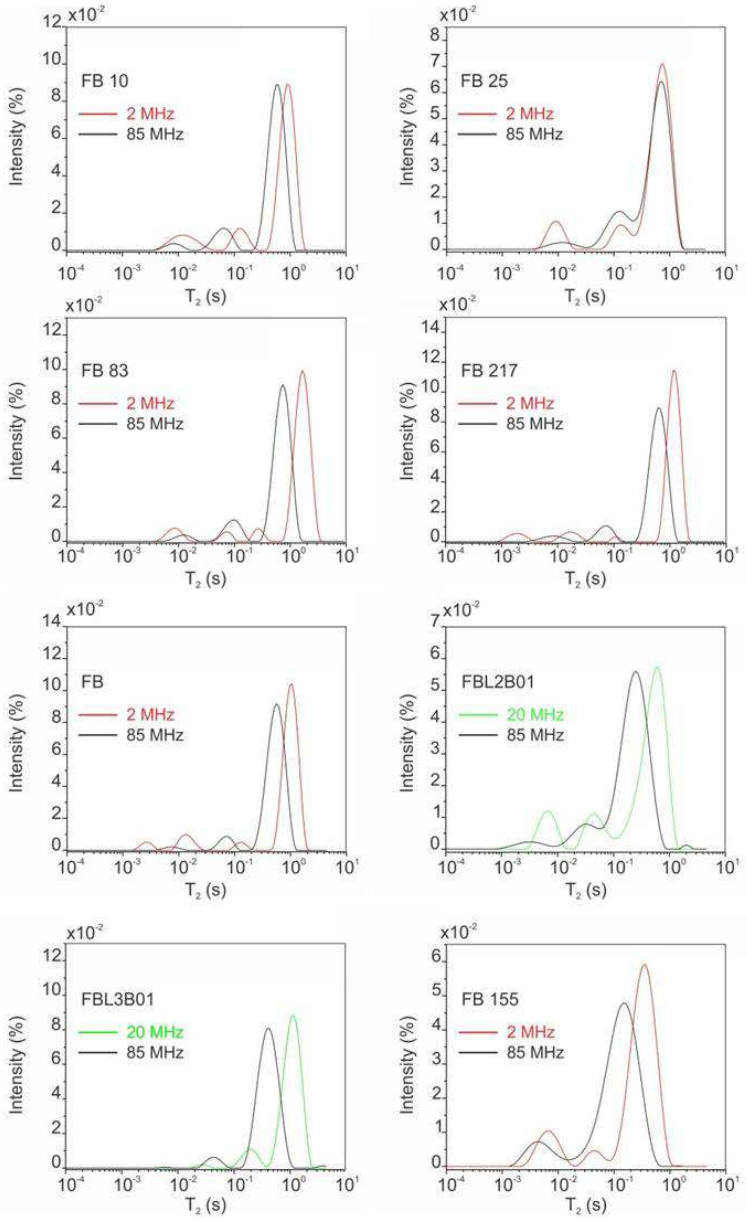

Figure 29 – Transverse relaxation times (T_2) distributions for Group 1 and Group 2 samples show 3 and 4 peaks at 2 MHz. In some cases, the shortest peak vanishes at 85 MHz (e.g. FB155). The peak dominant from Group 2 samples is shorter than the others. FBL2B01 and FBL3B01 samples were measured at 20 MHz due to equipment and sample size limit.

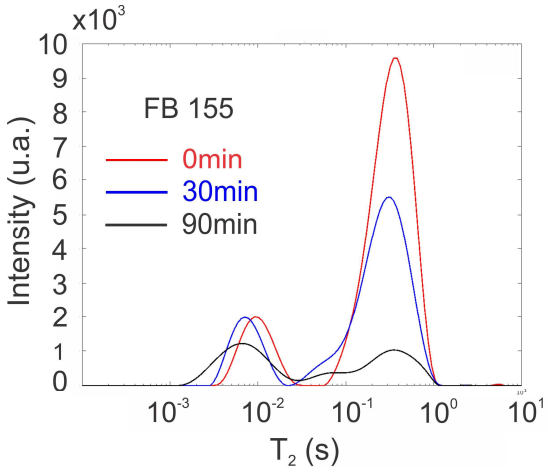

Figure 30 – Drying procedure of FB 155 sample, showing that two types of small pores (shorter transverserelaxation times peaks(T_2)) are becoming more evident as the drying time passes (0, 30 and 90 min.).

According to the model proposed by Browstein and Tarr (1979), all studied Fontainebleau sandstones are under the fast diffusion limit, since they satisfy the condition $\rho R/D_0 << 1$, where ρ is surface relaxivity, R is the estimated pore size and D_0 is the diffusion coefficient of water ($2300 \mu m^2/s$). Therefore, the peaks in T_2 distribution are not normal modes and may be correlated with different pore types. Under this condition, Equation 42 can be used to correlate pore sizes and T_2 relaxation times. Since MICP shows pore throat, not pore distributions, it presented a weak correlation between water saturated measurements of porosity and due to the weak correlation between peaks in MICP and NMR distributions, the Micro-CT data was preferred in surface relaxivities estimation (Figure 27 and 28). Using Micro-CT data, the estimated transverse surface relaxivity (ρ_2), which correlates T_2 with pore sizes, varies from ~1 to 8 μm/s for Group 1 and is ~28 μm/s for Group 2. The ratio between the surface relaxivity average of Micro-CT and MICP data is 2.7.

Internal magnetic field gradients may arise from magnetic susceptibility differences between the pore surface and the fluid filling the porosity under the presence magnetic fields (Kleinberg et al., 1994). Here, we qualitatively compared T_2 distributions at low (2 and 20 MHz) and high (85 MHz) magnetic fields (Figure 29 and Table 3). We observe a shortening of T_2 times under the higher magnetic field, corresponding to 85 MHz (2T) (Korb et al., 2003; Souza, 2012). FB25 and FB10 samples present small displacements between the curves, while FB, FB155, FB83 and FB217 show a visible shift. In addition, the samples that show 4 peaks in 2 MHz T_2 distribution have their smallest peak suppressed in 85 MHz (and Table 3).

Table 3 – NMR T_2 relaxation time (transverse relaxation time) values for each peak from 2 and 85 MHz using a log-normal fitting of curves and calculated surface relaxivity (ρ_2)using Mercury Injection Capillary Pressure (MICP) and micro computed tomography (Micro-CT); (1) is Group1; (2) is Group 2; * the experiment was done using 20 MHz).

Samples	T_2 (s) Peak 1		T_2 (s) Peak 2		T_2 (s) Peak 3		T_2 (s) Peak 4		$\rho_{2\ MICP}$ (μm/s)	$\rho_{2\ Micro-CT}$ (μm/s)
	2 MHz	85 MHz	2 MHz	85 MHz	2 MHz	85 MHz	2 MHz	85 MHz	2 MHz	2 MHz
FB (1)	1.07	0.59	0.13	0.07	0.01	0.01	0.01	-	2.27	4.20
FB10 (1)	0.93	0.59	0.13	0.07	0.01	0.01	-	-	1.27	8.06
FB25 (1)	0.76	0.74	0.14	0.14	0.01	0.01	-	-	1.24	3.72
FB83 (1)	1.74	0.76	0.28	0.10	0.07	0.01	0.01	-	0.48	0.76
FB217 (1)	1.26	0.67	0.11	0.07	0.02	0.01	0.01	-	1.77	4.77
FBL2B01 (1)*	0.63	0.25	0.32	0.03	0.05	0.01	0.01	-	7.62	7.22
FBL3B01 (1)*	1.20	0.42	0.20	0.05	0.03	0.01	0.01	-	2.24	8.23
FB155 (2)	0.36	0.17	0.05	0.06	0,01	0.01	-	-	6.78	27.92

5.1.5.2.2 T_2 – Filtered T_2-T_2 Exchange (T_2F-TREx)

When NMR experiments are run to measure T_1 and T_2 under exchange processes, the measured relaxation times can be modified due to the competition between relaxation and exchange if the exchange rate is equal or higher than the relaxation rates (Van Landeghem et al., 2010). Under these conditions, the measured relaxation times are called apparent ($\tilde{T}_{1,2}$) because the real ones ($T_{1,2}$) must be measured under the condition of no or negligible exchange. Notwithstanding, the real and apparent relaxation times and exchange rates (k_{ij}) can be estimated from the exchange curves.

For FB83 (Group 1) and FB155 (Group 2), at 85 MHz, the T_2 distributions show 3 peaks (A, B and C) and 2 peaks (A and C), respectively. The shortest T_2 peak (~10^{-3}s) is due to a probe background signal and was therefore disregarded of the results. Comparing T_2

distributions measured at 2 and 85 MHz, peaks A suffer bigger shifts to shorter T_2 values as compared to peaks B and C. For FB155, peak A is superposing peak B (Figure 29).

Figure 31 and Figure 32 show filtered echo times for samples FB83 and 155. For both samples the intensities of magnetization of all peaks in Filter 3 echoes decay due to the combined effect of relaxation and exchange, thus characterizing apparent longitudinal relaxation times. For FB83 it is possible to observe the suppression and recuperation of peak B in 2500 echoes filter (filter time of 625 ms). The same effect is evidenced in peak C for FB83 in 200 and 2500 echoes filter (filter times of 50 and 625 ms, respectively) and FB155 in 300 echoes filter (filter time of 75 ms). Also presented Figure 31 and Figure 32 are the integral amplitudes as a function of storage time $t_{s,}$ which can be defined as the time in which the molecular exchange between different pores occurs**.** These curves were obtained using log-normal fittings on T_2 distribution time. After, exchange rates and real and apparent relaxation times were obtained using a simultaneous fitting on integral amplitude curves and the results are shown in Table 4 (Montrazi et al., 2018).

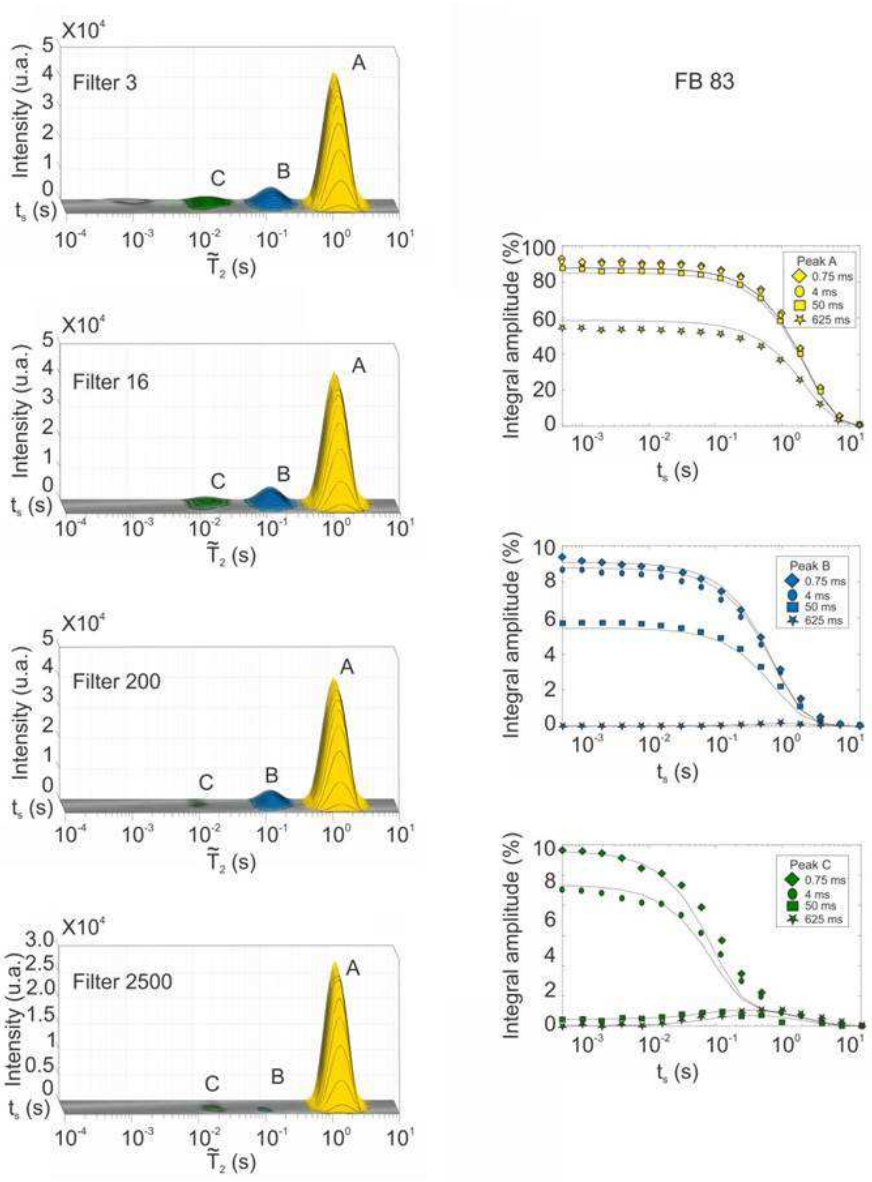

Figure 31– Apparent transverse relaxation times ($\tilde{T}_2$) distributions vs.storage time (t_s) (left) for different filters (3, 16, 200 and 2500 echoes) and Exchange curves (right) show t_s vs. integral amplitude of signal for three peaks or families of pores of FB83 sample in Group 1. The diamond, circle, square and star define 0.75, 4, 50 and 625 ms filter time, respectively.

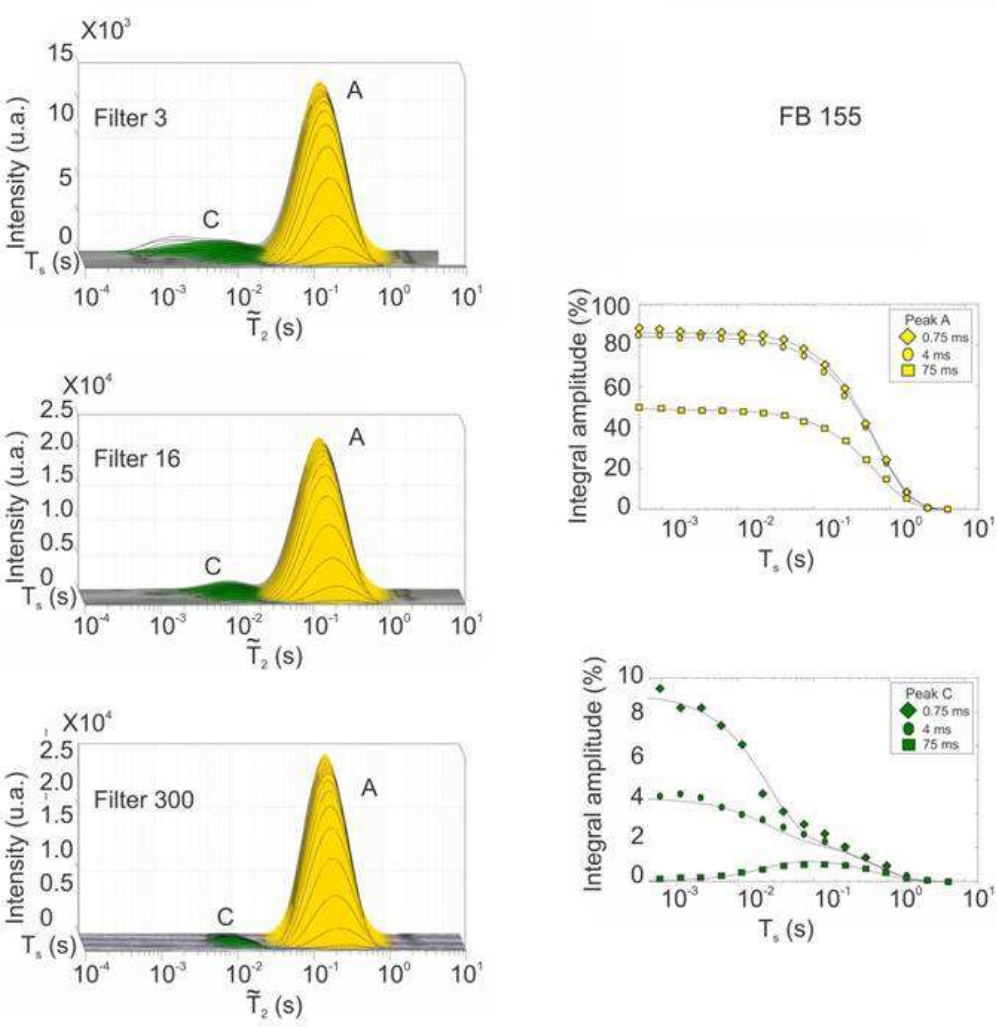

Figure 32 – Apparent transverse relaxation times ($\tilde{T}_2$) distributions vs.storage time (t_s)for different filters (3, 16 and 300 echoes) and Exchange curves (right) show t_s vs. integral amplitude of signal for two peaks or families of pores of FB155 sample (Group 2). The diamond, circle and square define 0.75, 4 and 75 ms filter time, respectively.

Table 4 – Longitudinal apparent ($\sim T_1$), transverseapparent ($\sim T_2$), real longitudinal (T1) and real transverse (T_2) (relaxation times as well as exchange rates (K) among the pores a, b and c, which are obtained from Exchange Curves (Figures 6 and 7).

FB83				FB155		
T_1^a (s)	T_1^b (s)	T_1^c (s)	κ_{ab}(s)	T_1^a (s)	T_1^c (s)	κ_{ac}(s)
2.7	0.79	0.11	0.007	2.1	0.037	1.1
$\sim T_1^a$ (s)	$\sim T_1^b$ (s)	$\sim T_1^c$ (s)	κ_{ac}(s)	$\sim T_1^a$ (s)	$\sim T_1^c$ (s)	-
2.4	0.75	0.09	0.046	0.74	0.029	
T_2^a (s)	T_2^b (s)	T_2^c (s)	κ_{bc}(s)	T_2^a (s)	T_2^c (s)	-
1.7	0.097	0.015	≈0	0.15	0.004	
$\sim T_2^a$ (s)	$\sim T_2^b$ (s)	$\sim T_2^c$ (s)	-	$\sim T_2^a$ (s)	$\sim T_2^c$ (s)	-
1.5	0.097	0.015		0.13	0.004	

5.1.6 **Discussion**

We studied a set of white Fontainebleau quartz sandstones samples composed of almost pure quartz. The samples were classified into two Groups, following the scheme of Haddad et al (2006). Group 1 consists of subangular and homogeneous overgrowth cemented sandstones. This cement grows syntaxially from the quartz host grain and form well developed angular facets. Unlike *Sample 1* of Haddad et al (2006), this group contains low amounts of microcrystalline quartz crystals, which partially cover the host detrital quartz grains. Group 2 illustrates all of the features described by Haddad et al (2006) for their *Sample 2* and also the samples described in French et al. (2013). It consists of cemented quartz sandstones, coated by concentric zonation layers of silica cements and partially oriented microcrystalline quartz crystals, coating host quartz grains or the overgrowth cements. SEM images show quartz host grains coated by amorphous silica or chalcedony → randomly microquartz crystals in a sequence of layers. Since these polymorphs become more crystalline, a microporosity associated with microquartz crystals can be formed (Lima and DeRos, 2002), which is indeed seen in SEM images (Figure 26). The quartz overgrowth

cements do not contain microporosity and the porosity associated with acicular silica is macro, varying from 10 to 50 μm.

NMR 2 MHz T_2 distributions showed three to four peaks as in previous studies (Fleury et al., 2007, Souza, 2012; Livo, 2016). In Group 1 samples the longest T_2 peak is about 1 s, the intermediate peak varies from 0.1 to 0.3 s and the shortest ones vary from 0.01 to 0.07 s. When the fourth peak is present, it varies from 0.002 to 0.009 s (Table 3). Group 2 samples present 0.35, 0.05 and 0.01 s for longest, intermediate and shortest T_2 times, respectively. Group 2 samples present shorter relaxation times than Group 1. This effect occurs generally due to presence of paramagnetic impurities (Kleiberg et al., 1994; Kenyon, 1997, Keating and Knight, 2007), but could also result from the presence of roughness in the pore surface or diffusion coupling (Straley et al., 1995; Kenyon, 1997).

Relaxation rates of confined fluids are proportional to the S/V ratio of pores (Equation 41), thus the longest T_2 times (peak A) can be related directly to the largest pores. Relaxivities related to the largest pores in the studied Fontainebleau samples range between ~1 and 8 μm/s, and reproduce the values previously obtained for this unit (Hürlimann et al., 1994, Øren and Bakke, 2002, Fleury et al., 2007, Souza, 2012). FB155 sample showed the highest relaxivity of 28 μm/s, which is close to the maximum value reported in the literature for Fontainebleau sandstones.

The peaks with lower relaxation times are the ones related to the microporosity and of direct interest here. They are less intense than the peak A and require more care during interpretation. Firstly, we estimated the water volume of each peak in T_2 distribution of completely saturated samples and then did some “NMR drying sample procedures”. Considering the system in fast diffusion regime, after drying the largest pore, the magnetization in the shorter T_2 times remains virtually unchanged. Through these experiments we can affirm that small NMR T_2 peaks are not normal modes and could be interpreted to be due to the micropores (Figure 30). From NMR *versus* MICP (Figure 27) analysis, all samples have small MICP peaks varying from 0.2 to ~1 μm. This result is reinforced by the petrography and SEM analysis. The pronounced ~3 μm MICP peaks in FB25 and FB155 are probably due the acicular silica which fills the pores. In NMR T_2 distributions, these ~3 μm MICP peaks are hidden by the largest T_2 peak. Finally, the best log-normal fittings of T_2 time distributions showed that among the small peaks, the peak with 10^{-2} s T_2 time has higher volumes than the others (except for FB83, in which the T_2 fourth peak is 7%, while the third is 4%) (28).

The interconnection between the different pore systems can be investigated through the diffusion coupling of the different NMR T_2 peaks. Kenyon (1997) defined two NMR models for diffusion coupling between clay flakes connecting channels and central macropores. The first occurs when there is no diffusion coupling between macro- and micropores. Therefore, two different peaks appear in the T_2 distribution, the shorter one being related to channels between chlorite flakes and the longer one being related to the macropores. The second model occurs when diffusion coupling is very efficient, so the magnetization of the whole pore is uniform and Equation 41 holds. Based on the conditions described by Brownstein and Tarr (1979), all studied Fontainebleau samples are under the fast diffusion mode and the second model is valid here. However, S/V of intergranular pores increases due to roughness of the pore surface, inducing a decrease in relaxation times distribution (Kenyon, 1997). Here, we used the T_2F-TREx to investigate the diffusion coupling between the three main NMR T_2 peaks identified in the Fontainebleau sandstones.

Table 4 shows the exchange rates obtained from T_2F-TREx experiments. For sample FB83 (Group 1), where all the peaks are distinguishable, one can observe exchange between peak A and peaks B and C, i.e. between the macroporosity and the microporosity. The stronger exchange between peaks A and C could be explained in terms of the coatings morphology, which interferes directly in the exchange rates, being more efficient for partially oriented microcrystalline quartz crystals at the surface of the macropore. Exchange between peaks B and C is not observed. For sample FB155 (Group 2), where peaks A and B are superposed, one can consider that the exchange occurs exclusively between peaks A and C. Notwithstanding, since the exchange between peaks A and C is higher than between peaks A and B, it is likely that peak B is associated to the most internal layers of the microquartz coating. If so, its longer T_2 values compared to peak C pores could be explained by a different pore shape or S/V ratio, more flattened pores providing longer T_2 times. Finally, the exchange rate (κ_{AC}) between macropore (A) and microquartz coating (C) for FB155 is orders of magnitude higher than that observed for FB83 (Table 4). This is related to the fact that, while for FB155 (Group 2) pore surfaces are completely covered by microquartz coating, for FB83 (Group 1) they are only partially covered. The macropores from Fontainebleau samples have similar compositions and sizes, however, the observed T_2 values for peak A, at the same magnetic field, are significantly different when comparing samples belonging to Groups 1 and 2 (FB83 and FB155, respectively). This difference could be explained by the concept of diffusion coupling (Kenyon, 1997), which is directly related with the real and apparent

relaxation times, as well as the exchange rates shown in Table 4. However, by comparing the apparent and real peak A T_2 values for both samples, it can be observed that they are very similar. This means that the diffusion coupling would not be responsible for the significant difference between peak A T_2 values observed in samples FB83 and FB155. In this case, this difference could be described by differences in terms of surface relaxivity or surface-to-volume ratio of the pores, which might be different due to the morphology of the microquartz coatings found for samples FB83 and FB155. However, by analyzing the apparent and real longitudinal relaxation times for sample FB155, one can observe that they are very different. This significant difference could be associated with diffusion coupling, because, in this particular case, the exchange rate is much bigger than the longitudinal relaxation rate, $k_{AC} >> 1/T_1^a$.

SEM images and optical microscopy can be used to test the previously proposed scenarios. NMR results are in agreement with microscopic observations, which showed a microporosity associated with the presence of microcrystalline quartz coatings, besides the acicular silica and intergranular framework. The longest T_2 peak of all samples value is due to primary intergranular porosity. Since the acicular silica porosity is macro and can be observed in SEM and petrographic images, we believe that it is included in the longest T_2 peak. In addition, in the T_2F-TREx results, pore sizes obtained through the calculated surface relaxivity allow us to relate the $\sim 10^{-2}$ peak in Group 1 T_2 time distribution to pores in the 300 nm to 1.4 μm range, suggesting that they are due to microporosity associated to microcrystalline quartz coatings. For $\sim 10^{-1}$ peak, the pore sizes would range from 2 to 5 μm. However, pores in this size range were not observed in SEM images. Therefore, we believe that shape of micropores which are associated with $\sim 10^{-1}$ peak is an important factor to determine the pore sizes. If these micropores were predominantly planar, their size would range from 0.43 to 1.26 μm, which is compatible with that observed in SEM images. The shape of micropores may be related to the coalesce and rotational dispersal of microcrystalline crystals. French and Worden (2013) defined a rotational distribution around 30^0 for Fontainebleau sandstones. Since this value is much lower than obtained by Worden et al (2012) for Heidelberg Formation - 180^0 - besides the exchange between peaks A and B is low, we believe that peak B is more associated with flattened pores, which are between semi-parallel c-axes of crystals. The higher exchange between peaks A and C permit to define C as been the microporosity associated with the space between multiples facets of diverse microqtz crystals, generating the diffusive coupling between the macropore and micropore (Figure 26I

and Figure 26J). The peak C could be the best indicative of amounts of microquartz since Group 2 contain the sample which the associated micropores (peak C) have the higher volume of water, while the space between the crystals along the c-axes (peak B) is the same for all samples. The shortest peak (10^{-3}s) in 2MHz T_2 distribution from samples which show four peaks (FB, FB83 and FB217) can be due to microporosity within the chalcedony layer. The calculated surface relaxivity showed a pore size range from 55 to 179 nm for this microporosity, as observed in SEM images (range from 80 to 140 nm).

In Fontainebleau sandstones, the pore surface is exclusively composed of silica, therefore differences in relaxivity are less likely to occur and the shape or roughness of the pores changing the S/V ratio is the most important factor controlling changes in T_2 time distributions.

5.1.7 **Conclusions**

The main conclusions of this work are:

- Two types of samples were defined, which are similar to those previously studied by Haddad et al (2006). Group 1 contains homogeneous cemented sandstones with quartz overgrowth containing small amounts of microcrystalline quartz crystals. Group 2 is an alternating light and dark zoned layered cemented sandstone with quartz host grains coated by amorphous silica → chalcedony → randomly oriented microquartz crystals sequence layer. The microquartz crystals are present on the entire pore surface.

- The primary cements are either syntaxial quartz overgrowths, which fills the pores and did not form microporosity, or partially oriented microcrystalline quartz crystals, which are known as an effective mechanism for porosity preservation.

- NMR techniques, such as T_2 time distribution (low and high field) and T_2F-TREx show the longest ~1 s peak in T_2 distributions is due to intergranular macropores and the ~10^{-2} s T_2 peak is due to microporosity associated with partially oriented microcrystalline quartz crystals. The intermediate peaks probably are also due to microporosity associated with partially oriented microcrystalline quartz crystals, but with different shape or S/V ratio (more planar). The 10^{-3} T_2 peak appears in some samples and can be interpreted as be due to microporosity within the chalcedony layer.

- NMR is as an excellent tool to characterize the porous space and the types of porosity, mainly those caused by microcrystalline quartz crystals, which are very important as a mechanism of porosity preservation.

Published in Petrophysics Journal (10/04/2018)

5.2 Nuclear magnetic resonance and pore coupling in clay-coated sandstones with anomalous porosity preservation (Água Grande Formation, Recôncavo Basin)

Marta H. Jácomo[a], Ricardo I. F. Trindade[a], Everton L. de Oliveira[b], Carlson de M. M. Leite[c], Elton Montrazzi[b], Mariane Andreeta[b], Tito J. Bonagamba[b]

[a] Instituto de Astronomia, Geofísica e Ciências Atmosféricas, Universidade de São Paulo, São Paulo, Brasil.

[b] Instituto de Física de São Carlos, Universidade de São Paulo, São Carlos, Brasil.

[c] PETROBRAS, Unidade de Operação-BA, Exploração

Abstract

Continuous chlorite coats are known to preserve the porosity in deeply buried sandstones by forming physical barriers to quartz early overgrowth. Sandstones from Água Grande Formation, Recôncavo Basin (Brazil) present anomalous porosity due to chlorite coating development and is suited to study the nuclear magnetic response to this effect. Samples from this unit were classified into three groups according to their texture, composition and abundance of chlorite coatings: Group 1 with low amounts of coating, Group 2 with high amounts of coating and a non-reservoir sample (Group 3). Group 1 samples show wide NMR T_2 distribution, while Group 2 samples present a bimodal T_2 Distribution. Non-reservoir Group 3 samples showed only a T_2 peak in much shorter T_2 times. To interpret the NMR results, transmitted-light optics, scanning electron microscopy, porosity (ϕ) and permeability (k) measurements, micro-CT, X-Ray diffraction, magnetic susceptibility and hysteresis were used. We conclude that the longest T_2 (>0.1 s) peak of reservoir samples (Groups 1 and 2) is due to intergranular macropores, the intermediate peak is due to feldspar or clay intraclasts dissolution and the shortest peak (~0.01 s) is due to the chlorite coating itself with minor contribution of secondary microporosity. The microporosity is predominant in the non-reservoir sample and relates to the clay bound water. The shift to shorter times of longer T_2 peaks in samples with higher contents of chlorite-bearing sandstones is likely related to diffusive coupling.

5.2.1 **Introduction**

Good porosity preservation is a key parameter in hydrocarbon reservoirs exploration, particularly in deep-seated ones (> 4 km). The loss of porosity with increasing depth is due to mechanical and chemical compaction, in addition to secondary cementation. However, clay coatings on detrital host grains when present as infiltrated clays in sandstones, even in small volumes, can inhibit quartz overgrowth thus preserving the porosity at depth (Moraes & De Ros, 1990; Anjos et al., 2003). Bloch et al. (2002) have defined the porosity preservation after burial as “anomalous porosity” condition.

Several studies have shown that early chlorite coatings on detrital grains are correlated with porosity preservation in deep reservoirs. However, the way in which it contributes to preservation is no consensus. While some authors affirm that chlorite grains inhibit the growth of quartz by separating the detrital grains surface to pore water, preventing the dissolution of the grains and avoiding nucleation (Ehrenberg, 1993), others suggest that inhibition of quartz overgrowth occurs due to limited epitaxial growth of inter-particle space by clay (Billault et al., 2003; Ajdukiewicz & Larese, 2012).

Anomalous porosities are observed only on sandstones containing eodiagenetic pre-compaction clays, which can be chloritized during mesodiagenetic processes. Late and neoformed mesogenetic clay coatings do not preserve the porosity, since sediments would have been submitted to the conditions necessary for cementation. An exception to this rule would be the formation of chlorite by the direct precipitation of interstitial fluids (Morad et al., 2000; Berger et al., 2009).

Chlorite is the most effective coating to produce anomalous porosity, but some studies have reported porosity preservation in fluvial reservoir rocks with chlorite which is a precursor of smectite (e.g. Luo et al. 2009; McKinley et al., 2003; Worden & Morad, 2003). Early diagenetic chlorite flakes form on the interface between the detrital grains and the intergranular porous space, while other clays such as smectite and illite grow perpendicular to the grain, forming a pore-bridging texture (Pitmann et al., 1992). Chlorite particles which are parallel or slightly oblique to the detrital surface tend to orient themselves progressively perpendicularly with the increase of the distance from the grain boundary due to geometric selection. During particle growth, the particles compete for available space such that some oriented crystals gain favorably more growth space than others. In this process, only high

tilting or perpendicular crystals continue to grow, as nothing can inhibit the growth of these crystals, since there is no competition among them (Ajdukiewicz & Larese, 2012).

Despite numerous works on the clay coating structure, mineral texture and the mechanisms leading to porosity preservation, a detailed study of the porosity distribution and macropore to micropore connection in these rocks is still lacking. Here we apply nuclear magnetic resonance (NMR) techniques that allow us to investigate the pore size distribution and the possible connection between pore families, together with other techniques for the pore space investigation such as transmitted-light optics, scanning electron microscopy and micro-computed tomography. We analyzed fluvial and eolian sandstones from Água Grande Formation (Recôncavo Basin), comprising samples with anomalous porosity due to the presence of clay coats and microquartz (Leite et al., 2014), and a non-reservoir sample. These eolian and fluvio-eolian sandstones are excellent oil-producing reservoirs in the Recôncavo Basin, even under deep burial conditions.

5.2.2 **Methods**

5.2.2.1 NMR

The pore space and the fluid, which fills the pores, control the NMR transverse (T_2) and longitudinal (T_1) relaxation processes by three mechanisms:

1) T_1 and T_2 intrinsic relaxations, which are mostly controlled by viscosity, fluid composition, temperature and pressure;

2) T_1 and T_2 surface relaxations, which are controlled by grain mineralogy and S/V ratio (size/ volume of pores); and

3) T_2 relaxation is affected by molecular diffusion, which is controlled by the behavior of the fluids when submitted to a magnetic field gradient; in this case, molecules diffuse into areas with distinct magnetic fields, making the precession rates different.

The relation that governs surface mechanisms in the fast-diffusion regime (Browstein & Tarr, 1979; Kenyon, 1997) is:

$$1/T_1=\rho_1(S/V) \text{ and } 1/T_2=\rho_2 (S/V) \quad (44)$$

where ρ_1 and ρ_2 are the pore surface relaxivities for T_1 and T_2, respectively; S/V is the surface/volume ratio. Surface relaxivity can be interpreted as a measurement of how much the

proton magnetization can relax when it encounters a pore surface and depends on the concentration of paramagnetic impurities and magnetic particles on it. At first approximation, the larger the pore size the smaller the S/V ratio, and the longer the relaxation time T_2.

The total magnetization is the sum of decay signals of each pore size:

$$M_z(t) = \sum_{i=1}^{n} M_i \exp\left(-\frac{t}{T_{2i}}\right) \tag{45}$$

where Mi is the equilibrium magnetization, T_{2i} is a constant decay time for the *ith* pore and Mz (t) is the total magnetization at time t.

The relaxation time rate due molecular diffusion in a gradient magnetic field is given by:

$$\frac{1}{T_{2Diffusion}} = \frac{D(\gamma G T_E)^2}{12} \tag{46}$$

where $1/T_{2\ \text{diffusion}}$ is the relaxation rate due the molecular diffusion, D ($cm^{2/}s$) is the molecular diffusion coefficient, γ is the gyromagnetic ratio, G is the magnetic field gradient (G/cm) and TE is the inter-echoes time used in the CPMG sequence measurements (Carr-Purcell-Meiboom-Gill).

T_2 and D- T_2 measurements were done on samples saturated with fresh water. The D-T_2 consists in a pulsed field gradient stimulated echo sequence PFG-STE and then CPMG.

The CPMG measurements were performed with echo times of 200 μs with 32 averages for each experiment. The 2D D-T_2 experiment was performed on the 2 MHz equipment, with time to the fixed stimulated echo in 6 ms, diffusion time of 40 ms, and time to the Hahn echo of 200 μs.

To convert the decay functions into a T_2 distribution we used the inverse Laplace transform (ILT) implemented in an in-house program developed in the NMR Group. Two-dimensional maps were constructed with a patented MATLAB routine developed by Schlumberger Ltd.

1H NMR measurements were performed using two Redstone Tecmag spectrometers, one operating at 2 MHz and another at 85 MHz, using a permanent (0.047 T) and an Oxford Instruments superconductor magnet (2 T), respectively, both from Instituto de Física de São Carlos, Universidade de São Paulo.

Complementary to the NMR study, we used transmitted-light optical and electron microscopy (SEM), gas porosimetry and permeametry, micro-CT (μCT), X-ray diffraction (XRD) and hysteresis measurements in order to identify and characterize the texture and reservoirs properties of samples. A detailed description of the experimental conditions and equipments used in these measurements is provided in the Appendix 1.

5.2.3 The Água Grande Formation, Recôncavo Basin

Recôncavo Basin is an aborted rift half graben rift situated in Northeastern Brazil, related to the South Atlantic Ocean opening during the Early Cretaceous (Milani & Davison, 1988). It is one of the most productive onshore areas in the country, with 72 mature fields presently in operation (ANP, 2016). Recôncavo basin reservoirs can be assembled into three main groups: 1) pre-rift aeolian fluvial sandstones of Sergi and Água Grande formations; 2) syn-rift deltaic sandstones of Ilhas Group; 3) syn-rift turbidite sandstones of Candeias and Maracangalha formations. The pre-rift system comprises the main reservoirs. The Candeias Formation is the hydrocarbon source for the petroleum system. It consists of rich organic carbon grayish lacustrine shales (average 4% TOC and kerogen type 1) intercalated with mudstones, siltstones, limestones and dolomites (Magnavita et al., 2012).

Reservoir rocks of Água Grande Formation are eolian-fluvial sequences. The fluvial unit is composed of fining upward cycles with conglomeratic sandstones at the base, grading from coarse to fine sandstone and capped by silty shales. The eolian unit is composed of well-sorted medium grained planar-bedded sandstones with depositional structures, which are typical laminations of depositional process (Cortez, 1996).

5.2.4 Results

5.2.4.1 Petrography, electronic microscopy and X- ray diffraction

We analyzed eight core plugs from Água Grande Formation sandstones, comprising seven plugs from the stratigraphic interval characterized by anomalous porosity by Leite et al. (2014) and one non reservoir sample. We divided the studied samples into three groups according to their sedimentary texture and composition (Table 5).

Group 1 comprises samples 7560, 7564 and 7570. They consist in moderately- to well-sorted subarkose or quartz sandstones, which are composed by quartz and feldspar as primary minerals. Diagenetic minerals are kaolinite and quartz overgrowth cements, which fill the

Table 5 – Petrophysical Parameters for Água Grande Formation samples.

Sample/Deep (m)	Texture original (Folk, 1968)	Depositional environment (geological description)	Group	Porosity (%) petrography	Porosity (%) density	Porosity (%) Helium gas	Permeability (mD) Helium gas	Magnetic Susceptibility (10^{-6} SI)	Petrofacies
7560 (1705,75m)	Quartz sandstone	Fluvial- deep burial diagenesis	1	15.00	10.08	10.40	9.87	19.27	Low permeability fluvial
7564 (1706,70m)	Subarkose	Fluvial –shallow to deep mesodiagene-sis	1	9.66	9.17	10.20	7.52	24.26	Low permeability fluvial
7570 (1707,85m)	Subarkose	Fluvial	1	9.00	8.44	10.80	44.70	8.05	High permeability fluvial
7536 (1699,65m)	Subarkose	Eolian- sand sheet with fluvial incursions or fluvial bars with eolian reworking	2	20.67	19.96	20.80	34.30	31.10	High pemeability Eolian
7545 (1701,95m)	Subarkose	Fluvial-eolian– shallow to deep mesodiagene-sis	2	19.67	15.27	17.30	4.14	29.88	Low permeability Fluvio-eolian
7549 (1702,80m)	Quartz sandstone	Fluvial- deep burial diagenesis	2	23.33	16.75	18.00	8.40	45.92	Low permeability fluvial
7552 (1703,50m)	Subarkose	Fluvial- deep burial diagenesis	2	18.00	17.00	17.70	4.69	31.07	Low permeability fluvial
7562 (1706,10m)	Mud sandstone (textural)	Fluvial – deep burial diagenesis (deep mesodiagene-sis)	3	0.00	2.77	1.40	0.00	116.67	Non-reservoir

pores. Dissolution of feldspar and clay intraclasts contributes a significant portion of porosity, varying from 1.3% to 5.0% (see Appendix 2).

Group 2 comprises samples 7536, 7545, 7549, 7552. They are characterized by moderately- to well-sorted subarkoses or quartz sandstones with parallel lamination. While quartz and feldspar are primary minerals, diagenetic minerals are dickite, anatase, quartz overgrowth, dolomite, chalcedony and albite (see appendix 2). Filling-pore minerals as dickite and anatase are the main cause of porosity-loss in these petrofacies. Similar to Group 1 samples, feldspar and the clay intraclasts were partially dissolved and develop secondary microporosity, corresponding to 2.0% to 4.7% of porosity volume. Intragranular diameter pores vary from 10 to 30 μm.

All reservoir samples have some content of clay coating on the host grains (Figure 33). X-ray diffraction (XRD) was used to identify the types of clays. As the amount of clay coats from Group 1 is below the detection limit, Figure 34 shows XRD results only from Group 2. Chlorite coat is evident by the ~14 Å peak in natural conditions (Line 1) and 15 Å peak in ethylene glycol (Line 2). It does not show the expansion from 16.65-17.15 Å under ethylene glycol solution, which is typical of smectite (Beaufort et al., 1997; Srodon, 1980). Kaolinite is present in all samples (Groups 1 and 2).

Authigenic chlorite occurs as pore-lining crystals, whose flakes are 5-10 μm across with thickness of ~0.1 μm and sometimes behave like pore-bridging clay, reducing the throats of pores and consequently the permeability (Figure 33E-Figure 33H). The eolian 7536 sample of Group 2 presents much less developed perpendicular flakes than the other samples (Figure 33E and Figure 33H). Group 1 presents less coating than Group 2 samples. When chlorite coatings are poor, discontinuous or absent, overgrowth of quartz cement occurs and part of the porosity is lost (Figure 33B and Figure 33I). Figure 33H shows that when the quartz overgrowth is perpendicular to the host grain (outgrowth), chlorite does not prevent the quartz overgrowth as proposed by Ajdukiewicz & Larese (2012).

To estimate the chlorite amounts, the SEM composition maps were combined into a color image (Figure 35). Typically, Group 1 samples show less chlorite content in comparison to Group 2 samples (Figure 35), with the percent of iron on grain surfaces between 5-31% in the former and between 39-60% in the later. The only exception is sample 7560, which is part of Group 1 but presents 50% of Fe covering the host grains.

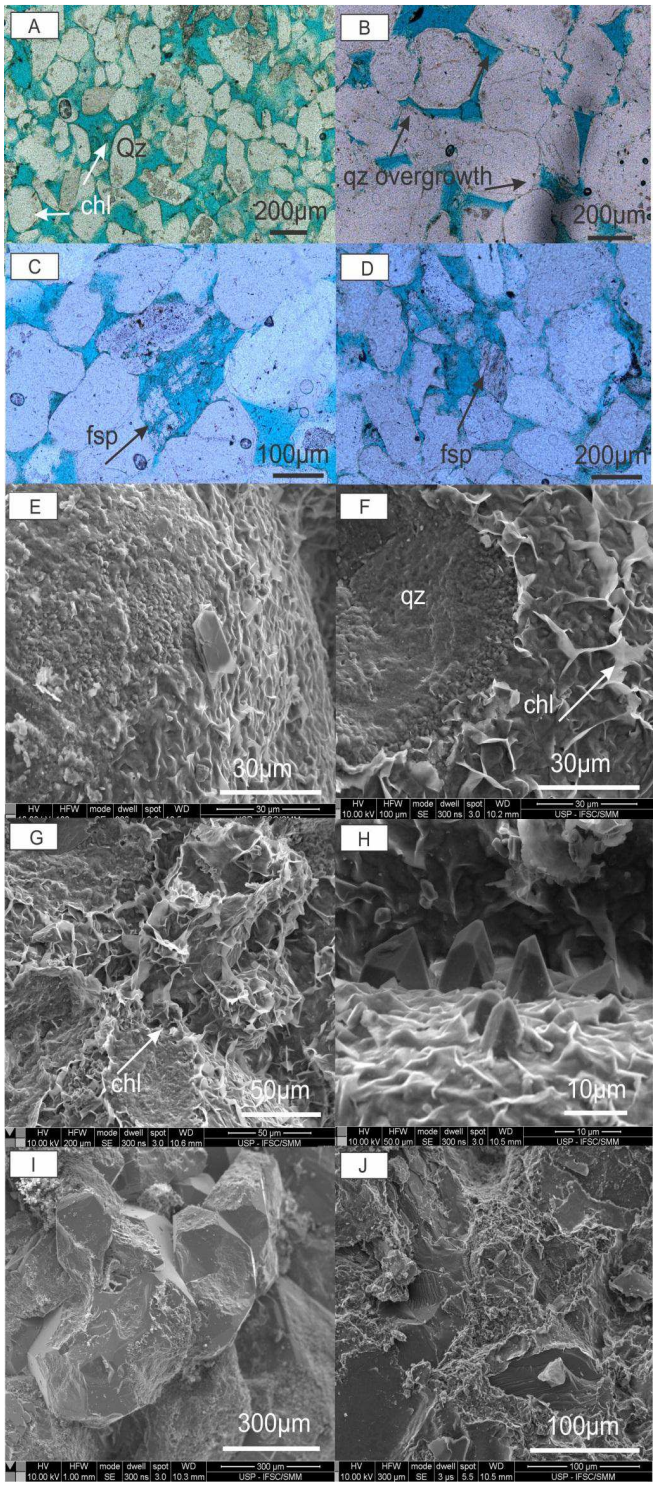

Figure 33 – Optical and scanning electron microscope images showing chlorite (chl) coating over quartz (qz) grains. Optical microscope images show the higher amount of coating in Group 2 samples (A) than in Group 1 samples (B). Group 1 samples develop quartz overgrowth (B). (C-D) show some examples of feldspar (fsp) dissolution generating secondary porosity in samples from both Groups. SEM images of chlorite coats with honeycomb morphology forming pore lining clays (E,F,H), sometimes with morphology similar to corrensite (chlorite-smectite) developing pore bridging (G). 7570 sample in (I) shows almost null chlorite coats (I). The non-reservoir 7562 sample (J) is very cemented sample and present very low porosityand almost null permeability.

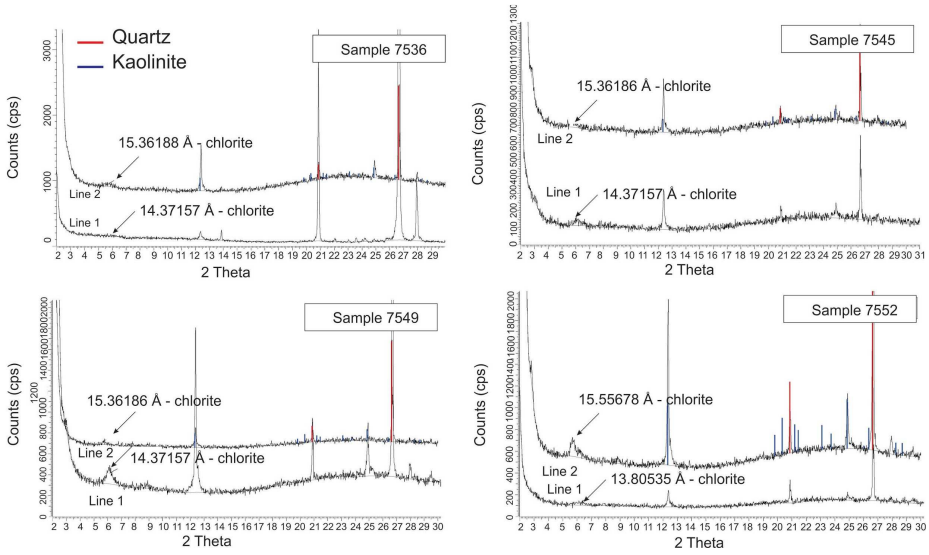

Figure 34 – XRD spectrum of Group 2 reservoir samples showing chlorite, kaolinite and quartz peaks.

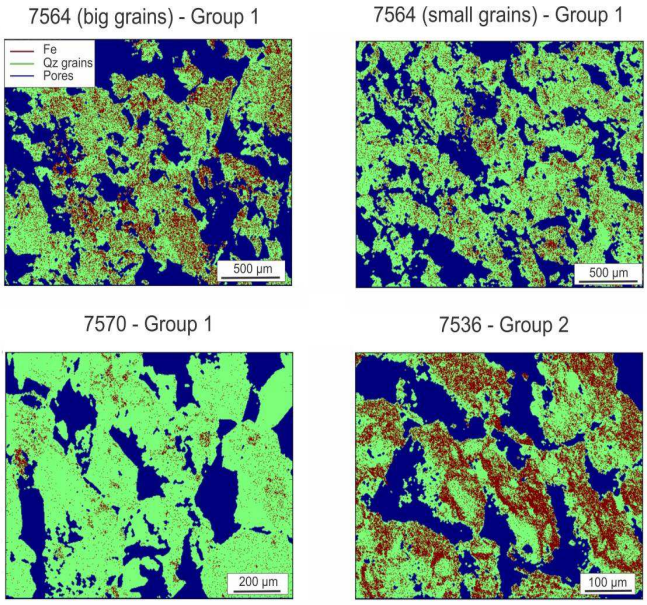

Figure 35– SEM compositional maps showing low Fe content on quartz host grains of Group 1 samples and higher Fe content in Group 2 samples. Sample 7570 is also characterized by the lowest values of magnetic susceptibility.

Group 3 is the non-reservoir sample. It consists of fine and moderately sorted mud sandstone (25% mud) with long or concave-convex contacts, attesting to significant pressure dissolution and the porosity loss (Table 5). This facies is composed by primary quartz and feldspar. Diagenetic minerals include dickite, illite/smectite, chlorite, anatase and pyrite (see

Appendix 2). SEM images (Figure 33J) and thin sections do not show any chlorite or chalcedony/microcrystalline coatings.

5.2.4.2 Porosity (ϕ), permeability (k) and pore size distribution

Porosity estimations with He porosimetry for Group 1 samples vary from 10.2% to 10.8%. These results agree with those obtained by other methods, including thin-section point counting and density measurements (Table 5). Permeability for the same samples is within 7.52 mD and 9.87 mD for low permeability samples (7560, 7564) and 44.7 mD for the high permeability sample (7570) (Table 5). Group 2 contains chlorite and preserves a good porosity varying from 17.7 to 20.8% (He porosimetry). The permeability in this group of samples varies from 4.13 mD to 8.40 mD for fluvial samples, and is 34 mD for the eolian sample. The non-reservoir Group 3 sample is strongly cemented and presents very low porosity (1.4%) and no permeability.

Pore size distribution was estimated through μCT. Pore sizes vary from 32.67 μm to 36.35 μm in Group 1, and from 24.68 μm to 33.98 μm in Group 2, but both groups have similar modes (volume *versus* pore size) of ~20 μm regarless of grain size (Figure 36A). Pore size distributions were modeled using a digital rock reconstruct of μCT images and a pore throat network technique developed by Andreeta (2017) (Figure 36B). According to the model, Group 2 pore sizes present unimodal size distributions (Figure 36C) even when grains have a bimodal texture, confirming the μCT data.

5.2.4.3 Magnetic susceptibility and hysteresis

Group 1 samples show lower magnetic susceptibility than Group 2 samples. Susceptibility values vary from 8.05×10^{-6} SI to 24.26×10^{-6} SI in Group 1 and from 29.88×10^{-6} SI to 45.92×10^{-6} SI in Group 2. For most samples from both groups, hysteresis data show that the paramagnetic signal of clays is dominant (Figure 37A-Figure 37E).

A very small amount of low-coercivity magnetic minerals can be detected in the hysteresis cycle, probably due to trace amounts of magnetite (Figure 37A-Figure 37E). For sample 7570, which shows the smallest content of clay coating, the magnetic susceptibility at higher field is negative, and directly related to the quartz matrix (Figure 37F). Since the magnetic susceptibility, particularly at fields above 0.1 T, is almost completely controlled by

the paramagnetic clays, it can also be used as an indicator of the amount of chlorite coating in these samples. Group 3 sample shows the highest magnetic susceptibility of 116.67x10^{-6} SI.

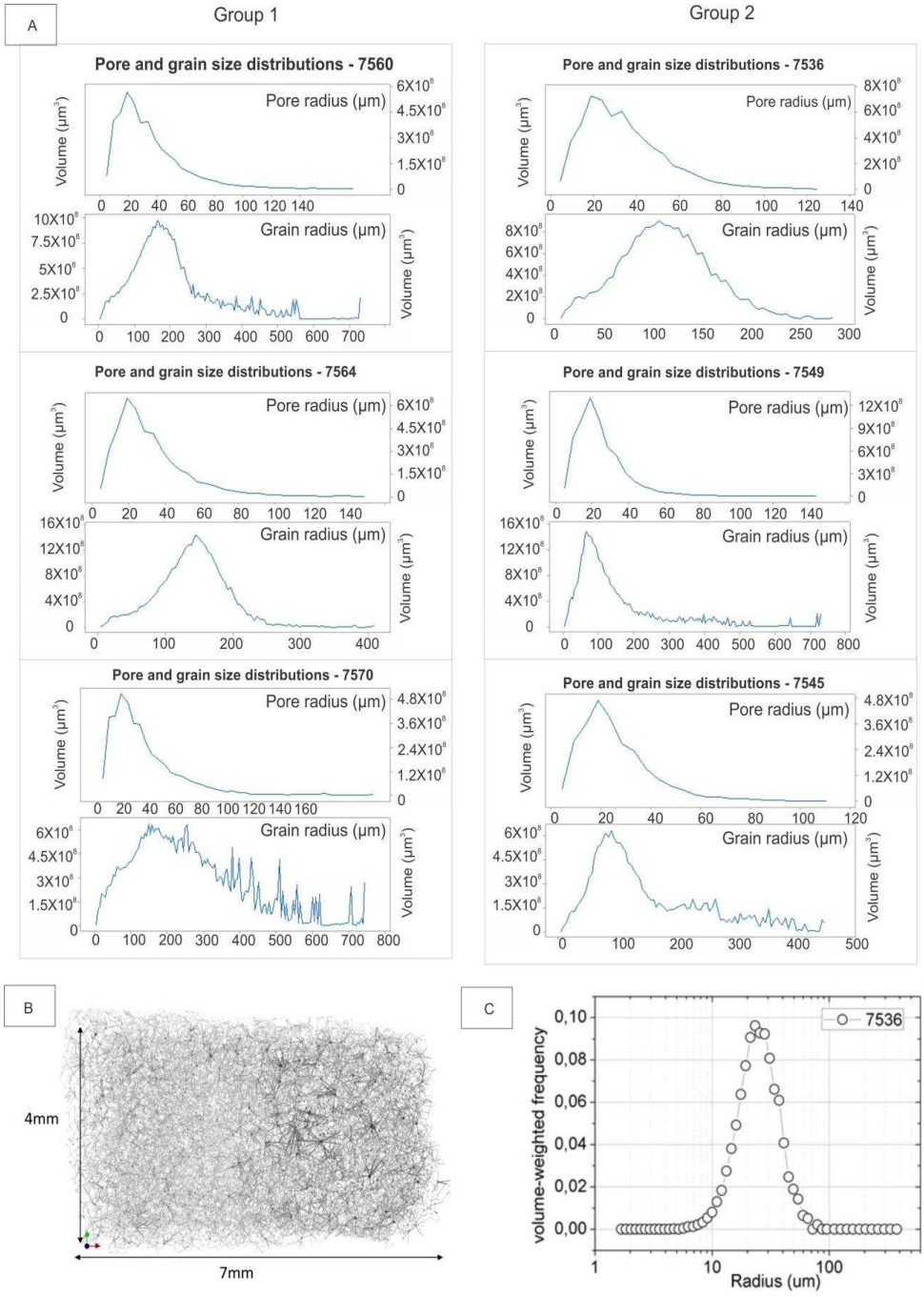

Figure 36 – µCT images showing pore and grain distributions of Group 1 and Group 2 reservoir samples (A). In (B) a network visualization method for the 7536 sample with a evident lamination and in (C) a histogram of pore volume distribution.

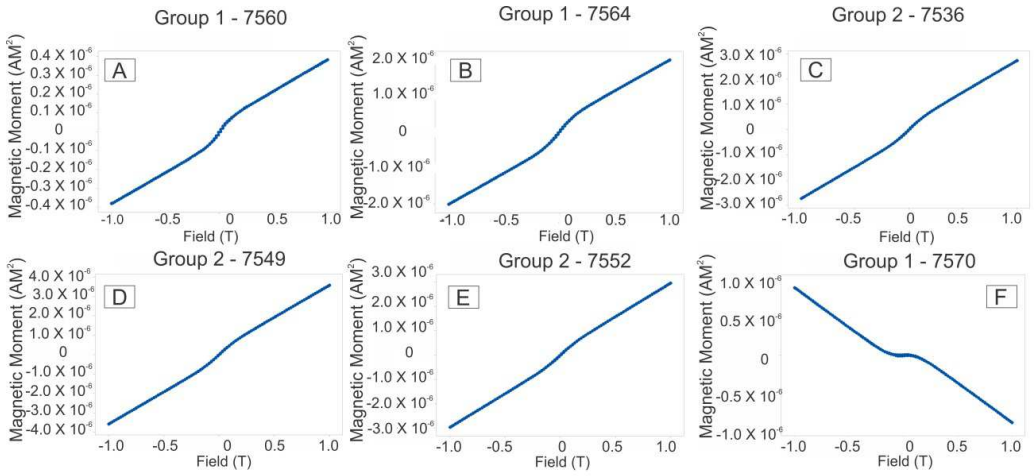

Figure 37 – Curves of magnetic field (T) against magnetic moment (A.m) – hysteresis loop - for reservoir samples showing a dominant paramagnetic behavior for Groups 1 and 2, except for sample 7570, which is dominantly diamagnetic at higher fields. All samples show some content of low-coercive ferromagnetic particles, probably magnetite, as indicated by the magnetic hysteresis.

5.2.4.4 Nuclear magnetic resonance

Figure 38 shows T_2 relaxation time distributions for all studied samples. Group 1 samples show a wide distribution of T_2 values. The best log-gaussian fittings to T_2 distribution shows three defined sites: the shortest varies from 0.025 s to 0.01 s, the intermediate from 0.02 s to 0.1 s and the longest from 0.1 s to 0.44 s. In contrast, Group 2 samples present two well defined modes in the T_2 time distribution whose peaks vary from 0.016 s to 0.018 s for the shortest times and from 0.19 s to 0.209 s for the longest times. In the non-reservoir sample (Group 3), the micropores with T_2 time mode at 0.001 s predominates. Very low intensity peaks also occur at 0.02 s and 0.576 s.

It can be observed that Group 1 longest T_2 times are higher than those of Group 2. To verify if this effect is related to internal magnetic field gradients around the pore surfaces, we can compare measurements performed for samples of both Groups using low (2 MHz) and high (85 MHz) magnetic field (Figure 39). All reservoir samples show an increase of the shortest amplitudes in 85 MHz. Group 1 samples present fewer displacements between the two curves than Group 2, for which longer T_2 peaks present displacements to shorter times of a factor of 10 on 85MHz high field. This shift generally is due to internal gradients in high magnetic field, caused mainly by the differences of magnetic susceptibility between the pore surface and fluid. In this turn, the internal gradient is negligible in low external magnetic field, such as 2MHz (Song et al., 2003). The 85MHZ internal gradients are estimated in order

of 10^2 to 10^3 (Gauss/cm) for large pores (longest T_2) and 10^3 (Gauss/cm) for smallest pores, as it expected (Song et al., 2003). These differences are due the differences in proton travelling around shorter average distances in small pores when compared to those in larger pores, where there are particles near and far from pores surface. Besides this, NMR experiments increasing the time between πrf pulses from 200 μs to 500 μs in low magnetic field (2MHz) were also performed and do not show significant displacements of T_2 curves, which evidences the minimization of the internal gradient effect using 200 μs as echo time. Group 3 sample also shows a small displacement between 2 MHz and 85 MHz curves due to the very low water content that fills its pores (Figure 39D).

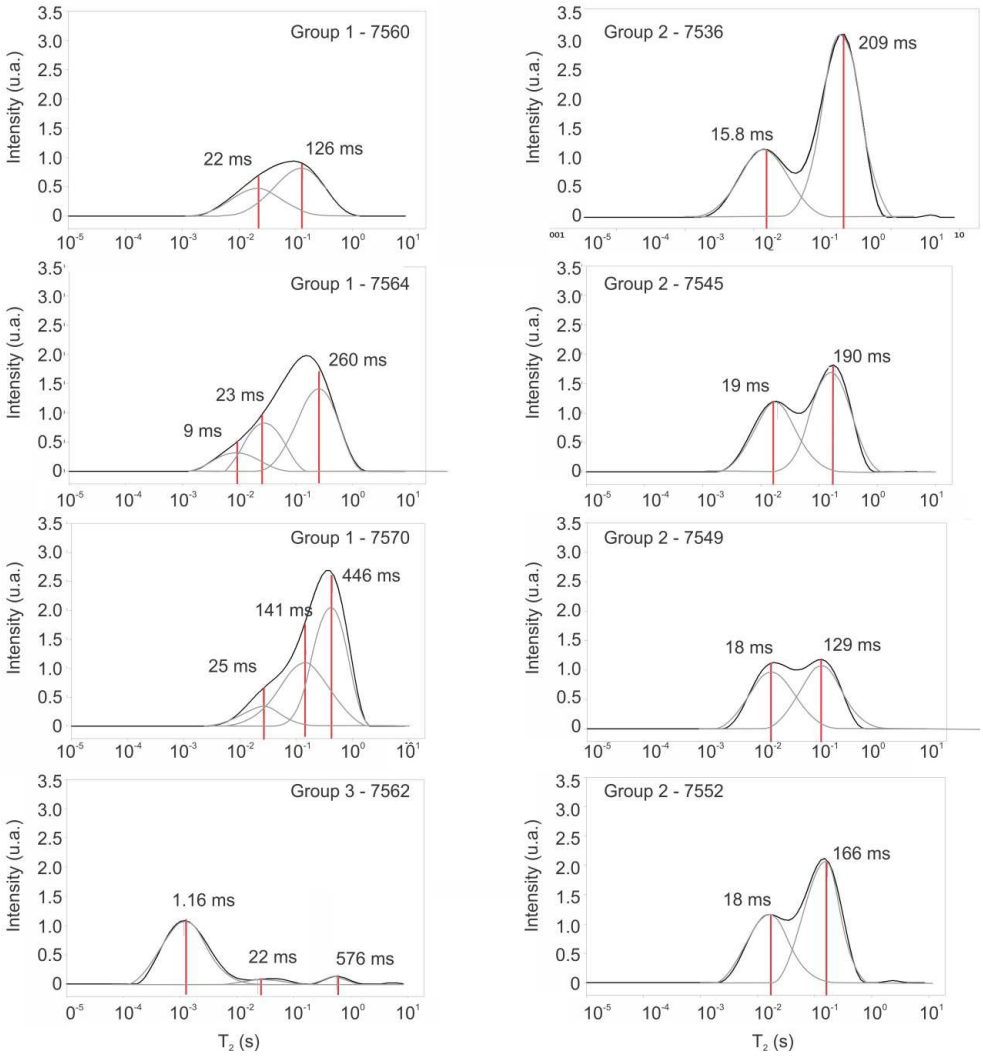

Figure 38 – T_2 distributions for Groups 1, 2 and 3. Group 1 samples (left column, except 7562) shows a wide NMR T_2 distribution. Group 2 samples (right column) show bimodal distributions. The non-reservoir sample (Group 3 –left column and last line) shows an intense peak in shorter times.

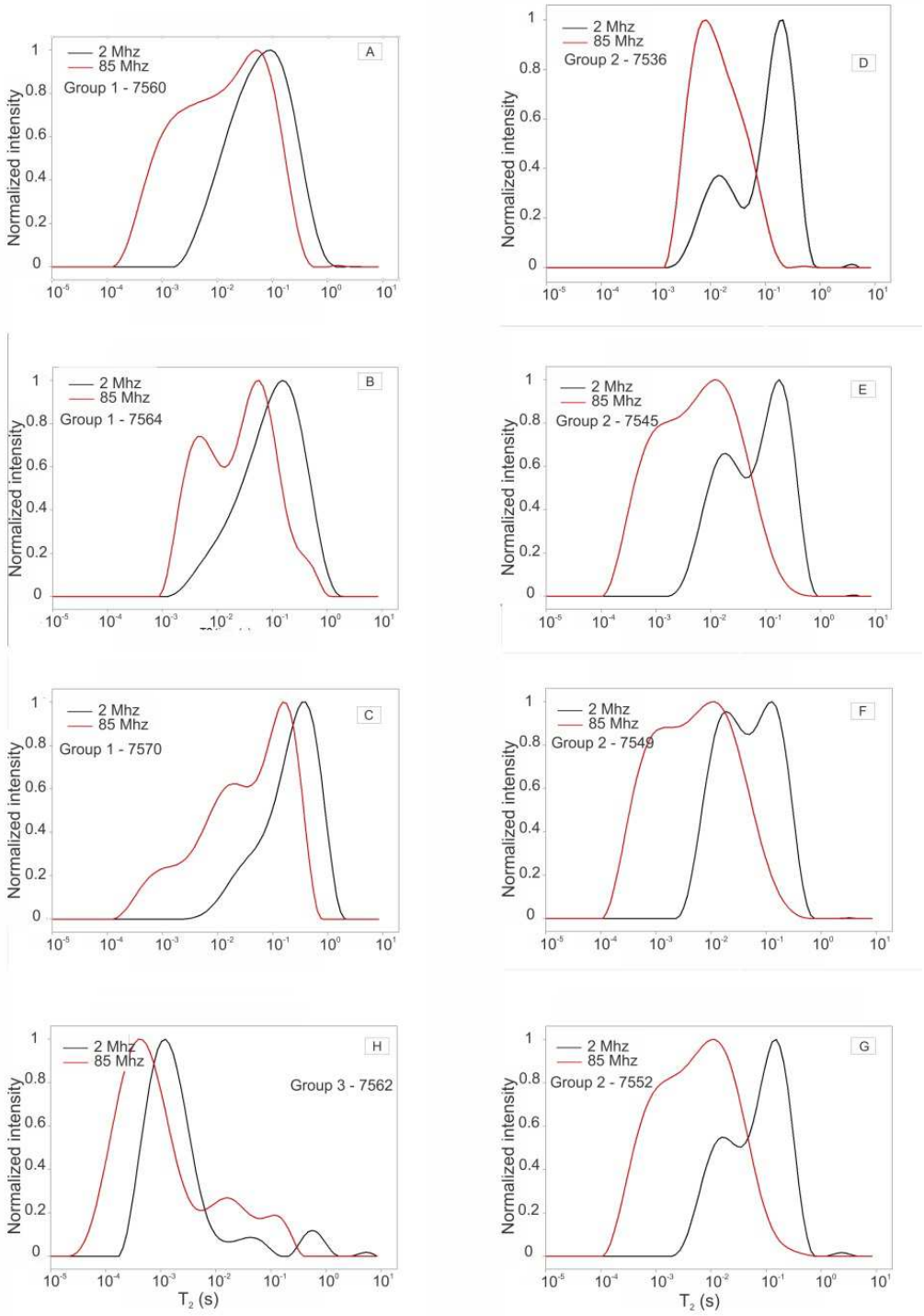

Figure 39 – 2MHz and 85 MHz T_2 distributions of Groups 1, 2 and 3 (A-H).

D-T_2 maps for representative reservoir samples are shown in Figure 40. The non-reservoir sample did not show meaningful results due to its very low porosity. Group 1 and Group 2 samples show very similar behaviors for the diffusion on their macropores, which are defined by time of diffusion for 40 ms. Using the method PFG-STE, during the diffusion time the magnetization is on longitudinal axis and the relaxation is by T_1, which minimizes the loss

of magnetization during this time (Tanner, 1970). So, this result presents only pores with relaxation times greater than the diffusion time. The longest T_2 time is closer to bulk water translational diffusion coefficient. This is compatible with the dominance of larger pores. The shortest T_2 is correlated with the lower translational diffusion coefficient and indicates restricted diffusion from the smaller pores into macropores range.

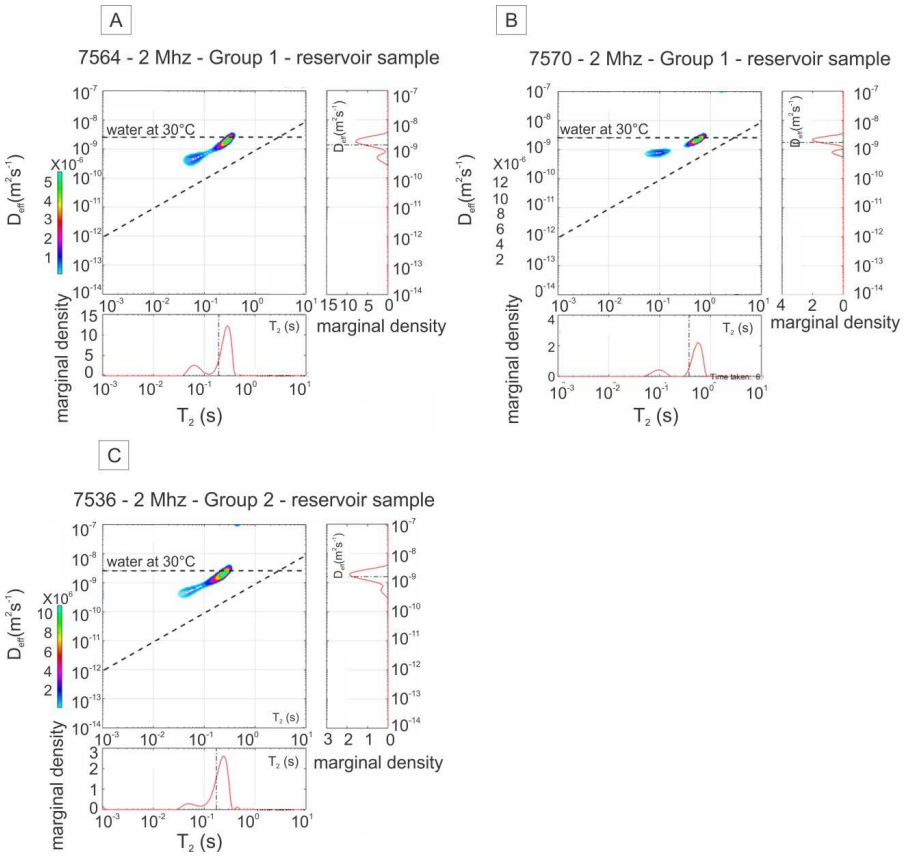

Figure 40 – D-T_2 maps with 40 ms diffusion time for representative samples of all.

5.2.5 **Discussion**

5.2.5.1 Intergranular and secondary porosity.

Samples present heterogeneities at the hand-sample and thin-section scales that could be responsible for part of the observed NMR responses. The three groups of samples of Água Grande formation studied here present particular characteristics at different scales. Group 1 samples present fining upward texture, relatively lower content of chlorite coating, lower magnetic susceptibility, smaller porosity values and wider T_2 distributions. Group 2 samples show well-defined parallel laminations, higher contents of chlorite coating, relatively higher magnetic susceptibility, bigger porosity values and bimodal T_2 distributions. Group 3

corresponds to the non-reservoir Sample 7562, which is high cemented sandstone with almost no porosity. It has higher values of magnetic susceptibility and microporosity is predominant over macroporosity, according to the NMR data.

In the macropore range, the NMR T_2 times of Group 1 samples are higher than that observed for Group 2 samples. However, contrary to what would be expected the first group shows lower porosity. NMR measurements can be affected by the presence of magnetic gradients at the pore surface. Higher internal magnetic field gradients due to the paramagnetic chlorite are known to shift the T_2 values to smaller relaxation times (Kleinberg et al., 1994, LaTorraca et al., 1995, Rueslatten et al., 1998). In addition, clays generate micropores that also cause faster relaxation (LaTorraca et al., 1995). In our samples, the paramagnetic chlorite coating controls the low magnetic susceptibility, therefore, an internal gradient could be expected for samples with a higher content of grain coating in high magnetic fields. This effect is observed on Figure 39, when we compare 2 MHz and 85 MHz T_2 distributions for low susceptibility samples of Group 1 and high susceptibility samples of Group 2.

The T_2 shift to lower values for Group 1 samples is much less pronounced than in Group 2. Moss and Jing (2001) showed similar shifts to shorter T_2 times in smectite-bearing samples. They associated this effect to smectite expansion due to water infiltration between clay layers. Since our samples are devoid of smectite or other expansible clay minerals, the observed shift must be caused by other factors such as different pore sizes or diffusive coupling. It is also interesting to note that T_2 distributions obtained with different times between π RF pulses in 2 MHz for Group 2 samples, which show the highest magnetic susceptibilities, do not vary. This result implies that at low fields the magnetic field inhomogeneities do not affect the T_2 distribution significantly, at least for the chlorite contents of the studied Água Grande reservoir rocks. These results are different from those obtained by Zhang et al (2001) who interpreted the shift as caused by an internal field gradient in the chlorite-bearing sandstones.

NMR responses for macropores can also be compared with μCT results (Figure 36). This technique has a 5 μm spatial resolution, and thus suited only to image the macropores. Results show that both Group 1 and Group 2 samples present similar pore size distributions and longest T_2 times peaks ($\geq$0.1 s) are correlated to the intergranular macropores whose modes are centered in 30 μm for both groups.

Both groups of reservoir samples showed two regions with restricted diffusion on D-T_2 maps (Figure 40). During the evolution of diffusion, the particles continue to relax by the

effect of T_1, the micropores whose T_1 times are smaller than diffusion time are not measurable (Schmidt-Rohr & Spiess, 1994). The time used for diffusion was 40 ms, therefore these result represent only the macropores. The longest T_2 restricted diffusion is due to intergranular macropores, while the shortest T_2 restricted diffusion is here interpreted as a result of the secondary porosity related to dissolution of feldspar and clay intraclasts. The peak related to dissolution of feldspar is sometimes as important as that of free water. This is evidenced on sample 7560, whose T_2 relaxation distributions show a unimodal curve, whereas dissolution of feldspar is represented by T_2 peaks at 0.022 s and 0.063 s with magnitudes close to that of intergranular macropores (Figure 38). Sample 7560 has 10.4% of porosity, from which 5% is due to feldspar dissolution. On T_2 distributions, the secondary porosity appears mainly on Group 1 samples associated to the low intensity 0.01 s peak.

Feldspar dissolution is also present in Group 2 samples, so we interpret that intermediated peak will also be present in Group 2 as in Group 1, however the displacement of the longest T_2 peak to shorter times in samples of Group 2 samples could mask it. Thin sections show that feldspar pore sizes vary from 4 μm to a maximum of 30 μm in sample 7560 where detrital feldspar was intensely dissolved.

All samples present pore filling kaolinite/dickite grains that range in size from micropores as having <1μm to 5μm and form a secondary microporosity (see appendix 2). Kenyon (1997) defined relaxation times $T_2 \leq 0.01$s as being the micropores, therefore we interpret the T_2 peak of ~ 0.01-0.025 s as due to kaolinite/dickite and chlorite coatings.

5.2.5.2 Chlorite coatings and pore coupling

Compositional maps (Figure 35) showed a higher percent iron on grain surfaces of samples with more intense peaks in this time range (~0.015s). Thus, the microporosity due to chlorite coatings can be related to the shortest reservoir T_2 times. The non-reservoir sample, on the other hand, shows a high NMR T_2 intensity peak at much shorter times (0.001 s). This rock present almost no porosity, so very short time is interpreted as due to clay bound water of clay pore-filling, which is in agreement with the interval proposed by Straley et al (1995) and Kausik et al (2011), who define T_2 of $\leq$ 3ms and ~1ms as due to clay bound water.

Several studies have shown the effect of pore coupling on NMR relaxation (e.g., Straley et al., 1995, Kenyon, 1997, Zhang et al., 1998, 2001, Anand & Hirasaki, 2005). Chlorite flakes, which are the coating on the studied sandstones, are modeled in terms of their

NMR response as microchannels perpendicular to the pore walls, forming micropores connected with the adjacent macropore (Straley et al., 1995; Kenyon, 1997) (Figure 41).

The diffusion of protons from macropores to micropores affects the NMR response but not always in a uniform manner. Kenyon (1997) described two models for the NMR response according to the degree of coupling between clay flakes connected channels and central macropores. When diffusion coupling is not observed, two different relaxation times appear at the T_2 distribution, the shorter one being correlated with the width of chlorite channels, the longer is being correlated with the macropore.

When diffusion coupling is very efficient, the magnetization of the whole pore is uniform both in the channels and in the center of the macropore. In this case, only one relaxation time is obtained and the system is at the fast-diffusion limit. However, the S/V will increase due to the roughness of the pore surface induced by the presence of the clay flakes causing a decrease in T_2 values. According to Anand & Hirasaki (2005) the intermediate coupling is characterized by two distinct modes which are correlated with distinct pores, but the intensity of the T_2 distribution peaks are not correlated with the true porosity values. In this case, the diffusion is fast enough to couple some micropores, but not all of them.

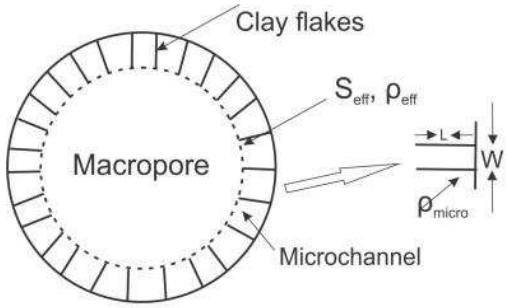

Figure 41 – Model for diffusion coupling (adapted from Kenyon, 1997).

The NMR T_2 relaxation distributions for Água Grande reservoir samples suggest an intermediate diffusion coupling. In these samples, the T_2 time peak on 0.01 s is not proportional to porosity and presents a significant displacement towards shorter T_2 times of macropores.

Figure 35 shows qualitatively that the content of iron on quartz grains has a good correlation with the intensities of NMR 0.01 s peak. Anand & Hirasaki (2005) also recognized by in chlorite coated sandstones from North-Burbank and described an intermediate coupling for water and strong coupling for hexane. Zhang et al (2001) also studied rocks of this region.

They described internal field gradients on NMR measurements from chlorite coated sandstones by modifying the echo time, in an experiment similar to the one performed here. They obtained T_2 ~0.008 s for micropores due to chlorite coat and T_2 ~0.06 s for macropores for for brine saturated samples. Before that, Zhang et al (1998) calculated the surface relaxivity for T_2 at a short echo spacing (0.2 ms) (the same echo time used in this paper) and obtained 84±13.0 μm/s.

Compared to the fast-diffusion case, in intermediate diffusion the time that one particle diffuses across the pore T_d increases relative to the wall relaxation time T_s in the channels of chlorite flakes:

$$\frac{T_D}{T_s} = = \frac{L^2/D}{W\rho/} = \frac{\rho L^2}{DW} \tag{47}$$

(Kenyon, 1997)

where L is the length of the chlorite channel, W is the width of the chlorite channel, ρ is the relaxivity and D is the diffusion coefficient. Thus, in the deeper and narrower part of the channels, the magnetization decays faster than at the opening of the micropore.

Addionally, Kenyon also proposed a model to calculate the relaxivity for intermediate diffusion coupling behavior:

$$\rho_{eff} = \sqrt{\frac{\rho_{microD}}{W}} \tag{48}$$

(Kenyon, 1997)

where ρ_{eff} the effective relaxivity determined for the macropores, ρ_{micro} is the microscopic surface relaxivity, D is the diffusion coefficient of water in clay layers, and W is the separation of clay layers (Figure 41).

Figure 33F, Figure 33G and Figure 33H show that channels of chlorite flakes in Água Grande reservoir samples present L ~5μm and W~5-10 μm, Group 2 samples showing much higher contents of coating then Group 1 sample.

We first estimate the relaxivity of the sample with the lowest coating contents, Sample 7570, for which a fast-diffusion model can be assumed. From equation 44, the surface relaxivity for macropores in this sample is 27.54 μm/s and the relaxivity of micropores due to chlorite is 100 μm/s. The effective surface relaxivity for macropores in the other samples can be estimated using equation 48 using the calculated relaxivity for the micropores, ρ_{micro} = 100

μm/s, $D=10^{-6}$ cm^2/s (Kleinberg, 1996). Thus, from equation 48 the effective surface relaxivity in the other samples is 31. 62 μm/s.

5.2.6 **Conclusions**

Samples from Água Grande Formation can be divided into three groups according to their texture, composition, petrophysics and NMR T_2 distribution properties. Group 1 samples show finning upward texture, low contents of chlorite coating, intermediate to low magnetic susceptibility, lower porosity and a wide distribution of NMR T_2 time distribution. Group 2 samples show well defined parallel laminations, a higher content of chlorite coating, relatively high values of magnetic susceptibility, higher porosity and bimodal NMR T_2 time distribution. In T_2 distributions of the two groups of reservoir samples the largest peak (>0.1 s) is due to intergranular macropores, the intermediate peak is due to feldspar or clay intraclast dissolution and the shortest peak (~0.01 s) is due to the chlorite peak, defining the 3 log-gaussians or peaks. The samples of group 2 show only two peaks because the shift of longer T_2 to shorter times hides the intermediate peak, which represents the porosity due to feldspar/clay intraclasts dissolution. In the non-reservoir sample used for comparison the microporosity is predominant and relates to the clay bound water.

In chlorite-coated samples, the T_2 shift to shorter times is interpreted as due intermediate diffusion coupling between micropores and macropores. This drift to shorter T_2 times could be an indicative of clay coatings on well-logging tools if the considered stratigraphic intervals present comparable pore size distributions.

APPENDIX 1

Methods

2.1. Transmitted-light optics

Blue epoxy-impregnated thin sections were examined with transmitted-light optical microscope to identify the minerals, the textural framework and the presence and nature of cements. The microporosity was characterized with scanning electron microscopy due to microscope resolution.

2.2. Scanning electron microscopy (SEM)

We utilized the INSPECT F50 FEI scanning electron microscope from Instituto de Física de São Carlos, Universidade de São Paulo, to identify and characterize the clay

coatings on detrital host grains and measure the size of the pores. Energy Dispersive Spectroscopy (EDS) was used for semi-quantitative chemical mapping of O, Al, Fe, Mg and Si.

2.3. Porosity (ϕ) and permeability (k) measurements

Porosity and permeability were measured on each sample. Porosity was determined using three methods: thin-section point counting, Helium expansion 2500 PSI and density after saturation (Table 5). Values obtained with the different methods present a good correlation. The permeability was determined using a Hassler cell (Table 5). A Core lab Helium Permeameter (model n. 3020-124 and serie A7520) from Petrobras/SA was used for measurements.

2.4. Micro-CT (X-ray micro computed tomography)

X-ray Micro-CT (μCT) allowed the three-dimensional visualization of the pore structure of samples and estimation of pore size distribution. In addition, the porosity also was obtained by this method. Measurements were performed with a SkyScan 1272 scanner by Bruker (USA) from Instituto de Física de São Carlos, Universidade de São Paulo, and were analyzed using the Bruker μCT software (CTAn). Samples correspond to fragments of about 0.005 cm^3 in volume collected directly from the original samples.

2.5. XRD (X-ray diffraction)

Clays are very common components of sedimentary rocks, but identify them is not always a trivial task due to the variable range of physicochemical properties of clay minerals, including their composition, morphology, grain size, swelling and cation exchange (Wilson et al, 2014). Thus, X-ray diffraction is a useful technique to distinguish clays, mainly smectite and its mixed-layer, based on their expansion with ethylene glycol. Here, a Bruker D8 Advance Da Vinci Diffractometer from Instituto de Geociências da Universidade de São Paulo (IGc/USP) was used to identify the types of clays present in the samples.

2.6. Magnetic susceptibility and hysteresis

Magnetic susceptibility differences within the rock samples caused by the presence of paramagnetic minerals or impurities can induce field inhomogeneity in the pore space, causing an increase in $1/T_2$ relaxation rates (Kenyon, 1997; Keating and Knight, 2007 and Washburn et al, 2008). Thus, these measurements are important to understand eventual

contrasts on the T_2 NMR response in the porous media. We used the Susceptmeter KLY-4S-Kappabridge by AGICO operating at 976 Hz at the Laboratório de Paleomagnetismo da Universidade de São Paulo (USPmag). Hysteresis measurements were used to investigate whether the magnetic susceptibility was carried by ferromagnetic or paramagnetic minerals, and the relative contribution of each magnetic phase. Measurements were performed in a Princeton Measurements Corp. vibrating sample magnetometer with a peak field of 1T also from USPmag.

APPENDIX 2

Table 1- Compositional analysis of samples (%)

Group		1			2				3
Minerals		7560	7564	7570	7536	7545	7549	7552	7562
Primary minerals	Quartz	87.85	87.45	89.39	82.37	83.86	90.03	85.78	56.00
	Plagioclase	1.96	2.96	1.10	4.63	4.57	0.43	3.26	8.00
	Perthite	0.39	0.74	0.36	0.42	0.41	0.43	0.82	0.33
	Microcline	0.00	0.00	0.00	0.00	0.00	0.00	0.40	0.00
Diagenetic minerals	Caulinite (dickite)	3.00	2.96	3.33	4.0	3.33	2.33	4.00	6.67
	Quartz	1.56	2.67	3.30	0.42	0.41	0.87	0.40	0.00
	Chalcedony	0.79	0.00	0.00	0.42	0.00	0.87	0.40	0.00
	Illite/ Smectite	0.00	0.00	0.00	0.00	0.00	0.00	0.00	5.00
	Illite	0.00	0.00	0.00	0.00	0.00	0.00	0.00	3.34
	Anatase	0.00	0.37	0.36	1.26	0.41	0.43	0.40	4.67
	Dolomite	0.00	0.00	0.00	0.00	2.90	1.74	0.82	0.00
	Albite	1.96	0.00	0.00	0.00	0.83	0.43	0.82	0.00
	Pirite	0.00	0.74	0.36	0.42	0.00	0.00	0.00	2.66
Accessory minerals	Cianite	0.00	0.00	0.00	0.42	0.00	0.00	0.00	0.00
	Biotite	0.00	0.00	0.36	1.26	0.83	0.00	0.40	1.67
	Muscovite	0.00	0.00	0.00	0.84	0.41	0.43	0.00	1.33
	Epidote	0.00	0.00	0.00	0.42	0.00	0.00	0.00	0.33
	Zircon	0.39	0.37	0.00	0.42	0.00	0.43	0.82	1.00
	Turmaline	0.00	0.37	0.00	0.00	0.41	0.43	0.40	0.67
Silcrete		0.39	0.74	0.36	1.66	0.83	0.43	0.40	0.00
Pelitic intraclasts		1.18	1.11	0.74	0.00	0.00	0.00	0.00	0.00
Mud matrix		0.00	0.00	0.00	0.00	0.00	0.00	0.00	8.00

Draft to be submitted to the Journal of Applied Geophysics

5.3 Magnetic matrix effects on NMR relaxation times in porosity-preserved sandstones: A case study in Solimões Basin

Marta Henriques Jácomo[a], Ricardo Ivan Ferreira Trindade[a], Everton Lucas-Oliveira[c], Tito José Bonagamba[c]

[a]Instituto de Astronomia, Geofísica e Ciências Atmosféricas, Universidade de São Paulo, São Paulo, Brasil.

[c] Instituto de Física de São Carlos, Universidade de São Paulo, São Carlos, Brasil.

Abstract

Nuclear Magnetic Resonance (NMR) estimates of pore distribution can be strongly affected by the presence of magnetic gradients between the pore and the grain's surface. Here we investigate the effect of the magnetic matrix on Uerê and Juruá reservoir sandstones (Solimões Basin, Brazil), where quartz, illite and hematite coatings developed and contributed to the partial preservation of the original porosity. Samples were divided into three groups based on petrographic observations, magnetic susceptibility, type of iron-bearing minerals and the shape of T_2 NMR distributions. Group 1 consists of subarkoses with variable amounts of coatings of microcrystalline quartz or undifferentiated silica on the quartz grains. Group 2 also contain microquartz coatings but its mineral matrix contains iron-bearing minerals such as Fe-dolomite, siderite and pyrite, besides Fe-illite. Samples from Juruá Formation form Group 3, which consists of hematite-coated sandstones cemented by quartz overgrowths, albite, hematite and pore-filling illite. Macroporosity for these samples is indicated by a peak above 10^{-1} s in T_2 time distributions, whereas intermediate peaks (0.1-0.01 s) are related to mineral dissolution. The Groups 2 present a slight displacement, while Group 3 samples present significant shifts towards shorter times (~5 X 10^{-2} s). These shifts are directly related to the magnetic mineralogy of the rocks, with Group 2 and Group 3 samples presenting the highest magnetic susceptibilities. The T_2 displacements in the studied samples are caused mainly by relaxitivity in Group 2, related to the clay flakes along the pore surface, and diffusion in Group 3, related to the strongly magnetic hematite coatings.

5.3.1 **Introduction**

The porosity is of primary interest in reservoir quality investigations, affecting estimations of the volume of hydrocarbons and the fluid flow within sandstones (Morad et al., 2010; Worden et al., 2018). Due mainly to compaction, there is a normal loss of porosity with depth in siliciclastic reservoirs (Bjørkum and Nadeau, 1998; Worden and Burley, 2003; Ehrenberg et al., 2008; Taylor et al 2010). However, some conditions, such as the formation of clay or microcrystalline quartz coatings covering detrital quartz grains can inhibit the quartz overgrowth cementation, as well as chemical compaction through intergranular pressure dissolution, preserving the porosity even at great depths (Bloch et al., 2002). A significant amount of work has been performed on the macro-porosity structure of these rocks and the processes behind the preservation of their porosity (Moraes and De Ros, 1990, Ajdukiewicz et al., 2010, Dowey et al., 2012; Worden et al., 2012; French and Worden, 2013; Worden et al., 2018). But only few studies have been dedicated to understand their micro-porosity (e.g., Ajdukiewicz et al., 2010, 2012; Jácomo et al., 2018, 2019).

Nuclear Magnetic Resonance (NMR) tools are particularly well-suited for the characterization of the microporosity structure of rocks, providing information on the size-distribution of micropores and their relation with larger pores in the rock (Kenyon et al., 1989; Straley et al., 1995; Kenyon, 1997). In the anomalous porosity context, some studies reported NMR data for sandstones coated by microcrystalline quartz (Fleury, 2007; Sousa, 2012; Livo, 2016; Jácomo et al., 2019) or by clay (Straley et al., 1995; Kenyon, 1997; Zhang et al., 1998, 2001; Anand and Hirasaki, 2005; Jácomo et al., 2019). Recently, we used NRM analyses to describe the micropore structure of sandstones presenting anomalous porosity in two case-studies. One case-study was dedicated to the well-known Fontainebleau sandstones, which are composed almost exclusively of quartz (without significant clay or other iron-bearing minerals contribution). In this case, the correlation between magnetic relaxation times and pore size can be obtained with relative success (Fleury, 2007; Sousa, 2012; Livo, 2016; Jácomo et al., 2019). NRM methods allowed us to investigate the interconnection between the micropores formed in the multi-layered coating of these rocks and the preserved macropores (Jácomo et al., 2019). The other case-study, where the porosity was preserved due to paramagnetic chlorite coatings in the Recôncavo Basin sandstones (Jácomo et al., 2018), the relation between magnetic relaxation times and pore size is more complicated by the contribution of the diffusion coupling between the clay coatings and the macropores (Straley et al., 1995; Kenyon et al., 1997; Zhang et al., 2001; Anand and Hirasaki, 2007; Keating and

Knight, 2012; Grunewald and Knight, 2009; Jácomo et al, 2018). In addition to these two processes described above, another important factor that affects the relation between magnetic relaxation times and pore size distribution is the presence of ferrous minerals or impurities, which may interfere significantly with the NRM signal (Keating and Knight, 2007; 2010; 2012).

In the present contribution, we focus on sandstones of the Uerê and Juruá Formations, Solimões Basin (Brazil), in which different kinds of coatings occur in the same Basin. Due to its intrinsic heterogeneity, these units allow to explore different scenarios of porosity preservation in sandstones; from almost clean sandstones exclusively coated by micro-quartz, to sandstones with significant contribution of iron-bearing minerals, including coatings of clay and hematite, which can affect the NMR pore size distribution estimations. The pore space of these rocks is here studied using Nuclear Magnetic Resonance (NMR) and rock magnetic measurements such as magnetic susceptibility (χ), magnetic hysteresis, Isothermal Remanent Magnetization (IRM) and First-Order Reversal Curves (FORC). Rock magnetic measurements are able to provide information on the type, grain-size and internal-domain structure of magnetic minerals even when they occur in very tiny amounts in the rocks. We also performed observations with transmitted-light optic microscope, scanning electron microscope (SEM) and micro-computed tomography (micro-CT).

5.3.2 **Basic NMR relaxation concepts**

The NMR has been widely used in Petrophysics for the characterization of the rock's pore space and fluid content. The NMR measures the net magnetization of hydrogen atoms in the presence of an external magnetic field. NMR measurements involve sequences of hydrogen proton alignment to a strong magnetic field followed by spin tipping or flipping, and magnetic relaxation. T_1 is the longitudinal relaxation time and relates to interactions among spins and the neighborhood. T_2 is the transversal relaxation times and results from spin-spin interactions. Here, we used the transversal relaxation T_2 since it is the relaxation time usually used in NMR log borehole exploration. It is defined as:

$$\frac{1}{T_2} = \frac{1}{T_{2B}} + \frac{1}{T_{2S}} + \frac{1}{T_{2D}} \tag{49}$$

where T_{2B} is the intrinsic relaxation, T_{2S} is the surface relaxation and T_{2D} is the relaxation rate due the molecular diffusion.

Three mechanisms control the NMR relaxation times due to interactions between fluids and rocks. The first is the intrinsic magnetic relaxation (T_{2B}), which is mostly controlled by fluid properties such as viscosity, amounts of paramagnetic dissolution, temperature and pH. The second is the surface relaxation (T_{1S}), which is controlled by grain mineralogy and the surface to volume ratio of pores. The third mechanism is diffusion relaxation (T_{2D}), which is related to the effects of magnetic grain mineralogy on the diffusing water molecules; in this case, molecules diffuse into areas with non-uniform magnetic fields or feel a restriction on their movement. Generally, the bulk term is neglected since the other two mechanisms dominate the signal. In the fast-diffusion regime (Browstein & Tarr, 1979), where protons travel and relax at grain surface during the NMR experiment:

$$1/T_2=\rho_2\,(S/V) \tag{50}$$

where ρ_2 is the pore surface relaxivity for T_2 times; S/V is the surface/volume ratio. The relaxation time rate due to molecular diffusion in a magnetic field gradient is given by:

$$\frac{1}{T_{2Diffusion}}=\frac{D(\gamma G T_E)^2}{12} \tag{51}$$

where D ($cm^{2/}s$) is the molecular diffusion coefficient, γ is the gyromagnetic ratio, G is the magnetic field gradient (G/cm) and TE is the inter-echoes time used in the CPMG sequence measurements (Carr-Purcell-Meiboom-Gill).

5.3.3 **Methods**

5.3.3.1 Transmitted-light and scanning electron microscopy (SEM)

Blue epoxy-impregnated thin sections were examined with transmitted-light optical microscope to identify the minerals and pores types, the textural framework and the presence of cements. These parameters were determined by counting 300 points for each sample. The SEM images were obtained using a Zeiss Sigma Vacuum Field Emission SEM coupled to an Oxford Instruments EDX Penta Precision detector to identify the geometry and size of micropores and the clay and microcrystalline quartz coatings.

5.3.3.2 Porosity (ϕ) and permeability (k) measurements

Porosity and permeability measurements were performed for each sample by Petrobras/SA using a The Core lab helium-expansion at 2,500 psi and a Core lab helium permeameter (model n. 3020-124), respectively.

5.3.3.3 X-ray micro computed tomography (micro-CT)

The micro-CT is a non-destructive technique which allows a three-dimensional visualization through the reconstruction of X-ray image projections. Since the degree of X-ray absorption by each mineral, particle or fluid varies with density and atomic number, rock matrix and pores can be easily discriminated with this technique. In this work, measurements were performed using a SkyScan 1272 scanner by Bruker (USA) in fragments of rocks about 0.005 cm^3 in volume.

5.3.3.4 Nuclear Magnetic Resonance (NMR)

NMR measurements were performed using Redstone^{TM} Tecmag spectrometers operating at 2 and 85 MHz. The samples were saturated with distillated water using a vacuum pressure of 90 kP, where the samples remained in the water for 60 min. CPMG routines were performed with inter-echo spacing times of 200 μs, detecting 40,000 echoes. The number of scans for each experiment at 2 and 85 MHz were 32 and 8, respectively. To convert the decay functions into a T_2 distribution an inverse Laplace transform (ILT) implemented in our NMR Group was applied; it uses the curvature-smoothing regularization method (Borgia et al., 1998; Kenyon, 1997).

5.3.3.5 Magnetic susceptibility and hysteresis

The difference of magnetic susceptibility between the fluid and the grain mineral surface induces field inhomogeneity in the pore space, contributing to faster $1/T_2$ relaxation rates (Keating and Knight, 2007). Therefore, the magnetic characterization of samples is essential for NMR interpretation. A MFK1-FA AGICO susceptometer operating at 976 Hz was used for magnetic susceptibility measurements. Magnetic hysteresis loops were obtained using a Princeton Measurements Corp. vibrating sample magnetometer with a peak field of 1 T to define which types of magnetic minerals (ferromagnetic, paramagnetic or diamagnetic) are associated with the magnetic susceptibility signal.

5.3.3.6 Isothermal Remanent Magnetization (IRM) and First-order reversal curve (FORC)

The IRM curves were performed exposing the samples to a DC field varying from 0.01 to 1 T in 30 steps, along the same direction at room temperature. For that, we used a 755-1.65 DC SQUID magnetometer (2G Enterprises), housed inside a magnetically shielded room with ambient field <500 nT. The First-order reversal curves (FORC) were performed using a

Princeton Alternating Gradient Magnetometer Micromag TM 2900. In this experiment, the field varies from ±1 T with field steps of 10 mT. The distributions were computed with the XFORC software (Zhao et al., 2015).

5.3.4 **Results**

5.3.4.1 Basic Petrophysics, Petrography, electron microscopy and micro-CT data

The Uerê sandstones are oil exploration targets of the Solimões Basin (Brazil). Although they show a great depositional continuity, they are laterally heterogeneous, making oil exploration on this unit a very hard task (Lima and De Ros, 2002). All the seven samples from Uerê Formation (R2852, R2853, R2854, R2855, R2856, R2860, R2863) present IGV values between 21 to 43%, porosity (He) from 15 to 23% and permeability from 3 to 152 mD (Table 6). The other two samples (R2877 and R2875) are from the Juruá Formation, which present hematite coatings instead of quartz microquartz. IGV values in these samples are 24 and 31%, the porosities are 19 and 10% and permeability are 11 and 0 mD, respectively (Table 6 and appendix).

Table 6 – The physical properties of the measured samples. Dia is diamagnetic, Para is paramagnetic and Ferro is ferromagnetic.

Groups	**1**					**2**		**3**	
Petrophysics	**R2852**	**R2856**	**R2860**	**R2863**	**R2855**	**R2853**	**R2854**	**R2877**	**R2875**
He Porosity (%)	20	22	16	23	21	15	15.9	19	10
Porosity (micro-CT)	22	23	13	15	19	17	7	11	10
Macroporosity (thin sections)	17	20	4	5	11	2	11	9	0
Permeability (mD)	152	70	3	12	12	3	10	11	0
Density	2.62	2.65	2.58	2.65	2.66	2.63	2.72	2.69	2.65
Magnetic Susceptibility	22.5	19.9	15.2	9.94	17	45.5	47.9	49.6	123.6
Magnetism	Dia + Ferro	Dia + Ferro	Dia + Ferro	-	Dia + Ferro	Para + Ferro	Para + Ferro	Para + Ferro	Para + Ferro

Based on our petrographic observations, the amount of magnetic susceptibility (χ) and type of iron-bearing minerals in the samples, which directly influence the rock magnetic data, we have subdivided our samples in three groups. Group 1 comprises samples R2852, R2856,

R2860, R2863 and R2855 and consist of fine-grained and poorly-sorted subarkoses (*sensu* Folk, 1968) with variable amounts of coatings of microcrystalline quartz (from 0.3 to 11%) or undifferentiated silica (from 0 to 8%) on the quartz grains (Figure 42). Other diagenetic constituents are quartz overgrowths (from 1 to 10%), albite (from 4 to 11%), pore-filling illite the (from 1 to 6%), illite coatings (0 to 3%), anhydrite (from 0 to 3%), Fe dolomite (from 0 to 3%), dolomite (from < 1 to 2%) and pyrite (< 1 to 1.6%). Samples R2853 and R2854 form the Group 2. They present microquartz coatings (<1 and 4%) as Group 1 samples, but their mineral matrix contain iron-bearing minerals such as Fe-dolomite (4% in R2853), siderite (1% in R2853), and pyrite (1.5% in R2853). Secondary porosity was locally generated by dissolution of bioclasts and feldspars, with kaolinite filling the dissolved feldspar pores. These samples contain the highest amounts of pore-filling displacive chalcedony (2% and 33%) and IGV (43% and 45%) (Appendix).

The Juruá Formation R2875 and R2877 samples form the group 3 which correspondes to poorly-sorted arkose and moderately-sorted subarkose, respectively (*sensu* Fol, 1968;). They consist of hematite-coated sandstones cemented by quartz overgrowths (from 7 to 14%), albite (from 6 to 13%), hematite (from 4 to 7%) and pore-filling illite (<1%). R2875 sample has also ankerite (~2%), anhydrite (<1%), Fe calcite (<1%), and mud pseudomatrix (<1%). The eodiagenetic mineralogy revealed that eodiagenesis occurred under dry climate conditions in a continental environment (Elias et al., 2004).

The pore size distributions obtained by micro-CT images show normal to close to normal distributions, in which the median of microquartz-coated samples vary from 16.4 to 18.3 μm (± 0.9 μm). Sample R2877 has median pore size of 22.6 μm, which is similar to that of microquartz-coated samples considering the resolution of 2 μm of micro-CT images. On the other hand, the other hematite-coated sample (R2875) has a median of 11.6 μm, which is significantly different from that of the other samples (Figure 43). Thin section analysis shows that primary intergranular and secondary pores due to dissolution of feldspar are the main forms of macroporosity. Their pore sizes vary, respectively, from 10 to 90 μm and from 3 μm to 12 μm. SEM images showed that micropores are mainly contained among microcrystalline quartz crystals (pore size between 623 nm and 2 μm) and illite flakes (pore sizes between 1 and 5 μm) (Figure 42).

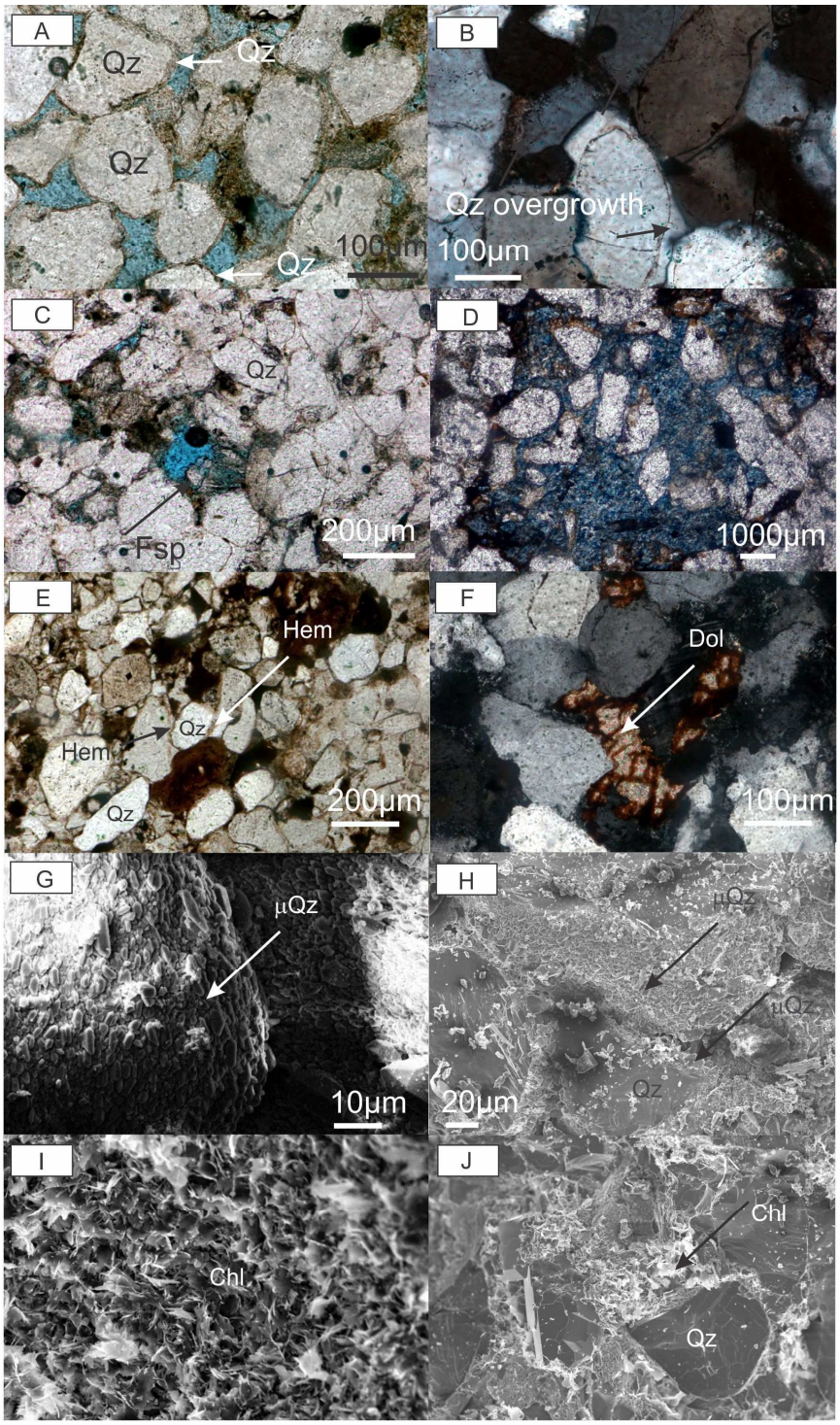

Figure 42 – A) sandstones with quartz microcrystalline coatings around the quartz grains; uncrossed polarizers; B) sandstone cemented by quartz overgrowths; crossed polarizers; C) porosity from the dissolution of feldspar grain; uncrossed polarizers; D) microporosity related to dissolution of cement or feldspar; uncrossed polarizers; E) sandstone with hematite coatings uncrossed polarizer; F) ferroan dolomite pore-filling cement; crossed polarizers; G) and H) microquartz coatings covering quartz grain surfaces; scanning electron microscopy; I) chlorite coating; J) chlorite filling the pores of sandstone; scanning electron microscopy.

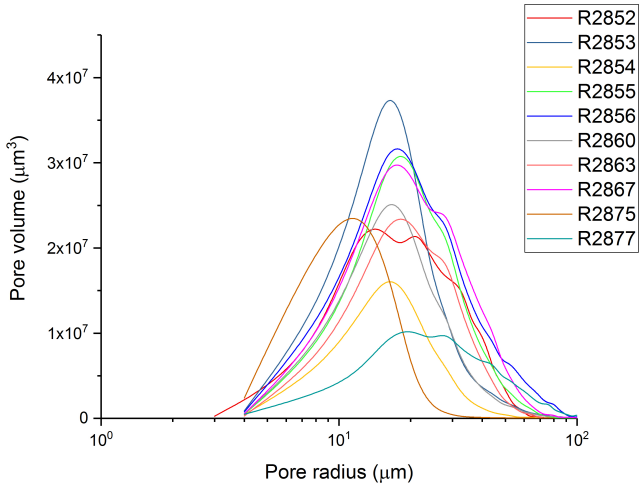

Figure 43 – The micro-CT pore size distribution showing similar median values, which vary from 15 to 18 μm, with exception of R2875 sample, which has a 11.57 μm median pore radius.

5.3.4.2 Magnetic Properties

Although the petrographic description shows only the presence of paramagnetic pyrite (R2853, R2855, R2860, R2863, R2867), siderite (R2853), ankerite (R2853, R2855, R2860, R2863, R2877) and antiferromagnetic hematite (R2875 and R2877), hysteresis loops enabled the identification of ferromagnetic minerals in all samples (Figure 44) (Table 6). Samples from Group 1 (R2852, R2856, R2860, R2863 and R2855) have χ values between 10 and 23 X 10^{-6} SI. They show a dominant diamagnetic signal but also have minor amounts of ferromagnetic grains. This is indicated in hysteresis loops by positive slopes at low fields followed by a marked negative slope at high fields (Figure 44A-Figure 44D). Samples from Group 2 present χ values within the range 45 to 49 X 10^{-6} SI, and have a paramagnetic contribution in addition to the ferromagnetic and diamagnetic ones (R2853, R2854 and R2877) which appears in the hysteresis loops as a strong positive slope at low fields and a less positive slope at higher fields (Figure 44E-Figure 44 H). This analysis improves the petrographic description, which did not show big differences of paramagnetic contents (see Appendix). We can see that sample R2854 is dominated by paramagnetic minerals. Samples R2877 and R2875 (non-reservoir samples) present higher magnetic coercivity values in the hysteresis loops, typical of hematite, as indicated by the higher separation of curves close to

the origin (Figure 44G-Figure 44 H), in agreement with the petrographic observation of hematite coating in these rocks.

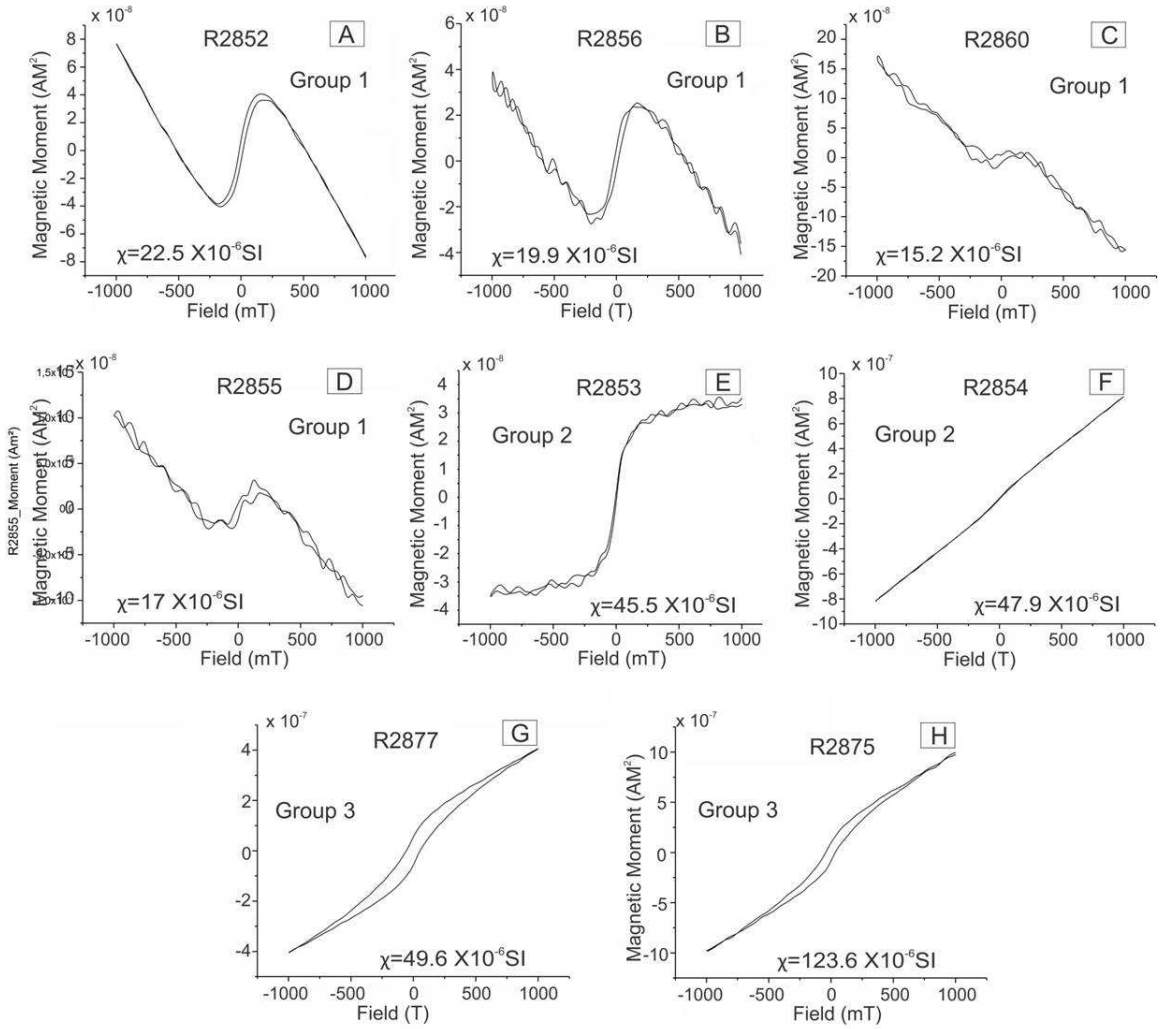

Figure 44 – The hysteresis loops for the studied samples showing typical diamagnetic plus ferromagnetic contribution in samples R2852, R2856, R2860, R2855 (A-D). Samples R2853 (E), R2877 and R2875 (G-H) contain paramagnetic and ferromagnetic phases (in addition to the diamagnetic matrix). Sample R2854 (F) has a dominant paramagnetic signal.

Ferromagnetic phases in all samples were further investigated through Isothermal Remanent Magnetization (IRM) curves (Figure 45). The IRM curves show that all samples of Group 1 (R2852, R2855, R2856 and R2863) except for R2860, contain only low coercivity magnetic phases, likely magnetite, since the magnetization tends to saturate below 300 mT (Figure 45). In contrast, high-coercivity magnetic phases (hematite or goethite) are evidenced in samples from Group 2 (R2853, R2854) and in hematite-coated non-reservoir samples (R2875 and R2877), for which the magnetization does not reach the saturation even after remanence acquisition at the peak field of 1000 mT (Figure 45) (Liu et. al., 2012). The

relative contribution of low and high coercivity phases to the IRM curves can be modeled using the method developed by Kruiever et al (2001). Modeled curves show that almost all samples contain low-coercivity magnetite, that accounts for 24% to 100% of the magnetic remanence in these rocks (Table 7). Sample R2875, in contrast, contains only high-coercivity hematite as a remanence carrier phase (Table 7).

The FORC experiment was performed on samples R2852, R2875 and R2877, in order to refine the description of their coercivity distribution and the domain structure of the remanence carrying minerals (e.g., Roberts, 2015). These samples comprise a mineralogy dominated by diamagnetic grains with a minor low-coercivity ferromagnetic component, likely related to magnetite (R2852), a mixture of low and high-coercivity minerals, likely magnetite and hematite (R2877) and a sample with only high-coercivity phases, likely hematite (R2875).

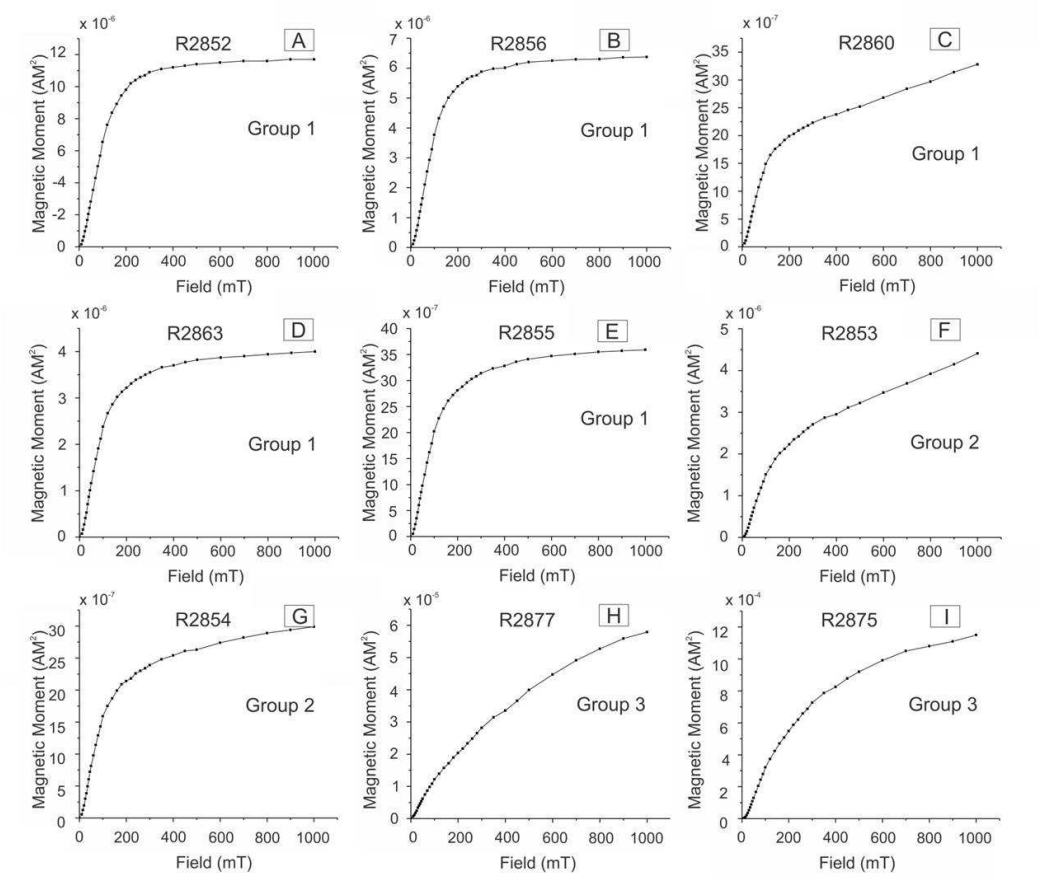

Figure 45 – IRM curves show the behavior of remanence carrying minerals (n this case magnetite and hematite). The remanent magnetization of samples R2852, R2856, R2863 and R2855 saturates below 1T, evidencing the presence of magnetite only. The magnetization of R2860, R2853, R2854 and R2877 samples do not saturate in 1T, evidencing the presence of hematite in addition to magnetite. Sample R2875 shows only hematite.

Table 7 – Magnetic coercivity and relative percentage contribution to the total remanent magnetization of ferromagnetic phases obtained in this study.

Sample	Magnetic coercivity (mT)	Percentage Volume (%)	Mineral
R2852	89.1	100	magnetite
R2855	87.1	100	magnetite
R2856	81.3	100	magnetite
R2860	66.1	58	magnetite
	676.1	42	hematite
R2863	81.3	100	magnetite
R2853	100	60	magnetite
	794.3	40	hematite
R2854	75.9	79	magnetite
	741.3	21	hematite
R2877	79.4	24	magnetite
	794.3	76	hematite
R2875	251.2	100	hematite

The FORC diagrams can be qualitatively interpreted through their forms in terms of the domain state of ferromagnetic grains, i.e. their grain-size. Figure 46 shows that R2852 comprises dominantly coarse (>1 μm) MD magnetite, probably as part of detrital grains, while samples R2875 and R2877 contain mostly fine-grained minerals, likely related to the grain coats (0.050 to 0.084 μm in size, Dunlop and Ozdemir, 1997).

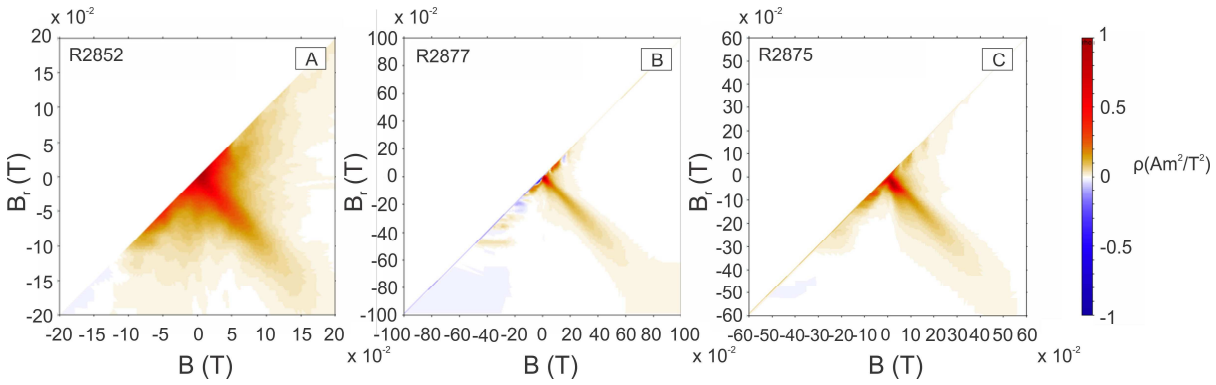

Figure 46 – FORC diagrams of representative samples showing the MD magnetite phase in R2852 sample (representative of Group 1 samples) and SD hematite phases in samples R2877 and R2875 (Groups 3 and 4, respectively).

5.3.4.3 Nuclear Magnetic Resonance

Figure 47 shows T_2 relaxation time distributions for all studied samples. The best log-normal fittings of 2MHz T_2 distributions define three to four families of pores (Table 8). According to the shape of T_2 distributions, we can classify the samples into three groups.

Group 1 is formed by the samples R2852, R2856, R2860, R2863 and R2855. It corresponds to the samples with the highest intensity peak above 10^{-1} s in T_2 time distribution and the peak with shortest T_2 times (~ 0.8 X 10^{-2} s) is not below or does not present a shift toward the value below of 0.3 X 10^{-2} s, which is defined as been the clay bound water limit in NMR borehole exploration (Allen et al., 1997) (black dashed line in Figure 47). Group 2 (R2853 and R2854 samples) is characterized by a shift in the highest intensity peak towards shorter times (~5 X 10^{-2} s) in T_2 distribution, shortening the differences between 0.7 X 10^{-2} s and 5 X 10^{-2} s peaks and making it resemble a unimodal distribution. The hematite-coated sample R2877 from Group 3 shows a behavior very similar to Group 2, but their log-normal fittings of T_2 distributions show an extra well-defined peak close to 3.3 X 10^{-2} s, which makes the T_2 time distributions clearly bimodal. Groups 2 samples and hematite-coated sample R2877 from Group 3 are characterized by a shift of shortest T_2 times towards values below 0.3 X 10^{-2} s. Finally, sample R2875 which has no visible macroporosity in thin sections, shows T_2 distribution covering only the shorter relaxation times (~ 0.9 X 10^{-2} s).

Table 8 – T_2 times of peaks which were obtained through the best log-normal fittings of 2MHz and 85MHZ on the distribution.

Samples	T_2 (s) Peak 1		T_2 (s) Peak 2		T_2 (s) Peak 3		T_2 (s) Peak 4	
Larmour frequency	2 (MHz)	85 (MHz)	2 (MHz)	85 (MHz)	2 (MHz)	85 (MHz)	2 (MHz)	85 (MHz)
R2852	0.166*	0.066*	0.079	0.022	0.014	0.007	0.002	0.001
R2856	0.240*	0.126*	0.098	0.063	0.020	0.016	0.008	0.001
R2860	0.288	0.151	0.120*	0.060*	0.014	0.012	-	0.001
R2863	0.436*	0.174	0.200	0.030*	0.083	0.001	0.012	-
R2855	0.112*	0.044*	0.050	0.014	0.022	0.001	0.008	-
R2853	0.316	0.151	0.047*	0.013*	0.007	0.001	-	-
R2854	0.355	0.091*	0.050*	0.015*	0.016	0.004	0.007	0.001
R2877	1.000	0.302	0.214*	0.089	0.063	0.008*	0.007*	-
R2875	0.282	0.199	0.009*	0.050	-	0.006*	-	-

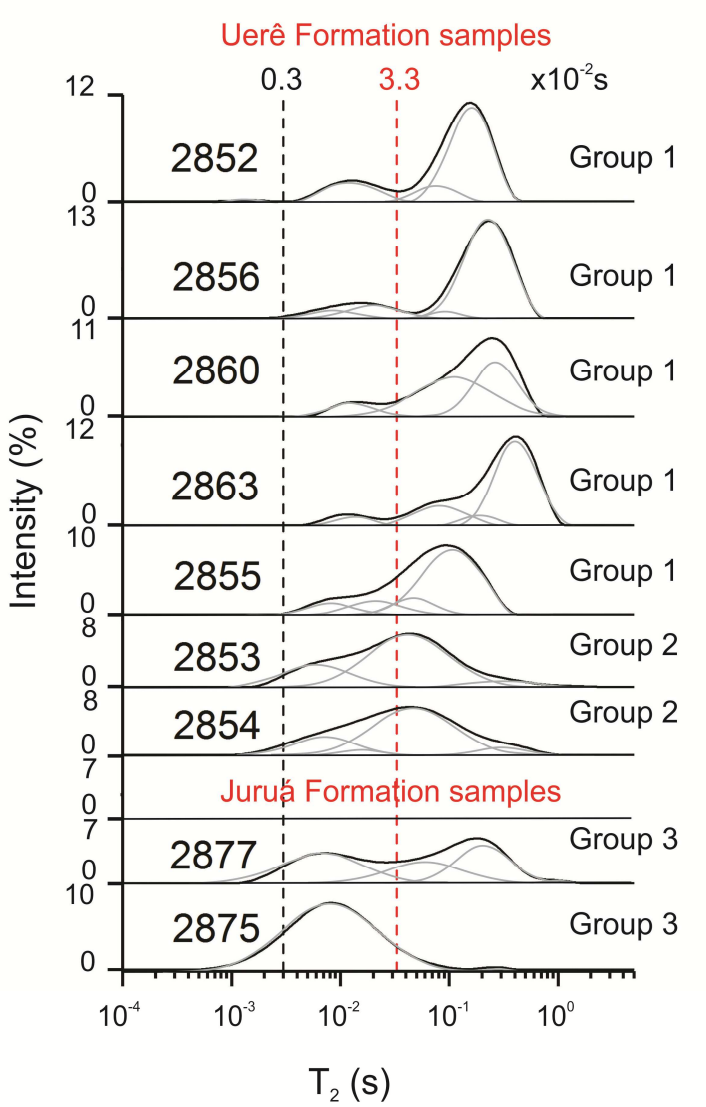

Figure 47 – T_2 times distributions from Group 1, Group 2 and Group 3 samples. See details in text.

The main factors which affect the relationship between the T_2 times and pore sizes in NMR experiments are the presence of paramagnetic impurities and the high magnetic susceptibility of minerals. The internal gradient induced by the difference of magnetic susceptibility between the pore surface and pore fluid is usually negligible in low external magnetic fields as those used in the 2 MHz experiment, but they may be occur in some cases (e.g. Rueslatten et al., 1998; Zhang et al., 2001; Keating and Knight, 2007, 2012). One way of qualitatively analyzing this behavior in high magnetic field (85 MHz) is to compare it with the low-field (2 MHz) T_2 distributions. The T_2 time distributions in the low and high magnetic fields of almost all analysed samples showed a shift between them. The exceptions are

samples R2875 and R2877, for which no displacement between the 2MHz and 85MHz curves are observed (Figure 48H andFigure 48I). This behavior is a bit surprising given the high magnetic susceptibility of these samples, but it is worth to note their different magnetic mineralogy comprising hematite as the main remanent magnetization carrier. Sample R2854 showed an almost unimodal T_2 time distribution in 2MHz, but some portion of the highest T_2 time peak is shifted towards shorter 10^{-2} s T_2 times in 85MHz (Figure 48).

Measuring the dependence of T_2 times when the echo times are increased allow us to qualitatively estimate the magnitude of the internal gradients (Kenyon, 1997; Dunn et al., 2002; Anand and Hirasaki, 2007; Keating and Knight, 2010). Here, when the echo spacing was increased from 200 to 500 us, we observed a displacement of T_2 values toward shorter times for representative samples from Group 1 (R2852) and Group 2 (R2853) (Figure 49A and Figure 49B). For hematite-coated sandstones from Group 3 we choose sample R2875 (Group 3; Figure 49C) as the representative sample due to its higher magnetic susceptibility and we can also see a shift in T_2 distribution and a change in the distribution curve. This result suggests that diffusion is an important contribution for changes in 2MHz T_2 NMR distributions of Group 3 samples.

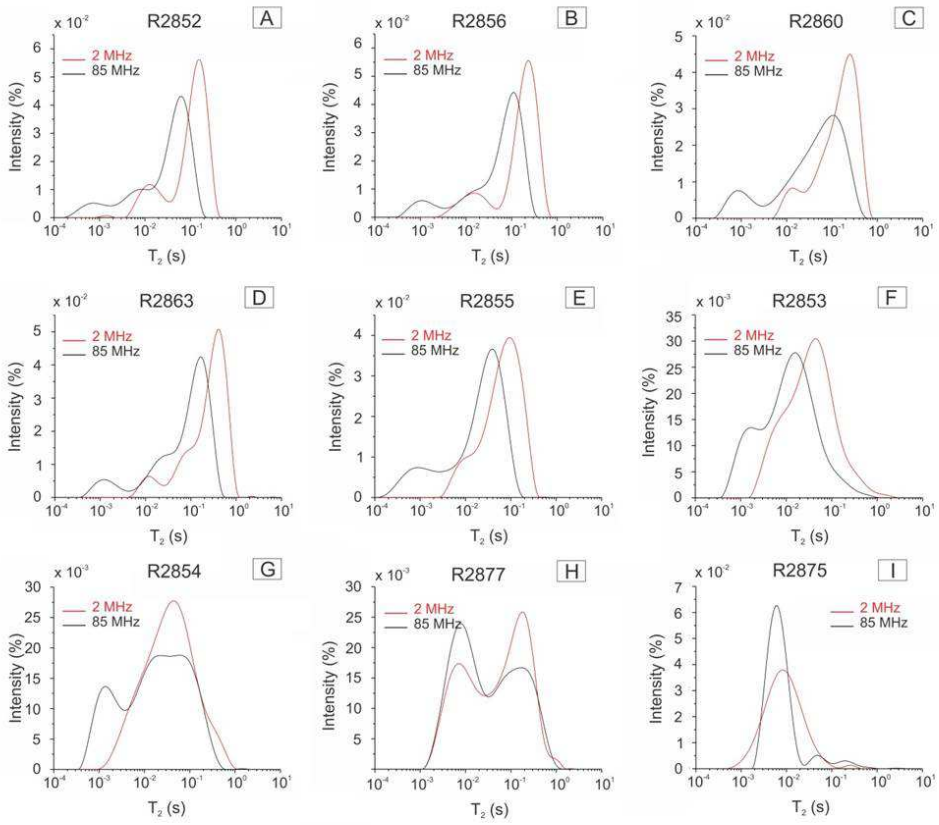

Figure 48– T_2 time distributions in low (2 MHz) and high (85 MHz) magnetic field, showing a slight displacement between these curves (exception is R2875 sample).

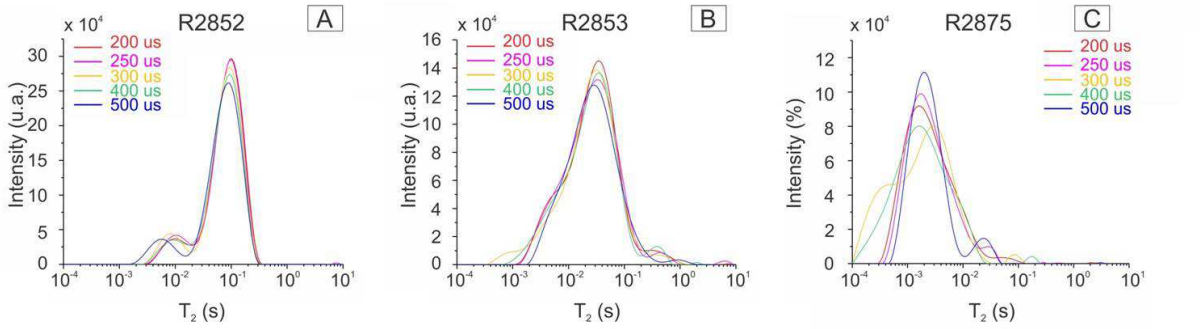

Figure 49 – The 2 MHz T_2 time distributions from R2852, R2853 and R2854 samples, using 200, 250, 300, 400 and 500 μs of echo times. Comparing the samples, we see the increase of disorder of curves from A to C due to increase of internal gradients.

5.3.5 **Discussion**

5.3.5.1 Petrography, petrophysical and NMR properties

The studied samples of the Uerê Formation sandstones had their porosity preserved due to presence of microcrystalline quartz coats (R2852, R2856, R2860, R2863, R2855, R2853 and R2854), while the samples from Juruá Formation (R2875 and R2877) are tight and coated by hematite. The petrography, porosity structure and geological context of the Uerê sandstones were previously studied by Lima and De Ros (2002), who presented a complete study on stratigraphy, petrography and petrophysics of the Uerê Formation.

All microquartz-coated samples have a good porosity, which varies from 15% to 23%. Although the R2875 and R2877 hematite-coated sandstones show a fair absolute porosity measured by the He porosimeter (10 and 19%, respectively), the porosity estimated through petrographic (0 and 9%, respectively) and micro-CT (10 and 9.5%, respectively) analysis are considerably lower, evidencing that hematite is ineffective in inhibiting quartz cementation, hence not preserving the primary macroporosity as shown by Heald and Larese (1974) for Potsdam and Juniata Sandstones, Saratoga region in New York (USA) and Pennsylvania (USA), respectively

As described before, the main macroporosity is due to preserved intergranular pores and, secondarily, to the dissolution of intragranular feldspar grains. The last one is very important in R2853, R2854 and R2860 samples, corresponding to 50%, 83% and 54% of porosity, respectively. When we compare the area of intermediate NMR peaks whose T_2 times vary from 5 to 42 X 10^{-2} s and the proportion of secondary feldspar, cement or lithic

porosities, the values are very similar for R2852, R2856, R2860 and R2855 samples, which correspond to almost all samples from Group 1. The R2860 sample, for example, presents 54% of the porosity caused by mineral dissolution and the area of 1.2 X 10^{-2} s NMR T_2 peak is 51% of the total of curve. Therefore, we interpret that peaks with T_2 > 3.3.X 10^{-2} s of Group 1 samples are due to free water (Allen et al., 1997) within primary intergranular pores and secondary pores formed by dissolution, which correspond to the >10^{-1} s and ~10^{-1} s peaks, respectively.

Samples of NMR Group 2 (R2853 and R2854), and the hematite-coated samples (R2877 and R2875) did not show a good correlation between the NMR area of intermediate peaks and the amount of porosity generated by dissolution of feldspar. We believe that T_2 times in these samples were displaced towards shorter times in the T_2 NMR distribution (Figure 47), therefore obscuring the dissolution contribution. We suggest that in these samples all the macroporosity is related to the T_2 time values above 2 X 10^{-2} s. This limit presents the intersection between the shortest peak in T_2 time distribution (~ 0.8 X 10^{-2} s) and the value of T_2 peak which is ≥ 3.3.X 10^{-2} s, which is defined as being the inferior limit for free water pores in Group 1 samples. Group 2 samples from Uerê sandstones present a family of pores with T_2 times around 0.3 s. Samples with IGV higher than 40% and moldic pores of Uerê Formation present displacive chalcedony, which form spherical pores around 10-20 μm (Lima and De Ros (2002), Since these moldic pores are generated by the complete dissolution of grains, they are usually larger than the intergranular pores. Hence, the longest peaks of T_2 distributions (~ 0.3s) are here attributed to the displacive chalcedony.

Some samples presented an important difference between the point-count petrographic estimation of porosity and that obtained with the Helium method. These samples were: R2860 and R2863 samples from Group 1, R2853 from group 2 and sample R2875 from Group 3. The porosity calculated through the micro-CT is closer to the He values (Table 6). Since the resolution of micro-CT is about 2 μm, we suggest that the 3D micro-CT analysis better covers the macroporosity than the limited 2D thin-section, being thus more representative.

In order to test the direct correlation between T_2 times and pore sizes for Group 1 samples, which presented the best qualitative correlation between macropores and relaxation times distribution, we first needed to ensure that the system is in fast diffusion regime, one of the three premises of NMR interpretation (Brownstein and Tarr, 1979). This occur when $\kappa = \rho a/D_0 << 1$, where ρ is surface relaxivity, *a* is the distance that a proton would need to travel to reach a paramagnetic site and D_0 is the diffusion coefficient of water (2300$\mu m^2/s$). Generally,

a is assumed to be $(S/V)^{-1}$, which for spheres packing is R/3, for cylinder is R/2 and for planar packing is R/1 (R= pore radius) (Dunn et al., 2002). Assuming that $\kappa << 1$ occurs when κ is at least 10 times lower, the condition for fast diffusion is obtained when $\kappa < 0.1$ (Ryu and Johnson, 2009). Table 9 showed that almost all samples of Group 1 are in fast diffusion regime (the R2855 is exception), hence the equation that correlates T_2 times and pore sizes through the relaxivity constant is valid (equation 50) (Table 9). However, the same is not valid for R2855 sample from Group 1, neither in samples from the other Groups (2 and 3) (Table 9).

Microporosity in the studied rocks may be related to multiple sources, including illite (filling the pores or coating the quartz host grain), microquartz (filling the pores or coating the quartz host grain), the mud matrix, besides the dissolution of minerals and cements. Therefore, their interpretation is not straighforward. Knowing that macropores vary from 10 to 90 μm, the micropores associated with illite flakes vary from 1 to 5 μm and those associated to microcrystalline quartz crystals vary from 623 nm to 2 μm, we expected that the NMR 2MHz T_2 peaks which could be correlated with these micropores would be separated by an order of magnitude for clays and two orders of magnitude (or more) for microcrystalline quartz coatings when compared to the macropores T_2 times (Figure 47). Unlike the results obtained by Jácomo et al. (2018) for chlorite coated sandstones from Recôncavo Basin, the Uerê sandstones did not show a clear relation between the area of T_2 peaks at $\sim 10^{-2}$ s and the concentration of associated micropore type (illite coatings or illite filling the pores). However, if we plot the area of these T_2 peaks versus the concentrations of diverse clays and carbonate cements (Appendix), we have a positive trend. Therefore, we can affirm that the $\sim 10^{-2}$ s T_2 peak is a sum of several sources of micropores and hence, under the fast diffusion regime of samples from Group 1, the surface relaxivity constants represent the whole measured volume (Table 9). Assuming fast diffusion for all samples, the estimative of pore sizes using equation 50 show that macropores due to dissolution vary from 8 to 17 μm (8 μm is the average of Group 1 samples), which is coherent with what we obtained with SEM images. However, we do not discard the possibility of a less secondary contribution of smectite-chlorite whose flakes are ~ 10 μm wide. The pore sizes correlated with $\sim 10^{-2}$ s T_2 peak vary from 0.5 to 5 μm (Group 1 has average of ~1μm), which is also similar with the clays and minor dissolution observed through SEM analysis. Since the sample R2855 from group 1 and all samples from Groups 2 and Juruá samples R2875, R2877 showed surface relaxivities in the intermediate diffusion regime, we can interpreted them as a minimum value.

Previous studies showed the micropore contribution associated with microquartz coatings in T_2 time distribution (e.g. Jácomo et al., 2019). Here, in contrast, the microquartz coatings do not seem to influence these distributions. We expected that ~0.8 X 10^{-2} s T_2 peak in NMR distributions were associated with the microquartz coatings, given the order of magnitude of associated pore sizes, which vary from 0.5 to 3 μm. However, the log-normal fittings for all samples (not only Group 1) show this peak is present even in Juruá samples. In this case, it shows a displacement to shorter T_2 times. So, we suggest that micropores associated to microquartz in Group 1 samples are amalgamated to those associated with the porosity caused by clays bound water in ~0.8 X 10^{-2} s T_2 times.

In order to analyze the effects of illite coatings, the area of T_2 times peaks associated with clay micropores (T_2 ~10^{-2} s) were correlated with the amounts of illite coatings. Samples which present illite coatings (R2852, R2856 and R2855) did not show any correlation with micropores or macropores. The diffusion coupling in these clays within the macropores, was assessed using the parameters suggested by Grunewald and Knight (2011) who used hematite coated sandstones for analyzing the relaxation times in sediments with bimodal mineralogy.

The two parameters used by these authors are a and l_D, where l_D can be defined through the Einstein´s equation as being the distance in which the spin diffuses in the pore space before relaxing:

$$l\mathrm{D} = \sqrt{6DT} \tag{52}$$

where D is diffusion coefficient of ^{1}H in water and T is the relaxation time. If the diffusion $l_D > a$, there is a strong coupling between micro and macropores; if the diffusion $l_D < a$, there is a weak coupling. Table 9 shows that $l_D > a$ for all samples, defining an strong coupling between the two types of pores.

Table 9 – The values of κ, ρ, l_D and a for all studied samples. * assuming a fast diffusion regime.

Sample	Group	κ	ρ2*	χ (10^{-6} SI)	l_D	a (R/3)
R2852	1	0.0993	37.8	22.5	47.0	6.04
R2856	1	0.0645	25.4	19.9	56.3	5.84
R2860	1	0.0478	19.8	15.2	62.2	5.55
R2863	1	0.0375	14.2	9.94	77.0	6.09

R2855	1	0.1443	54.9	17	39.0	6.04
R2853	2	0.2817	118.7	45.5	25.2	5.46
R2854	2	0.2633	110.1	47.9	26.3	5.50
R2877	3	0.1176	35.9	49.6	53.8	7.54
R2875	3	0.7433	443.3	123.6	10.9	3.86

5.3.5.2 Magnetic and NMR properties

All natural sediments carry certain amounts of magnetic particles. Their properties change according with their composition, grain size and geological processes (transport, deposition and diagenetic reactions) (Maxbauer et al., 2016). Previous studies (e.g., Bloembergen et al., 1948; Foley et al., 1996; Bryar et al., 2000, Bryar and Knight, 2002, Keating and Knight, 2007, 2010, 2012; Keating et al., 2008; Grunewald and Knight, 2009 and 2011) showed how minerals bearing Fe^{3+} and Fe^{2+} in their composition can affect the NMR data, with the increase of paramagnetic sites affecting the surface relaxivities and increasing the decay rate. This behavior depends on the amount and the form in which iron occurs in the sample. If we compare the low amounts of magnetite (0.65%) with the higher amounts of other ferrous minerals (1%) (hematite, goetite, lepidocrocite and ferrihydrite), magnetite is by far the most important contribution to the surface relaxation and diffusion relaxation (this one being affected only by magnetite). When Bryar and Knight (2002) and Keating and Knight (2010) included paramagnetic Fe^{+2} minerals siderite and pyrite in their experiments, they concluded that they contribute differently to surface T_2 relaxation; siderite presenting an important contribution while pyrite contributing only when in high concentration.

Here, the petrography showed some iron minerals which can disturb the NMR signal such as hematite, Fe calcite (siderite), Fe dolomite (anquerite), besides the possible contents of Fe impurities in illite, pseudomatrix and lithic fragments. In addition to the microscopic observations, the magnetic measurements (Figure 44, Figure 45 and Figure 46) showed important ferrimagnetic and paramagnetic contributions which were not identified by thin section inspection. The microcrystalline quartz coated sandstones from Group 1 are mainly composed of diamagnetic quartz but present some amounts of magnetite, yielding a bulk magnetic susceptibility of 10 to 22.5 X 10^{-6} SI (Table 6). Samples R2853 and R2854 from Group 2 have, in addition to magnetite, minor amounts of hematite and also paramagnetic contributions. Samples R2877 and R2875 from Group 3 are hematite-coated sandstones and this mineral is the main iron-bearing phase responsible for the bulk magnetic susceptibility (Table 6).

The presence of paramagnetic and ferromagnetic minerals, even in low concentration (<1 %) are important in NMR data. In Figure 50 we plotted the magnetic susceptibility *versus* the magnetic moment of the samples after magnetization at 1T (Figure 50). The graph shows a linear trend formed by Group 1 and hematite-coated samples, suggesting the same source of magnetic effects for these groups, while the paramagnetic minerals, which are mainly related to Fe-illite, are the main contribution for Group 2.

When we compare the magnetic susceptibility values with the T_2 time distributions (Figure 51), we observe that the larger variations in T_2 time are associated with the samples with the higher magnetic susceptibilities. Besides that, comparing χ and T_2 with surface relaxivity, we conclude that this is a dominant mechanism for relaxation for all samples (Table 9) and the diffusion relaxation has an important contribution for T_2 relaxation on samples from Groups 3 only (Figure 49) since they present an important displacement for shorter T_2 times as T_2 echo time increase. This is evidenced when we compare R2852 and R2877 samples, which have similar pore sizes and surface relaxivities and different magnetic susceptibility values (Table 9). These data also suggest that low amounts of magnetite affect the surface relaxivity values, but not the diffusion relaxation. Unlike previous studies (Keating and Knight, 2007; 2012), we show that in samples with higher concentration of hematite crystals and hematite coatings, hematite affects significantly the diffusion relaxation times.

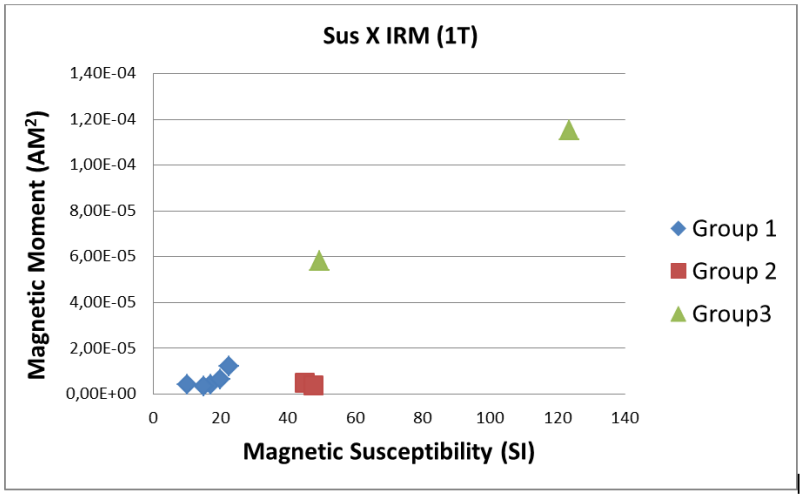

Figure 50 – Magnetic susceptibility versus magnetic moments of Groups of sample, showing a positive linear trend formed with Group 1 and Group 3 samples.

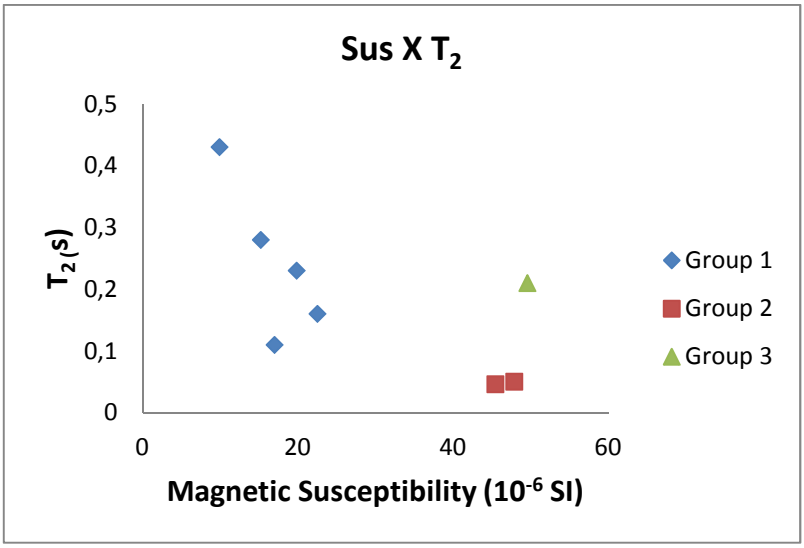

Figure 51 – Magnetic susceptibility versus T_2 times of Groups of samples. The Group 1 shows that a small difference in magnetic susceptibility values creates an important difference in T_2 relaxation times.

5.3.6 **Conclusions**

The porous sandstones from the Uerê Formation and tight sandstones from the Juruá Formation present different nuclear magnetic resonance signals, according to their texture, composition, petrophysics and magnetic properties. Group 1 samples are mainly diamagnetic samples and consist of microquartz-coated sandstones. Even presenting low contents of magnetite, they have the longest T_2 times in 2MHZ distributions. Group 2 samples are characterized by displacements towards shorter T_2 times and present almost unimodal behavior in NMR distribution. They consist of subarkose sandstones whose magnetic minerals comprise mainly paramagnetic grains. The tight samples correspond to hematite grain-coated sandstones. These samples also present a displacement towards shorter T_2 times. The presence of paramagnetic particles seems to be the main source for T_2 times displacements in Group 2 and surface relaxivity, while for hematite-coated samples the high amount of hematite grains contribute for the diffusion relaxivity which is evidenced also by the decrease of T_2 with the increase of T_2 echo time.

The high concentration of ferromagnetic and paramagnetic minerals in sandstones remains a major challenge for studies of NMR in siliciclastic deposits. This is particularly critical in reservoirs with anomalous porosity where the mechanism of porosity preservation involves Fe-bearing mineral coatings, these phases occupying the pore surface. Displacement of T_2 values caused by this geological configuration produce an underestimation of pore sizes, porosity values and obliterate the pore distribution relationships. To improve the

interpretation of NMR well-log data, it is important to perform experiments increasing inter-echo times during NMR data acquisition and fully characterize the magnetic mineralogy of the rocks.

APPENDIX

Table 1- Petrophysics and mineralogy of samples.

Groups	**1**					**2**		**3**	
Petrophysics	**R2852**	**R2855**	**R2856**	**R2860**	**R2863**	**R2853**	**R2854**	**R2877**	**R2875**
He Porosity (%)	20	21	22	16	23	15	15.9	19	10
Permeability (mD)	152	12	70	3	12	3	10	11	0
Density	2.62	2.66	2.65	2.58	2.65	2.63	2.72	2.69	2.65
Magnetic Susceptibility	19.9	20.6	22.3	16.0	22.9	15.1	15.9	18.8	10.3
Magnetism	Dia + Ferro	Dia + Ferro	Dia + Ferro	Dia + Ferro	-	Para + Ferro	Para + Ferro	Para + Ferro	Para + Ferro
IGV	29,7	30,65	42,0	21,67	21,33	42,67	45,1	24,0	31,0
Macroporosity	**17**	**11**	**20**	**4**	**5**	**2**	**11**	**9**	**0**
Minerals									
Primary	**59**	**44**	**46**	**53**	**55**	**36**	**39**	**50**	**52**
Detrital quartz	53	~41	42	~50	~51	33	36	~42	37
Detrital feldspar	4	~3	~4	~3	~3	~2	~3	~3	~3
Rock frag.	~1	0	0	0	~1	0	0	~2	~2
Fine crystals lithics	~1	0	0	0	0	~1	0	~3	10
Diagenetic	**22**	**43**	**33**	**42**	**38**	**58**	**48**	**40**	**45**
Quartz overgrowth and outgrowth	~1	3	1	10	~6	12	~1	~14	~7
Quartz filling pores	0	~2	0	0	0	1	0	0	0
Chalcedony rims	0	0	0	0	0	~14	0	0	0
Chalcedony	0	0	0	0	0	13	0	0	0
Chalcedony displacive	0	0	0	0	0	~2	~34	0	0
Microquartz coatings	8	~1	11	~1	~1	~1	4	0	0
Microquartz	0	0	8	~1	0	0	0	0	0
Diagenetic	0	~11	0	8	~10	0	0	0	0

silica									
Silica coatings		~8	0	4	~5	0	0	0	0
Clay coatings (Illite)	~3	~1	~2	0	0	0	0	0	0
Clay coatings (Smectite)	0	0	0	0	0	0	0	0	~1
Hematite	0	0	0	0	0	0	0	4	~7
Hematite coatings	0	0	0	0	0	0	0	10	16
Fe calcite	0	0	0	0	0	0	0	~1	0
Anhydrite	~3	~1	0	~1	0	0	~1	~1	0
Dolomite	~2	~1	~1	0	0	0	0	0	0
Fe Dolomite (anquerite)	0	~1	0	~1	~3	~4	0	~2	0
Siderite	0	0	0	0	0	~1	0	0	0
Illite	~1	3	~6	~1	~1	~1	~3	~1	~1
Pyrite	0	1.6	0	<1	1	1.5	0	0	0
Albite	~4	~9	~4	11	~9	~6	~4	~6	~13
Mud Pseudomatrix	0	0	0	0	0	~1	0	~1	0
Accessory	**2**	**~2**	**~1**	**~1**	**~2**	**3**	2	**~1**	**3**
Mica	~1	~1	0	0	~1	~2	~1	0	~2
Titanite + Turmaline + Zircon	1	~1	~1	~1	~1	~1	~1	~1	~1
Hydrocarbon	**0**	0	0	0	0	**~1**	0	0	0
Classification									

6 Synthesis and Conclusions

In this work the porosity structure of sandstones bearing anomalous porosity was investigated. These rocks have micropores associated with coatings which have different compositions, producing different NMR answers. Here, sandstones with microquartz (Fontainebleau Formation, Paris Basin), chlorite (Água Grande Formation, Recôncavo Basin), microquartz with illite (Uerê Formation, Solimões Basin) and hematite coatings (Juruá Formation, Solimões Basin) were investigated and the main following implications of this thesis are:

6.1 T_2 NMR distributions

The low magnetic field NMR distributions of coated sandstones from Fontainebleau, Água Grande, Uerê and Juruá Formation are characterized by an important displacement towards short T_2 times in distributions of samples with high amounts of clay or microquartz coatings even the sample showing similar pore sizes.

The Fontainebleau samples are almost completely composed of diamagnetic silica (SiO_2). The studied samples were divided into two groups with small and high amounts of microquartz coatings (Groups 1 and 2, respectively). Hysteresis loop of FB-L2B01 and FB-L3B01 samples from Group 1 and FB-155 sample from Group 2 showed a small ferrimagnetic contribution (low-coercivity magnetite), but these samples present small magnetic susceptibilities (FB-155 sample has negative susceptibility), evidencing the very small or negligible ferromagnetic contribution. μCT analyses showed that samples FB-155, FB-217 and FB-10 have similar pore size distributions. We expected the T_2 NMR distributions of these samples to be similar, however the FB-155 showed an important displacement of T_2 times towards shorter times. Since almost all the samples are in fast diffusion regime and all pore surfaces have the same composition (and very low magnetic susceptibility), the S/V ratio and diffusion coupling were considered the main factors responsible for this displacement. The relaxivity values obtained for Fontainebleau sandstones range from 1 μm/s to 8 μm/s.

The Água Grande samples were also divided into two groups according the amount of chlorite coatings on the quartz host grains. The NMR 2 MHz T_2 distributions for all samples can be interpreted in terms of three peaks. Thin sections and SEM images allowed us to interpret the longest T_2 times (>0.1 s) as due to intergranular macropores, while the intermediate T_2 peak in the distributions was interpreted as due to mineral dissolution (mainly

feldspar). We observed an important displacement towards shorter times in 2 MHz NMR T_2 distributions of samples with high amounts chlorite coatings (Group 2). The chlorite coatings contain Fe, which can enhance the relaxivity. However, even with the presence of paramagnetic chlorite, the considerable differences of magnetic susceptibility between the surface and the fluid apparently do not affect the diffusion relaxation since the increase of time between the echoes do not change the T_2 value in the samples. The amount of chlorite covering quartz grains was estimated by the EDS mapping of %Fe in the samples. There is a clear correlation between the %Fe on the samples and the NMR Gaussian fittings of 2 MHz T_2 distribution curves for peaks at ~0.02 s T_2 times. The relaxitivity in these rocks is directly correlated to the area of the ~0.02 s T_2 peak in NMR distribution, and to the %Fe covering the quartz grains. It is also correlated to the difference between the porosities estimated by petrography and Helium methods, which is usually interpreted as being related to amount of microporosity. Because of that, we first interpreted the diffusive coupling between macro and micropores as weak. However, the area of the NMR T_2 distribution curves is not proportional to the porosity measured by conventional methods. Therefore, some diffusive coupling must operate in the system bringing the T_2 peaks in NMR distributions towards shorter times. Some contribution of relaxitivity due to the presence of chlorite is also likely. We described this effect by using the model proposed by Kenyon (1997) in which the geometry of clay flakes along the pores is considered. The relaxivities from Group 1 samples, which are in fast diffusion regime, vary from 32μm/s to 43μm/s. The samples from Group 2, which are in intermediate diffusion regime, have effective relaxivities about 15μm/s and the relaxivity of micropore is ~100 μm/s.

The Uerê Formation samples were classified into three groups based on petrographic observations, the magnetic susceptibility and the type of iron-bearing minerals in the coatings. Group 1 consists of subarkoses with variable amounts of coatings of microcrystalline quartz or undifferentiated silica on the quartz grains. Group 2 also contain microquartz coatings but its mineral matrix contains iron-bearing minerals such as Fe-dolomite, siderite and pyrite, besides Fe-illite. These samples contain the highest amounts of pore-filling displacive chalcedony and high IGV (43% and 45%). The samples from Juruá Formation form Group 3, which consists of hematite-coated sandstones cemented by quartz overgrowths, albite, hematite and pore-filling illite. The T_2 relaxation time distributions for all studied samples showed three to four peaks. Macroporosity for these samples is indicated by a peak above 10^{-1} s in T_2 time distributions, whereas the intermediate peaks (0.1-0.01 s) are related to mineral

dissolution. In Group 1 samples the shortest T_2 times do not present a shift towards values below of 0.3 X 10^{-2} s. In contrast, Groups 2 and 3 are characterized by a shift in the highest intensity peak towards shorter times (~5 X 10^{-2} s), reducing the differences between the peaks and making it resemble a unimodal distribution (Group 2) or showing an extra peak close to 3.3 X 10^{-2} s, which makes the T_2 time distributions clearly bimodal. The exception is the R2875 sample, which has no visible macroporosity in the petrographic analysis, showing only one peak with the shortest relaxation times. The relaxivity values from Group 1, which is in fast diffusion regime, vary from 14 μm/s to 37 μm/s, while the relaxivity values from intermediate diffusion regime samples from Group 2 and 3 vary from 35 μm/s to 118 μm/s. The relaxivity from 2875 sample is 443 μm/s.

6.2 NMR diffusion coupling

NMR relaxation measurements are usually interpreted by assuming a direct correlation between T_2 distribution and pore sizes. But this is valid only if three premises are demonstrated: a) the pores have to be effectively isolated, such that molecules on each pore relax independently of the others; b) the system is in fast-diffusion regime; c) the surface relaxivity is uniform across the entire surface of the pore space (Browstein and Tarr, 1979). However, the first condition is not simple to meet in natural geologic rocks, whose pores are typically connected to each other, allowing diffusion of molecules between pores and therefore affecting the relaxation (Grunewald and Knight, 2009).

In order to study the diffusion coupling, we used the T_2-T_2 Exchange technique which allows observing fluid molecules migration among different pores (Washburn and Callaghan, 2006). Since T_2-T_2 Exchange experiments are very time consuming, a faster version of this experiment was used (T_2F-TREx) following the procedure of D'Eurydice et al. (2016).

In Fontainebleau samples, 85 MHz T_2-T_2 exchange experiments showed that T_2 distribution displacements towards shorter times is not caused by diffusion coupling, the cause being probably related to changes in S/V at the flat-shaped internal layers of the microquartz coatings. The T_2-T_2 exchange experiments also allowed to identify the micropores associated to microquartz crystals through the exchange rates between macropores A, which have longest ~1.7 and 0.36 s T_2 times for Group 1 and 2, respectively, pores B (~0.3 and 0.05 s T_2 for group 1 and 2, respectively) and pores C (~0.01s T_2). The exchange between A and C pores is higher than between A and B, while the exchange rate between B and C is negligible. We concluded that peak C is due to micropores associated to microcrystalline

quartz coatings and the peak B is probably also due to microcrystalline quartz coatings, however with more planar shape.

Unfortunately, the T_2-T_2 exchange analysis was not possible because of the high values of magnetic susceptibility of samples from Água Grande, Uerê and Juruá Formations. However, due to reasons presented above, besides the fact that the size of the channel, we suggest that intermediate diffusive coupling condition is present in the Fm. Água Grande.

6.3 Magnetic minerals

The internal gradients due to the paramagnetic or ferromagnetic minerals are known to shift T_2 values to shorter relaxation times (Kleinberg et al., 1994; LaTorraca et al., 1995; Rueslatten et al., 1998; Zhang et al., 2002; Keating and Knight, 2007, 2012).

The Fontainebleau sandstones are almost completely composed of silica as evidenced by petrographic and SEM analysis. In spite of a minor amount of ferromagnetic minerals detected in some samples (FB-L2B01, FB-L3B01 and FB-155) through hysteresis measurements, these Fe-rich impurities seem to occur as inclusions in quartz grains and do not occupy the walls of the pores. Therefore they do not affect the surface relaxivity.

The Água Grande Formation samples are composed mainly of paramagnetic and very small amounts of ferromagnetic minerals (magnetite) for almost all samples. The exception is the 7570 sample which is composed mainly of diagmagnetic minerals (quartz, feldspar) and very small amounts of ferromagnetic minerals (probably magnetite). Accordingly, the susceptibility varies from 19 X 10^{-6} to 46 X 10^{-6} SI in reservoir samples, the magnetic susceptibility for 7570 sample is 8 X 10^{-6} SI. Although the samples present important magnetic susceptibility values, they are not high enough to produce a displacement of T_2 towards shorter times with the increase of echo times, indicating the absence of diffusion mechanism in relaxation.

The best units to assess the effects of the magnetic minerals on the shift of T_2 values to shorter relaxation times is the Uerê and Juruá formations, which present a complex mineralogy including paramagnetic and ferrimagnetic impurities. The magnetic susceptibility in Group 1 samples (Uerê Formation) range from ~10 to 22 X 10^{-6} SI, while in Group 2 samples range from 45 and 48 X 10^{-6} SI. The Juruá Formation samples (Group 3) have the highest values: ~50 and 123 X 10^{-6} SI for the two samples. These samples are characterized

by the presence of hematite coatings. The high amount of Fe-illite and other paramagnetic minerals in Group 2 samples and hematite in Group 3 samples produces similar displacements of the longest T_2 times towards shorter times. This effect is caused by relaxitivity in Group 2 and diffusion in Group 3. The relaxivity is the only contribution of relaxation in Group 1, and the main contribution to Group 2 (with a small contribution of diffusion), while the diffusion relaxation is predominant in Group 3 due to the high amounts of hematite in the grain's surface.

Although the bulk magnetic susceptibility values of Recôncavo Basin samples and Solimões are similar, the amounts and types of magnetic minerals are different and their distribution, the samples from Solimões presenting a higher content of antiferromagnetic grains (hematite) along the pore walls. The Solimões samples present a shift in T_2 distributions with the increase of echo times, indicating a diffusion mechanism in the relaxation. This effect is not observed in the Recôncavo Basin samples. Therefore, the type of magnetic minerals (e.g., Fe-bearing clays and hematite) and their distribution must be taken into account when interpreting the T_2 relaxation distributions and the T_2 to echo-time correlation in porous rocks.

6.4 Final considerations

The analysis of anomalous porosity sandstones trough NMR is not a simple task since multiple reasons may affect the NMR signal in natural sandstones. Here, several analytical techniques were used to support the interpretation of NMR data. Combining NMR results with petrophysical, petrographic and magnetic data, it was possible to calculate the relaxivity of all samples. Relaxitivity from Fontainebleau varies from 1 to 8 μm/s. Água Grande relaxitivity varies from 32 to 43 μm/s for macropores. It is 100 μm/s for micropore in weak diffusive coupling and ~15 μm/s for intermediate diffusive coupling (using the model of Kenyon, 1997). In Uerê sandstones relaxitivity varies from 14 to 55 μm/s. If we assume the fast diffusion for Groups 2 and 3 (high magnetic susceptibility) of Uerê and Juruá sandstones, the relaxivity varies from 36 to 118 μm/s.

The high concentration of ferromagnetic and paramagnetic materials in sandstones remains a major challenge for studies of NMR in siliciclastic deposits. This is particularly critical in reservoirs with anomalous porosity when the mechanism of porosity preservation involves Fe-bearing coatings (e.g., Água Grande and Uerê formations). This is because the presence of paramagnetic and ferromagnetic minerals, particularly when they occupy the pore

surface, causes a displacement of T_2 values in NMR distribution towards shorter times underestimating the pore size and porosity values. To reduce the ambiguity in interpretation, it is important to perform experiments increasing the inter-echoes times during the well log NMR data acquisition, besides a better characterization of the magnetic mineralogy of the rocks.

7 References

Aase, N. E., Bjorkum, P. A., & Nadeau, P. H. (1996). The effect of grain-coating microquartz on preservation of reservoir porosity. *AAPG bulletin, 80(10), 1654-1673*.

Aase, N. E., & Walderhaug, O. (2005). The effect of hydrocarbons on quartz cementation: diagenesis in the Upper Jurassic sandstones of the Miller Field, North Sea, revisited. *Petroleum Geoscience, 11(3), 215-223*.

Agut, R., Levallois, B., & Klopf, W. (2000). January. Integrating core measurements and NMR logs in complex lithology. *In: SPE Annual Technical Conference and Exhibition. Society of Petroleum Engineers.*

Ajdukiewicz, J. M., Nicholson, P. H. & Esch, W. L. (2010). Prediction of deep reservoir quality using early diagenetic process models in the Jurassic Norphlet Formation, Gulf of Mexico. *AAPG Bulletin, 94(8): p. 1189-1227*.

Ajdukiewicz, J. M., & Larese, R. E. (2012). How clay grain coats inhibit quartz cement and preserve porosity in deeply buried sandstones: Observations and experiments Clay-Coat Experiments. *AAPG bulletin, 96(11), 2091-2119*.

Allen, D., Crary, S., & Freedman, B. (1998). How to use borehole nuclear magnetic resonance. *Oilfield Review, 3(45), 34-57.*

Al-Ramadan, K., S. Morad, J. N. Proust, & I. S. Al-Aasm. (2005). Distribution of diagenetic alterations in siliciclastic shoreface deposits within a sequence stratigraphic framework: Evidence from the Upper Jurassic, Boulonnais, NW France. *In: Morad, S., Al-Ramadan, K., Ketzer, J. M., & De Ros, L. F. 2010. The impact of diagenesis on the heterogeneity of sandstone reservoirs: A review of the role of depositional facies and sequence stratigraphy. AAPG bulletin, 94(8), 1267-1309.*

Al Saadi, F., Wolf K., & Kruijsdijk C. V. (2017). Characterization of Fontainebleau Sandstone: Quartz Overgrowth and its Impact on Pore-Throat Framework. *J Pet Environ Biotechnol, v. 7, n. 328, p. 2*.

Anand, V., & Hirasaki, G. J. (2005, January). Diffusional coupling between micro and macroporosity for NMR relaxation in sandstones and carbonates. *In: SPWLA 46th Annual Logging Symposium. Society of Petrophysicists and Well-Log Analysts.*

Anand, V., & Hirasaki, G. J. (2007). Paramagnetic relaxation in sandstones: Distinguishing T_1 and T_2 dependence on surface relaxation, internal gradients and dependence on echo spacing. *In: SPWLA 48th Annual Logging Symposium. Society of Petrophysicists and Well-Log Analysts*

Andersen, M. A., Duncan, B., & McLin, R. (2013). Core truth in formation evaluation. *Oilfield Review, 25(2), 16-25.*

Andreeta M.C. (2017). Topological analysis of reservoir rocks and acidification processes using complex networks methods. *DoctorateThesis. Instituto de Física de São Carlos. Universidade de São Paulo. 121p.*

Anjos, S. M.D. , De Ros, L. F., de Souza, R. S., de Assis Silva, C. M., & Sombra, C. L. (2000). Depositional and diagenetic controls on the reservoir quality of Lower Cretaceous Pendencia sandstones, Potiguar rift basin, Brazil. *AAPG bulletin, 84(11), 1719-1742.*

Anjos, S. M. C., De Ros, L. F., Silva, C. M. A., Worden, R. H., & Morad, S. (2003). Chlorite authigenesis and porosity preservation in the Upper Cretaceous marine sandstones of the

Santos Basin, offshore eastern Brazil. *In: Clay Mineral Cements in Sandstones (Vol. 34, pp. 283-308). International Association of Sedimentologists Special Publication.*

Anovitz, L. M., & Cole, D. R. (2015). Characterization and analysis of porosity and pore structures. *Reviews in Mineralogy and geochemistry, 80(1), 61-164*.

ANP. 2016. *Site: http://www.anp.gov.br/wwwanp/images/publicacoes/boletins-anp/boletim_de_outubro 2016.pdf. Acess: 23/12/2016.*

Appel, M. (2004). Nuclear magnetic resonance and formation porosity. *Petrophysics, 45(03).*

Arns, C.H. (2004). A comparision of pore size distributions derived by NMR and X-ray-CT techniques. *Physica A: Statistical Mechanics and its Applications, v.339, n.1-2, p. 159-165*.

Azevedo E. (2017). Mathematical and Physical Basis for NMR – *NMR School – AUREMN. São Carlos. Class Notes*.

Barclay, S. A., & Worden, R. H. (2000). Effects of reservoir wettability on quartz cementation in oil fields. *In: Quartz cementation in sandstones, 29, 103-117.*

Beaufort, D., Baronnet, A., Lanson, B., & Meunier, A. (1997). Corrensite: A single phase or a mixed-layer phyllosilicate in the saponite-to-chlorite conversion series? A case study of Sancerre-Couy deep drill hole (France). *American Mineralogist, 82(1-2), 109-124*.

Behroozmand, A. A., Keating, K., & Auken, E. (2015). A review of the principles and applications of the NMR technique for near-surface characterization. *Surveys in Geophysics, 36(1), 27-85*.

Berger, A., Gier, S., & Krois, P. (2009). Porosity-preserving chlorite cements in shallow-marine volcaniclastic sandstones: Evidence from Cretaceous sandstones of the Sawan gas field, Pakistan. *AAPG bulletin, 93(5), 595-615*.

Bernabé, Y., & Maineult A. (2015). Physics of porous media: fluid flow through porous media. P. 19-41.

Billault, V., Beaufort, D., Baronet, A. & Lacharpagne, J.-C. (2003). A nanopetrographic and textural study of grain- coating chlorites in sandstone reservoirs. *Clay Minerals, 38: p. 315–328*.

Bjorkum, P. A., & Nadeau, P. H. (1998). Temperature controlled porosity/permeability reduction, fluid migration, and petroleum exploration in sedimentary basins. *The APPEA Journal, 38(1), 453-465*.

Bloch, S. (1991). Empirical prediction of porosity and permeability in sandstones. *AAPG Bulletin, v. 75, p. 1145–1160.*

Bloch, S., Lander, R. H., & Bonnell, L. (2002). Anomalously high porosity and permeability in deeply buried sandstone reservoirs: Origin and predictability. *AAPG bulletin, 86*(2*), 301-328*.

Boles, J.R. & Franks, S.G. (1979) Clay diagenesis in Wilcox sandstones of southwest Texas: implications of smectite diagenesis on sandstone cementation.In: Worden, R.H., & Morad, S. 2003. Clay Minerals in sandstones: Controls on Formation Distribution and Evolution. *In: Clay Mineral Cements in Sandstones, International Association of Sedimentologists Special Publication **34**, Blackwell Publishing, 3–41. ISBN: 1-40510-587-0. DOI: 10.1002/9781444304336.ch1*.

Bonagamba T.J., (2005). A Ressonância Magnética Nuclear no âmbito da história da Física Moderna e suas atuais aplicações. *INPE.*

Borgia, G.C., Brown R.J.S., & Fantazzini P. (1998). Uniform-penalty inversion of multiexponential decay data. *Journal of Magnetic Resonance, v.132, n.1, p. 65-77*.

Browstein K.R., & Tarr C.E. (1979). Importance of classical diffusion in NMR studies of water in biological cells. *Physical Review A, 19 (6), 2446-2453*.

Bryar, T., Daughney, C., & Knight, R. (2000). Effects of paramagnetic iron (III) species on nuclear magnetic resonance relaxation of saturated sands. Journal of Magnetic Resonance, 142, 74-85.

Bryar, T. R., & Knight, R. J. (2002). Sensitivity of nuclear magnetic resonance relaxation measurements to changing soil redox conditions. Geophysical Research Letters, 29(24). doi:10.1029/2002GL016043.

Bukar, M. (2013). Does oil emplacement stop diagenesis and quartz cementation in deeply buried sandstone reservoirs? *(Doctoral dissertation, University of Liverpool).*

Butler, R. F. (2004). Paleomagnetism: Magnetic domains to geologic terranes. *Electronic edition, 24*.

Cagatay, M.N., Saner, S., AlSaiyed, I. & Carrigan, W.J. (1996). Diagenesis of the Safaniya Sandstone Member (mid-Cretaceous) in Saudi Arabia. *Sedimentary Geology, 105, 221–239.*

Cantrell, D. L., & Hagerty, R. M. (1999). Microporosity in arab formation carbonates, Saudi Arabia. *GeoArabia, 4(2), 129-154*.

Carneiro, Giovanna da Fraga. (2012). Estudo de emulsões de petróleos brasileiros por Ressonância Magnética Nuclear (RMN) de Baixo Campo Bidimensional. (*Dissertação de Mestrado em Química, Universidade Federal do Espírito Santo*).

Cao, Z., Liu, G., Meng, W., Wang, P., & Yang, C. (2018). Origin of different chlorite occurrences and their effects on tight clastic reservoir porosity. *Journal of Petroleum Science and Engineering, 160, 384-392*.

Chang, H.K., MacKenzie, F.T. & Schoonmaker, J. (1986). Comparision between the diagenesis of dioctahedral and triochedral smectite, Brazilian offshore basins. *In: McKinley, J. M., Worden, R. H., Ruffell, A. H., & Morad, S. 2003. Smectite in sandstones: a review of the controls on occurrence and behaviour during diagenesis. In: Clay Mineral Cements in Sandstones (Vol. 34, pp. 109-128). International Association of Sedimentologists Special Publication.*

Chang, J., & Yortsos, Y. C. (1994). Lamination during silica diagenesis; effects of clay content and Ostwald ripening. *American Journal of Science, 294(2), 137-172*.

Choquette, P. W., & Pray, L. C. (1970). Geologic nomenclature and classification of porosity in sedimentary carbonates. *AAPG bulletin, 54(2), 207-250*.

Cnudde, V., & Boone, M. N. (2013). High-resolution X-ray computed tomography in geosciences: A review of the current technology and applications. *Earth-Science Reviews, 123, 1-17*.

Coates, G.R., Xiao L., Prammer & M.G. (1999). NMR Logging: Principles and Aplications, *Houston: Halliburton Energy Services*.

Cooper, M.R., Evans J., Flint S.S., Hogg A.J.C., & Hunter R.H. (2000). Quantification of detrital, authigenic and porosity components of the Fontainebleau sandstone: a comparison of conventional optical and combined scanning electron microscope-based methods of modal analyses. *Quartz cementation in sandstones, p. 89-101*.

Cortez M.M.M. (1996). Análise geoestatística da geometria externa dos reservatórios fluvial e eólico da Formação Água Grande, área-central da Bacia do Recôncavo. Dissertação de mestrado, *UNICAMP*. *1996.118p.*

Curtis, C.D., Hughes, C.R., Whiteman, J.A. & Whittle, C.K. (1985). Compositional variation within some sedimentary chlorites and some comments on their origin. *Mineral. Mag., 49, 375–386*.

Davies, S., & Packer K.J. (1990). Pore-size distributions from nuclear magnetic resonance spin-lattice relaxation measurements of fluid-saturated porous solids:Theory and simulation, *Journal of Applied Physics, v. 67, n. 6, p. 3163-3170.*

Davies, S., Kalam M.Z., Packer K.J., & Zelaya F.O. (1990). Pore-size distributions from nuclear magnetic resonance spin-lattice relaxation measurements of fluid saturated porous solids. II. Applications to reservoir core samples. *Journal of Applied Physics, v. 67, n. 6, p. 3171-3176.*

D'Eurydice M.N., Montrazi E.T., Fortulan C.A., & Bonagamba T.J. (2016). T_2-Filtered T_2-T_2 Exchange NMR. *The Journal of Chemical Physics, 144 (20), 204201*.

De Ros, L.F., Anjos, S.M.C. & Morad, S. (1994). Authigenesis of amphibole and its relationship to the diagenetic evolution of Lower Cretaceous sandstones of the Potiguar rift basin, northeastern Brazil. *Sed.Geol., 88, 253–266*.

Dortch, R. D., Horch R. A., & Does M. D. (2009). Development, simulation, and validation of NMR relaxation-based exchange measurements. *The Journal of chemical physics, v. 131, n. 16, p. 164502.*

Dowey, P. J., Hodgson, D. M. & Worden, R. H. (2012). Pre-requisites, processes, and prediction of chlorite grain coatings in petroleum reservoirs: A review of subsurface examples. *Marine and Petroleum Geology, 32, 63-75*.

Dowey, P. J., Worden, R. H., Utley, J., & Hodgson, D. M. (2017). Sedimentary controls on modern sand grain coat formation. *Sedimentary Geology, 353, 46-63*.

Duliu, O. G. (1999). Computer axial tomography in geosciences: an overview. *Earth-science reviews, 48(4), 265-281*.

Dunlop, D. J., & Ozdemir, O. (1997). Rock Magnetism, 573 pp.

Dunn, K. J.; Bergman, D.J. & Latorraca, G.A. (2002). Nuclear Magnetic Resonance: Petrophysical and Logging Applications. *Inglaterra: Elsevier Science.*

Ehrenberg, S.N. (1993). Preservation of anomalously high porosity in deeply buried sandstones by grain-coating chlorite: examples from the Norwegian continental shelf. *AAPG Bulletin, 77(7), 1260–1286*.

Ehrenberg, S. N., & Nadeau, P. H. (2005). Sandstone vs. carbonate petroleum reservoirs: A global perspective on porosity-depth and porosity-permeability relationships. *AAPG bulletin, 89(4), 435-445*.

Ehrenberg, S. N., Nadeau, P. H., & Steen, Ø. (2008). A megascale view of reservoir quality in producing sandstones from the offshore Gulf of Mexico. *AAPG bulletin, 92(2), 145-164*.

Ehrlich, R., S. J. Crabtree Jr., K. O. Horkowitz, and J. P. Horkowitz. (1991). Petrography and reservoir physics I: objective classification of reservoir porosity: *AAPG Bulletin,75, 1547–1562*.

Elias, A. R., De Ros, L. F., Mizusaki, A. M., & Anjos, S. M. (2004). Diagenetic patterns in eolian/coastal sabkha reservoirs of the Solimões Basin, northern Brazil. *Sedimentary Geology, 169(3-4), 191-217.*

Fleury, M. (2007). NMR surface relaxivity determination using NMR apparent diffusion curves and BET measurements. *In: International Symposium of Society of Core Analysts, p. 10-12.*

Fleury, M., Deflandre F., & Godefroy S. (2001). Validity of permeability prediction from NMR measurements, *Comptes Rendus de l´Académie des Sciences-Series IIC-Chemistry, v.4, n. 11, p. 869-872.*

Foley, I., S. A. Farooqui, & R. L. Kleinberg.(1996). Effect of paramagnetic ions on NMR relaxation of fluids at solid surfaces. *Journal of Magnetic Resonance, Series A, 123, 95–104, doi: 10.1006/jmra.1996.0218.*

Folk, R.L.(1968). Petrology of Sedimentary Rocks. *Hemphill's Publ., Austin, Texas, 107 pp.*

Fraser, H. J.(1935). Experimental study of the porosity and permeability of clastic sediments. *In: Pettijohn. 1975. Sedimentary Rocks: New York, Harper and Row, 628 p.*

Fredrich, J. T., Greaves K. H., & Martin J. W. (1993). Pore geometry and transport properties of Fontainebleau sandstone. *In: International journal of rock mechanics and mining sciences & geomechanics abstracts, Pergamon, p. 691-697.*

Freitas, J. C. C., & Bonagamba, T. J. (1999). Fundamentos e aplicações da ressonância magnética nuclear. *Rio de Janeiro.*

French, M. W., & Worden, R. H. (2013). Orientation of microcrystalline quartz in the Fontainebleau Formation, Paris Basin and why it preserves porosity. *Sedimentary Geology, 284, 149-158.*

Gallegos, D. P., Smith D. M., & Brinker C. J. (1988). An NMR technique for the analysis of pore structure: Application to mesopores and micropores. *Journal of colloid and interface science, v. 124, n.1, p. 186-198.*

Garing, C., Chalendar J. A. de, Voltolini M., Ajo-Franklin J. B., & Benson S. M., (2017). Pore-scale capillary pressure analysis using multi-scale X-ray micromotography. *Advances in Water Resources, v. 104, p. 223-241.*

Giesche, H. (2006). Mercury Porosimetry: A General (Practical) Overview, *Particle and Particle Systems Characterization, 23(1), 9–19. DOI: 10.1002/ppsc.200601009*

Gislasson, S. R., P. J. Heaney, D. R. Veblen, and K. J. T. Levi. (1993). The difference between the solubility of quartz and chalcedony: the cause? *Chemical Geology, 107, 363–366.*

Glover, P. (2005). Petrophysics. *MSc. Course Notes-University Laval-Canada.*

Gluyas, J. G., Robinson, A. G., Emery, D., Grant, S. M., & Oxtoby, N. H. (1993). January. The link between petroleum emplacement and sandstone cementation. *In: Geological Society, London, Petroleum Geology Conference series (Vol. 4, No. 1, pp. 1395-1402). Geological Society of London.*

Grigsby, J. D., & Langford, R. P. (1996). Effects of diagenesis on enhanced-resolution bulk density logs in Tertiary Gulf Coast sandstones: An example from the lower Vicksburg Formation, McAllen Ranch field, south Texas. *AAPG bulletin, 80(11), 1801-1819.*

Grigsby, J. D. (2001). Origin and growth mechanism of authigenic chlorite in sandstones of the lower Vicksburg Formation, south Texas. *Journal of Sedimentary Research, 71(1), 27-36.*

Grunewald, E., & Knight, R. (2009). A laboratory study of NMR relaxation times and pore coupling in heterogeneous media. *Geophysics, 74(6), E215-E221.*

Grunewald, E., & Knight, R. (2011). A laboratory study of NMR relaxation times in unconsolidated heterogeneous sediments. *Geophysics, 76(4), G73-G83.*

Haddad, S. C., Worden R. H., Prior D. J., & Smalley P. C. (2006). Quartz cement in the Fontainebleau Sandstone, Paris Basin, France: crystallography and implications for mechanisms of cement growth. *Journal of Sedimentary Research, v. 76, n. 2, p. 244-256.*

Haszeldine, R. S., Cavanagh, A. J., & England, G. L. (2003). Effects of oil charge on illite dates and stopping quartz cement: calibration of basin models. *Journal of Geochemical Exploration, 78, 373-376.*

Hattori, I., Umeda, M., Nakagawea, T., & Yamamoto, H. (1996). From chalcedonic chert to quartz chert; diagenesis of chert hosted in a Miocene volcanic-sedimentary succession, central Japan. *Journal of Sedimentary Research, 66(1), 163-174.*

Heald, M. T., and R. E. Larese. (1974). Influence of coatings on quartz cementation: *Journal of Sedimentary Petrology, 44, 1269–1274.*

Hendry, J. P., & Trewin, N. H. (1995). Authigenic quartz microfabrics in Cretaceous turbidites; evidence for silica transformation processes in sandstones. *Journal of Sedimentary Research, 65(2a), 380-392.*

Hillier, S. (1994). Pore-lining chlorites in siliciclastic reservoir sandstones: electron microprobe SEM and XRD data, and implications for their origin. *Clay Mineral, 29(4): p. 665–679.*

Humphreys, B., Smith, S. A., & Strong, G. E. (1989). Authigenic chlorite in late Triassic sandstones from the Central Graben, North Sea. *Clay Minerals, 24(2), 427-444.*

Hürlimann, M. D., Helmer, K. G., Latour, L. L., & Sotak, C. H. (1994). Restricted diffusion in sedimentary rocks. Determination of surface-area-to-volume ratio and surface relaxivity. *Journal of Magnetic Resonance, Series A, 111(2), 169-178.*

Iijima, A. & Matsumato, S.R. (1982). Berthierine and chamosite in coal measures of Japan. *Clay Mineral., 30, 264–274.*

Jácomo, M. H., Trindade, R. I., de Oliveira, E. L., Leite, C. D. M., Montrazi, E. T., Andreeta, M., & Bonagamba, T. J. (2018). Nuclear Magnetic Resonance and Pore Coupling in Clay-Coated Sandstones With Anomalous Porosity Preservation, Água Grande Formation, Recôncavo Basin, Brazil. *Petrophysics, 59(02), 136-152.*

Jácomo, M. H., Trindade, R. I., French M., de Oliveira, E. L., Montrazi, E. T. & Bonagamba, T. J. (2019). NMR characterization of porosity-preserving microcrystalline quartz coatings in Fontainebleau sandstones. *In: AAPG Bolletin. Accepted.*

Jahren, J., & Ramm, M. (2000). The porosity-preserving effects of microcrystalline quartz coatings in arenitic sandstones: Examples from the Norwegian continental shelf. *Quartz cementation in sandstones, 29, 271-280.*

Jiang, F., Cheng, R., Ruan, B., Lin, B., Xu, Z., & Li, Z. (2017). Formation mechanism of volcanic reservoirs within a volcanostratigraphic framework: The case of the Wangfu fault depression in the Songliao Basin, China. *Marine and Petroleum Geology, 84, 160-178.*

Johnson, R.H. (1920). The cementation process in sandstone. *In: Walderhaug, O. 1994. Temperatures of quartz cementation in Jurassic sandstones from the Norwegian continental shelf; evidence from fluid inclusions. Journal of Sedimentary Research, 64(2a), 311-323.*

Kausik R., Minh C.C., Zielinski L., Vissapragada B., Akkurt R., Song Y., Schlumberger, Liu C., Jones S., Blair E., Chevron. (2011). Characterization of Gas Dynamics in Kerogen Nanopores by NMR. *In: SPE Annual Technical Conference and Exhibition, SPE 147198.*

Keating, K., & Knight R. (2007). A laboratory study to determine the effect of iron oxides on proton NMR measurements. *Geophysics, v. 72, n.1, p E27-E32.*

Keating, K., Knight, R., & Tufano, K. J. (2008). Nuclear magnetic resonance relaxation measurements as a means of monitoring iron mineralization processes. *Geophysical Research Letters, 35(19).*

Keating, K., & Knight, R. (2010). A laboratory study of the effect of Fe (II)-bearing minerals on nuclear magnetic resonance (NMR) relaxation measurements. *Geophysics, 75(3), F71-F82.*

Keating, K., & Knight, R. (2012). The effect of spatial variation in surface relaxivity on nuclear magnetic resonance relaxation ratesSpatially variable surface relaxivity. *Geophysics, 77(5), E365-E377.*

Kenyon, W. E., Howard, J. J., Sezginer, A., Straley, C., Matteson, A., Horkowitz, K., & Ehrlich, R. (1989, January). Pore-size distribution and NMR in microporous cherty sandstones. In SPWLA 30th Annual Logging Symposium. Society of Petrophysicists and Well-Log Analysts.

Kenyon, B., Kleinberg, R., Straley, C., Gubelin, G., & Morriss, C. (1995). Nuclear magnetic resonance imaging—technology for the 21st century. *Oilfield Review, 7(3), 19-33.*

Kenyon, W. E. (1997). Petrophysical principles of applications of NMR logging. *The Log Analyst, 38(02).*

Kenyon, W. (1997). Petrophysical principles of applications of NMR logging, The Log Analyst, v.38, n.2, p 43.

Kenyon, W.E., Howard J.J., Sezginer A., Straley C., & Matteson A. (1989). Pore-size distribution and NMR in microporous cherty sandstones, *in*: SPWLA 30th Annual Logging Symposium, Society of Petrophysicists and Well-Log Analysts.

Kieffer, B., Jové C. F., Oelkers E. H., & Schott J. (1999). An experimental study of the reactive surface area of the Fontainebleau sandstone as a function of porosity, permeability, and fluid flow rate. *Geochimica et Cosmochimica Acta, v. 63, n. 21, p. 3525-3534.*

Kleinberg, R.L., & Horsfield M. A. (1990). Transverse relaxation processes in porous sedimentary rock. *Journal of Magnetic Resonance, v. 88, n. 1, p. 9-19.*

Kleinberg, R. L., Kenyon, W. E., & Mitra, P. P. (1994). Mechanism of NMR relaxation of fluids in rock. *Journal of Magnetic Resonance, Series A, 108(2), 206-214.*

Kleinberg, R. L. (1996). Utility of NMR T_2 distributions, connection with capillary pressure, clay effect, and determination of the surface relaxivity parameter ρ2. *Magnetic resonance imaging, 14(7-8), 761-767.*

Kleinberg, R. L., & Vinegar, H. J. (1996). NMR properties of reservoir fluids. *The log analyst, 37(06), 20-32.*

Kleinberg, R. L., & Jackson, J. A. (2001). An introduction to the history of NMR well logging. *Concepts in Magnetic Resonance, 13(6), 340-342.*

Korb, J. P., Godefroy S., & Fleury M. (2003). Surface nuclear magnetic relaxation and dynamics of water and oil in granular packings and rocks. *Magnetic resonance imaging, v. 21, n. 3, 193-199.*

Kruiver, P. P., Dekkers, M. J., & Heslop, D. (2001). Quantification of magnetic coercivity components by the analysis of acquisition curves of isothermal remanent magnetisation. *Earth and Planetary Science Letters, 189(3-4), 269-276*.

LaTorraca G.A., Dunn K.J. Magnetic Susceptibility contrast effects on NMR T_2 Logging (1995). *In: SPWLA 36th Annual Logging Symposium, June 26-29, , pp. 1-4JJ*.

Leite C.M.M., Almeida J.R., De Ros L.F. Preservação de porosidade por microquartzo em reservatórios eólicos da Formação Água Grande na Bacia do Recôncavo, Bahia. *In: 47.Congresso Brasileiro de Geologia.*

Luo J., Morad S., Salem A., Ketzer J.M., Lei X.L., Guo D.Y., Hlal O. 2009. Impact of diagesis on reservoir-quality evolution in fluvial and lacustrine-deltaic sandstones: evidence from Jurassic and Triassic sandstones from the Ordos Basin, China. Journal of Petroleum geology, 32 (I). pp.79-102.

Lander, R. H., & O. Walderhaug. (1999). Porosity prediction through simulation of sandstone compaction and quartz cementation. *AAPG Bulletin, 83, 433–449*.

Leite, C.M.M., Almeida, J.R., and De Ros L.F. (2014). Preservation of microquartz porosity in eolian reservoirs of the Água Grande formation, Recôncavo Basin, Bahia [in Portuguese], *Paper 016233 presented at the 47th Brazilian Geological Congress, Salvador, Bahia, Brazil, 21–26 September*.

Li, H., Li H., Gao B., Wang W., & Liu C. (2017). Study on pore characteristics and microstructure of sandstones with different grain sizes. *Journal of Applied Geophysics, v. 136, p.364-371*.

Li, X., Kang, Y., & Haghighi, M. (2018). Investigation of pore size distributions of coals with different structures by nuclear magnetic resonance (NMR) and mercury intrusion porosimetry (MIP). *Measurement, 116, 122-128*.

Lima, R. D., & De Ros, L. F. (2002). The role of depositional setting and diagenesis on the reservoir quality of Devonian sandstones from the Solimoes Basin, Brazilian Amazonia. *Marine and petroleum geology, 19(9), 1047-1071*.

Livo, K. (2016). Mineralogical controls on NMR rock surface relaxivity: a case study of the Fontainebleau sandstone. *Master degree thesis, Colorado School of Mines*.

Liu, Q., Roberts, A. P., Larrasoana, J. C., Banerjee, S. K., Guyodo, Y., Tauxe, L., & Oldfield, F. (2012). Environmental magnetism: principles and applications. *Reviews of Geophysics, 50(4).*

Loucks, R. G., Reed, R. M., Ruppel, S. C., & Hammes, U. (2012). Spectrum of pore types and networks in mudrocks and a descriptive classification for matrix-related mudrock pores. *AAPG bulletin, 96*(6*), 1071-1098*.

Lowrie, W. (2007). Fundamentals of geophysics. *Cambridge university press.*

Luo J., Morad S., Salem A., Ketzer J.M., Lei X.L., Guo D.Y., Hlal O. (2009). Impact of diagesis on reservoir-quality evolution in fluvial and lacustrine-deltaic sandstones: evidence from Jurassic and Triassic sandstones from the Ordos Basin, China. *Journal of Petroleum geology*. *32 (I).79-102*.

Maast, T. E., Jahren, J., & Bjorlykke, K. (2011). Diagenetic controls on reservoir quality in Middle to Upper Jurassic sandstones in the South Viking Graben, North Sea. *AAPG bulletin, 95(11), 1937-1958.*

Magnavita L.P., Szatmari P., Cupertino J.A., Destro N., Roberts D. (2012).The Recôncavo Basin. *In: Regional Geology and Tectonics: Principles of Geologic Analysys. Editors: David G Roberts. A.W. Bally . Elsiever*

Mann, U., Hantschel, T., Schaefer, R.G., Krooss, B., Leythaeuser, D., Littke, R., (1977). Petroleum migration:mechanisms, pathaways, efficiencies and numerical simulations. *In:* Schön, J. H. 2014. *Propriedades físicas das rochas aplicadas à Engenharia de Petróleo.*

Marchand, A. M., Haszeldine, R. S., Smalley, P. C., Macaulay, C. I., & Fallick, A. E. (2001). Evidence for reduced quartz-cementation rates in oil-filled sandstones. *Geology, 29(10), 915-918*.

Marchand, A. M., Smalley, P. C., Haszeldine, R. S., & Fallick, A. E. (2002). Note on the importance of hydrocarbon fill for reservoir quality prediction in sandstones. *AAPG bulletin, 86(9), 1561-1572*.

Marschall, D., Gardner, J. S., Mardon, D., & Coates, G. R. (1995). September. Method for correlating NMR relaxometry and mercury injection data. *In: 1995 SCA Conference, paper(No. 9511).*

Maxbauer, D. P., Feinberg, J. M., & Fox, D. L. (2016). MAX UnMix: A web application for unmixing magnetic coercivity distributions. *Computers & Geosciences, 95, 140-145.*

McBride, E. F. (1989). Quartz cement in sandstones: a review. *Earth-Science Reviews, 26(1-3), 69-112*.

McKinley, J. M., Worden, R. H., Ruffell, A. H., & Morad, S. (2003). Smectite in sandstones: a review of the controls on occurrence and behaviour during diagenesis. *In: Clay Mineral Cements in Sandstones (Vol. 34, pp. 109-128). International Association of Sedimentologists Special Publication.*

Meiboom, S., & Gill D. (1958). Modified spin-echo method for measuring nuclear relaxation times. *Rev. Sci. Instrum., v. 29, p. 668–691*.

Milani E. & Davison I. (1988). Basement control and transfer tectonics in theReconcavo-Tucano-Jatoba rift, Northeast Brazil. *Tectonophysics, 154:41p.50.*

Mitchell, J., Chandrasekera T.C., Johns M.L., Gladden L.F., & Fordham E.J. (2010). Nuclear magnetic resonance relaxation and diffusion in the presence of internal gradients: the effect of magnetic field strength. *Physical Review E, v. 81, n. 2, p. 026101*.

Mitchell, J., Chandrasekera, T. C., Holland, D. J., Gladden, L. F., & Fordham, E. J. (2013). Magnetic resonance imaging in laboratory petrophysical core analysis. *Physics Reports, 526(3), 165-225*.

Mitra, P. P., Sen, P. N., & Schwartz, L. M. (1993). Short-time behavior of the diffusion coefficient as a geometrical probe of porous media. *Physical Review B, 47(14), 8565*.

Molenaar, N., Cyziene, J., Sliaupa, S., & Craven, J. (2008). Lack of inhibiting effect of oil emplacement on quartz cementation: Evidence from Cambrian reservoir sandstones, Paleozoic Baltic Basin. *Geological Society of America Bulletin, 120(9-10), 1280-1295*.

Montrazi, E. T., Lucas-Oliveira, E., Araujo-Ferreira, A. G., Barsi-Andreeta, M., & Bonagamba, T. J. (2018). Simultaneous acquisition for T_2-T_2 Exchange and T_1-T_2 correlation NMR experiments. *Journal of Magnetic Resonance*, 289, 63-71.

Moore, D. M., & Reynolds, R. C. (1989). X-ray Diffraction and the Identification and Analysis of Clay Minerals (Vol. 322, p. 321). *Oxford: Oxford university press*.

Morad, S., Ketzer, J. R. M., & De Ros, L. F. (2000). Spatial and temporal distribution of diagenetic alterations in siliciclastic rocks: implications for mass transfer in sedimentary basins. *Sedimentology, 47, 95-120*.

Morad, S., Al-Ramadan, K., Ketzer, J. M., & De Ros, L. F. (2010). The impact of diagenesis on the heterogeneity of sandstone reservoirs: A review of the role of depositional facies and sequence stratigraphy. *AAPG bulletin, 94(8), 1267-1309*.

Moraes, M. A., & De Ros, L. F. (1990). Infiltrated clays in fluvial Jurassic sandstones of Recôncavo Basin, northeastern Brazil. *Journal of Sedimentary Research, 60(6), 809-819*.

Morse, J. W., & Casey, W. H. (1988). Ostwald processes and mineral paragenesis in sediments. *American Journal of Science, 288(6), 537-560*.

Moss A.K., Jing X.D. (2001). An Investigation into effect of clay type volume and distribution on NMR measurements in sandstones. *In: International Symposium of the Society of Core Analysts. Paper SCA 2001-29.*

Milliken, K. L., & Curtis, M. E. (2016). Imaging pores in sedimentary rocks: foundation of porosity prediction. *Marine and Petroleum Geology, 73, 590-608*.

Nimmo, J. R. (2004). Porosity and pore size distribution. *Encyclopedia of Soils in the Environment, 3, 295-303*.

Oelkers, E. H., Bjørkum, P. A., and Murphy, W. M. (1996). A petrographic and computational investigation of quartz cementation and porosity reduction in North Sea sandstones. *In: Bjorkum, P. A., & Nadeau, P. H. 1998. Temperature controlled porosity/permeability reduction, fluid migration, and petroleum exploration in sedimentary basins.*

Osborne, M. J., & Swarbrick, R. E. (1997). Mechanisms for generating overpressure in sedimentary basins: A reevaluation. *AAPG bulletin, 81(6), 1023-1041*.

Øren, P., & Bakke S. (2002). Process based reconstruction of sandstones and prediction of transport properties. *Transport in Porous media, v. 46, n.2-3, p. 311-343.*

Pierret, A., Capowiez, Y., Belzunces, L., & Moran, C. J. (2002). 3D reconstruction and quantification of macropores using X-ray computed tomography and image analysis. *Geoderma, 106(3-4), 247-271*.

Pittman, E. D., & Lumsden, D. N. (1968). Relationship between chlorite coatings on quartz grains and porosity, Spiro Sand, Oklahoma. *Journal of Sedimentary Research, 38(2), 668-670*.

Pittman, E. D. (1971). Microporosity in carbonate rocks. *AAPG Bulletin, 55(10), 1873-1878*.

Pittman, E.D., Larese, R.E., and Heald, M.T. (1992). Clay Coats: Occurrence and Relevance to Preservation of Porosity in Sandstones, *in* Houseknecht, D.W., and Pittman, E.D., Editors, *Origin, Diagenesis, and Petrophysics of Clay Minerals in Sandstones, SEPM Special Publications, 47, 241– 255. DOI: 10.2110/pec.92.47.0241*.

Ramm, M., & Bjørlykke, K. (1994). Porosity/depth trends in reservoir sandstones: Assessing the quantitative effects of varying pore-pressure, temperature history and mineralogy, Norwegian Shelf data. *Clay minerals, 29(4), 475-490*.

Roberts, A. P., Heslop, D., Zhao, X., & Pike, C. R. (2014). Understanding fine magnetic particle systems through use of first□order reversal curve diagrams. *Reviews of Geophysics, 52(4), 557-602*.

Robertson, D. J., & France, D. E. (1994). Discrimination of remanence-carrying minerals in mixtures, using isothermal remanent magnetisation acquisition curves. *Physics of the Earth and Planetary interiors, 82(3-4), 223-234*.

Rosenbrand, E., Haugwitz, C., Jacobsen, P. S. M., Kjøller, C., & Fabricius, I. L. (2014). The effect of hot water injection on sandstone permeability. *Geothermics, 50, 155-166*.

Rouquerol, J., Avnir, D., Fairbridge, C. W., Everett, D. H., Haynes, J. M., Pernicone, N., Sing, J.D.F; & Unger, K. K. (1994). Recommendations for the characterization of porous solids (Technical Report). *Pure and Applied Chemistry, 66 (8), 1739-1758.*

Rueslatten H., Eidesmo T., Lehne K.A., Relling O.M. (1998). The use of NMR spectrometry to validate NMR logs from deeply buried reservoir sandstones. *Journal of Petroleum Science and Engineering, 19 pp.33-43.*

Ryu, S., & D. L. Johnson. (2009). Aspects of diffusion-relaxation dynamics with a nonuniform, partially absorbing boundary in general porous media: *Physical Review Letters, 103, 118701*.

Salimifard, B., Ruth, D. W., Green, D., & Veselinovic, D. (2014). September. Developing a Model to Estimate Permeability from Other Petrophysical Data. *In*: *SCA2014-063, International Symposium of the Society of Core Analysts*.

Saidian, M., & Prasad, M. (2015). Effect of mineralogy on nuclear magnetic resonance surface relaxivity: A case study of Middle Bakken and Three Forks formations. *Fuel, 161, 197-206*.

Saigal, G. C., Bjorlykke, K., & Larter, S. (1992). The effects of oil emplacement on diagenetic processes: examples from the fulmar reservoir sandstones, Central North sea: geologic note (1). *AAPG Bulletin, 76(7), 1024-1033*.

Schmidt-Rohr K., Spiess W. (1994). Multidimensional solid-state NMR and polymers. *Academic Press. San Diego, CA. 1st edition*.

Schmoker, J. W., & Schenk, C. J. (1994). Regional porosity trends of the Upper Jurassic Norphlet Formation in southwestern Alabama and vicinity, with comparisons to formations of other basins. *AAPG bulletin, 78(2), 166-180*.

Schön, J. H. (2014). Propriedades físicas das rochas aplicadas à Engenharia de Petróleo. (Vol. 1). Campus. *Traduction of Physical properties of rocks ISBN 978-85-352-7130-0. Elsevier*.

Sen, P. N. (2004). Time□dependent diffusion coefficient as a probe of geometry. *Concepts in Magnetic Resonance Part A: An Educational Journal, 23(1), 1-21*.

Smith, M. M., Wolery, T. J., & Carroll, S. A. (2013). Kinetics of chlorite dissolution at elevated temperatures and CO2 conditions. *Chemical Geology, 347, 1-8*.

Song, Y. Q., Venkataramanan, L., Hürlimann, M. D., Flaum, M., Frulla, P., & Straley, C. (2002). T_1–T_2 correlation spectra obtained using a fast two-dimensional Laplace inversion. *Journal of Magnetic Resonance, 154(2), 261-268*.

Song, Y. Q. (2003). Using internal magnetic fields to obtain pore size distributions of porous media. *Concepts in Magnetic Resonance Part A: An Educational Journal, 18*(2), *97-110*.

Souza, André Alves de. Estudo de propriedades petrofísicas de rochas sedimentares por Ressonância Magnética Nuclear. 2012. (*Tese de Doutorado, Universidade de São Paulo).*

Srodon J. 1980. Precise identification of illite/smectite interstratifications by x-ray powder diffraction. *Clays and clay minerals, vol. 28, n.6,pp 401-411*.

Straley, C., Morriss, C. E., Kenyon, W. E., & Howard, J. J. (1995). NMR in partially saturated rocks: laboratory insights on free fluid index and comparison with borehole logs. *The Log Analyst, 36(01).*

Surdam, R. C., Crossey, L. J., Hagen, E. S., & Heasler, H. P. (1989). Organic-inorganic interactions and sandstone diagenesis. *Aapg Bulletin, 73(1), 1-23*.

Swarbrick, R. E., & Osborne, M. J. (1998). Memoir 70, Chapter 2: Mechanisms that Generate Abnormal Pressures: an Overview.

Swarbrick, R. E., Osborne, M. J., & Yardley, G. S. (2002). *AAPG Memoir 76, Chapter 1: Comparision of Overpressure Magnitude Resulting from the Main Generating Mechanisms.*

Talabi, O., AlSayari S., Iglauer S., & Blunt M. J. (2009). Pore-scale simulation of NMR response. *Journal of Petroleum Science and Engineering, v. 67, n.3-4, p. 168-178*.

Tanner, J.E. (1970). Use of the stimulated echo in NMR diffusion studies. *J. Chem. Phys.*, 52, *2523-2526.*

Tauxe, L., Mullender, T. A. T., & Pick, T. (1996). Potbellies, wasp□waists, and superparamagnetism in magnetic hysteresis. *Journal of Geophysical Research: Solid Earth, 101(B1), 571-583*.

Tauxe L. (2005). Lectures in Paleomagnetism. *http://earthref.org/MAGIC/books/Tauxe/2005/*

Taylor, T. R., Giles, M. R., Hathon, L. A., Diggs, T. N., Braunsdorf, N. R., Birbiglia, G. V., Kittridge M. G., Macaulay C. I., Espejo, I. S. (2010). Sandstone diagenesis and reservoir quality prediction: Models, myths, and reality. *AAPG bulletin, 94(8), 1093-1132*.

Thiry, M., Ayrault M. B., & Grisoni J-C. (1988). Ground-water silicification and leaching in sands: Example of the Fontainebleau Sand (Oligocene) in the Paris Basin. *Geological Society of America Bulletin, v. 100, n. 8, p. 1283-1290.*

Thiry, M., & Maréchal B. (2001). Development of tightly cemented sandstone lenses in uncemented sand: example of the Fontainebleau Sand (Oligocene) in the Paris Basin. *Journal of Sedimentary Research, v. 71, n. 3, p. 473-483*.

Thiry, M. (2005). Weathering morphologies of the Fontainebleau Sandstone and related silica mobility. *Ferrantia, v.44, p.47-51*.

Thiry, M., Millot R., Innocent C., & Franke C. (2015a). The Fontainebleau Sandstone: bleaching, silicification and calcite precipitation under periglacial conditions - *Field trip guide, AIG-11, Applied Isotope Geochemistry Conference, September 21st to 25th 2015, Orléans, France, Scientific Report N° RS150901MTHI, Centre de Géosciences, Ecole des Mines de Paris, Fontainebleau, France, 26 pages.*

Thiry, M., Milnes A., & Ben Brahim M. (2015b). Pleistocene cold climate groundwater silicification, Jbel Ghassoul region, Missour Basin, Morocco. *Journal of the Geological Society, 172/2, p. 125-137, DOI: 10.1144/0016-76492014-033*.

Thiry, M., Liron M.N., Dubreucq P., & Polton J.C. (2017). Curiosités géologiques du massif de Fontainebleau. *Guide géologique, BRGM Editions, 115 p.*

Thomson, A., & Stancliffe, R. J. (1990). Diagenetic controls on reservoir quality, eolian Norphlet Formation, south State Line field, Mississippi. *Sandstone petroleum reservoirs* (pp. 205-224). Springer, New York, NY. *In: Pittman, E.D., Larese, R.E., and Heald, M.T., 1992, Clay Coats: Occurrence and Relevance to Preservation of Porosity in Sandstones, in Origin, Diagenesis, and Petrophysics of Clay Minerals in Sandstones, SEPM Special Publications, 47, 241– 255. DOI: 10.2110/pec.92.47.0241.*

Van Landeghem, M., Haber A., D'espinose De Lacaillerie J. B., & Blümich B. Analysis of multisite 2D relaxation exchange NMR. (2010). *Concepts in Magnetic Resonance Part A, v. 36, n. 3, p. 153-169.*

Vagle, G. B., Hurst, A., & Dypvik, H. (1994). Origin of quartz cements in some sandstones from the Jurassic of the Inner Moray Firth (UK). *Sedimentology, 41, 363-377.*

Vincent, B., Fleury, M., Santerre, Y., & Brigaud, B. (2011). NMR relaxation of neritic carbonates: An integrated petrophysical and petrographical approach. *Journal of Applied Geophysics, 74(1), 38-58*.

Walderhaug, O. (1994). Temperatures of quartz cementation in Jurassic sandstones from the Norwegian continental shelf; evidence from fluid inclusions. *Journal of Sedimentary Research, 64(2a), 311-323*.

Wang, R., Pavlin T., Rosen M.S., Mair R.W., Cory D., & Walsworth R.L. (2005). Xenon NMR measurements of permeability and tortuosity in reservoir rocks. *Magnetic Resonance Imaging, v. 23, n.2, p. 329-331*.

Washburn, K. E., & Callaghan, P. T. (2006). Tracking pore to pore exchange using relaxation exchange spectroscopy. *Physical review letters, 97*(17), 175502.

Washburn K.E., Eccles C., Callaghan P.T. (2008). The dependence on magnetic field strength of correlated internal gradient relaxation time distributions in heterogeneous materials. *Journal of Magnetic Resonance, v.194.n.1.pp.33-40.*

Webb, P. A. (2001). An introduction to the physical characterization of materials by mercury intrusion porosimetry with emphasis on reduction and presentation of experimental data. *Micromeritics Instrument Corp, Norcross, Georgia*.

Weibel, R., Friis, H., Kazerouni, A. M., Svendsen, J. B., Stokkendal, J., & Poulsen, M. L. K. (2010). Development of early diagenetic silica and quartz morphologies—Examples from the Siri Canyon, Danish North Sea. *Sedimentary Geology, 228(3-4), 151-170.*

Williams, L. A., Parks, G. A., & Crerar, D. A. (1985). Silica diagenesis; I, Solubility controls. *Journal of Sedimentary Research, 55(3), 301-311*.

Wilson, M. D., & Pittman, E. D. (1977). Authigenic clays in sandstones; recognition and influence on reservoir properties and paleoenvironmental analysis. *Journal of Sedimentary Petrology, 47(1), 3-31*.

Wilson, M. D. (1992). Inherited grain-rimming clays in sandstones from eolian and shelf environments: their origin and control on reservoir properties.*In: Origin, Diagenesis and Petrophysics of clay Minerals in Sandstones. AAPG SEPM Special Publication 47.*

Wilson, M. D., & Stanton, P. T. (1994). Diagenetic mechanisms of porosity and permeability reduction and enhancement. *AAPG SEPM Special Publication.*

Wilson, M. J., Wilson, L., & Patey, I. (2014). The influence of individual clay minerals on formation damage of reservoir sandstones: a critical review with some new insights. *Clay Minerals, 49, 147-164*.

Worden, R. H., Oxtoby, N. H., & Smalley, P. C. (1998). Can oil emplacement prevent quartz cementation in sandstones?. *Petroleum Geoscience, 4(2), 129-137*.

Worden, R. H., & Burley, S. D. (2003). Sandstone diagenesis: the evolution of sand to stone. *Sandstone Diagenesis: Recent and Ancient, 4, 3-44*.

Worden, R.H., & Morad, S. (2003). Clay Minerals in sandstones: Controls on Formation Distribution and Evolution. *In: Clay Mineral Cements in Sandstones, International Association of Sedimentologists Special Publication **34**, Blackwell Publishing, 3–41. ISBN: 1-40510-587-0. DOI: 10.1002/9781444304336.ch1*.

Worden, R. H., French, M. W., & Mariani, E. (2012). Amorphous silica nanofilms result in growth of misoriented microcrystalline quartz cement maintaining porosity in deeply buried sandstones. *Geology, 40(2), 179-182*.

Worden, R. H., Bukar, M., & Shell, P. (2018). The effect of oil emplacement on quartz cementation in a deeply buried sandstone reservoir. *AAPG Bulletin, 102(1), 49-75*.

Yardley, G. S., & Swarbrick, R. E. (2000). Lateral transfer: A source of additional overpressure?. *Marine and Petroleum Geology, 17(4), 523-537*.

Zhang, Q., Lo, S.-W., Huang, C.C., Hirasaki, G.J., Kobayashi, R., and House, W.V. (1998). Some Exceptions to Default NMR Rock and Fluid Properties. *In: 39th Annual Symposium of SPWLA, May 26-29, 1998, Keystone Resort, CO.*

Zhang G.Q., Hirasaki G.J., House V. (2001). Effect of internal Field Gradients on NMR Measurements. *Petrophysics, vol.42, n.1, pp-37-47.*

Zhao, X., Heslop, D., & Roberts, A. P. (2015). A protocol for variable□resolution first□order reversal curve measurements. *Geochemistry, Geophysics, Geosystems, 16(5), 1364-1377.*

Zhao, X., Roberts, A. P., Heslop, D., Paterson, G. A., Li, Y., & Li, J. (2017). Magnetic domain state diagnosis using hysteresis reversal curves. *Journal of Geophysical Research: Solid Earth*, *122*(7), 4767-4789.